UNIVERSITY OF OKLAHOMA

GRADUATE COLLEGE

AN INVESTIGATION BETWEEN TORNADIC AND NON-TORNADIC QLCS MESOVORTICES USING OPERATIONAL AND EXPERIMENTAL MRMS PRODUCTS

A THESIS

SUBMITTED TO THE GRADUATE FACULTY

in partial fulfillment of the requirements for the

Degree of

MASTER OF SCIENCE

By

TYLER JAMES PARDUN
Norman, Oklahoma
2023

Downloaded from SHAREOK. Persistent Handle URL: https://hdl.handle.net/11244/338758

AN INVESTIGATION BETWEEN TORNADIC AND NON-TORNADIC QLCS MESOVORTICES USING OPERATIONAL AND EXPERIMENTAL MRMS PRODUCTS

A THESIS APPROVED FOR THE
SCHOOL OF METEOROLOGY

BY THE COMMITTEE CONSISTING OF

Dr. Michael Coniglio, Chair

Dr. Anthony Reinhart

Dr. David Bodine

© Copyright by TYLER JAMES PARDUN 2023
All Rights Reserved.

Acknowledgments

This thesis would not have been possible without my family, my friends, and my co-advisors who have given me the skills and guidance I needed in order to accomplish this major task. This work would not have been accomplished without all of your support and guidance, and I do not take that for granted.

First, I would like to acknowledge my Mom and Dad who have given me so much support and guidance through this journey allowing me to follow my childhood dream. You have always cheered me on from the sideline and watched me grow as a student, a scientist, and a young adult. I am extremely blessed to be surrounded by your support and unconditional love throughout this process.

To my siblings, Michael, Katie, and Hannah who have never doubted for a second my choices that have led me on a journey into this field which ultimately led me to produce this work to furthering the science. To have you all by my side is an absolute blessing I do not take for granted. Your support and love will never go unnoticed.

To my closest friends who have always stood and listened to my excitement as I explain the context of this work. Your never-ending support and love has kept me going through the years and I am forever grateful to have each and everyone of you in my life. Whether you live in the Southern Plains, the Midwest, or in the Chicago suburbs, each of you are always in my heart and just a phone call away. The support you have all given me over the years means the absolute world and I will forever cherish these moments, with more to come.

To my co-advisors, Dr. Mike Coniglio and Dr. Tony Reinhart, I have always appreciated your patience and guidance during this time and I am extremely grateful for the opportunities you have presented to me over the years that allowed me to get to where I am, and shed light on the possibilities of where I can go. You have watched me grow as a student and as a scientist and I will forever cherish these moments as they boost me forward into my future. Here's to the next adventure!

CONTENTS

Acknowledgments **iv**

Abstract **xi**

1 Introduction **1**
- 1.0.1 QLCS Mesovortexgenesis . . . 1
- 1.0.2 Sensitivity of QLCS Mesovortices . . . 8
- 1.0.3 Single-Radar Case Studies . . . 11
- 1.0.4 Multi-Radar Capabilities . . . 12

2 Data & Methods **14**
- 2.0.1 Data Acquisition . . . 14
- 2.0.2 Operational and Experimental Products . . . 16
- 2.0.3 Multi-Radar Blending . . . 20
- 2.0.4 Mesovortex Identification . . . 22
- 2.0.5 Vortex Tracking Algorithms . . . 23

3 Operational and Experimental Product Analysis **28**
- 3.0.1 Azimuthal Shear . . . 29
- 3.0.2 Divergent Shear . . . 36
- 3.0.3 Convergent Shear . . . 38
- 3.0.4 Dual-Polarization Products . . . 41
- 3.0.5 Product Correlations . . . 43

4 Environmental Composites **46**

5 Summary and Conclusions **50**
- 5.0.1 Close-Proximity QLCS Mesovortices . . . 51
- 5.0.2 Far-Proximity QLCS Mesovortices . . . 54
- 5.0.3 Product Correlations . . . 55
- 5.0.4 RAP Analyses . . . 56
- 5.0.5 Operational Applications . . . 57

Reference List **59**

Appendix **67**
- 1 Figures . . . 67
- 2 Tables . . . 96

LIST OF TABLES

A.1 The full dataset containing 13 total QLCS storms including the start date of observation, their region of occurrence, the total number of WSR-88Ds used in blending, the number of tornadic mesovortices sampled (T_{vort}), the total number of non-tornadic QLCS mesovortices sampled (N_{vort}), the start time of observation, and the end time of observation in UTC. The total number of tornadic and non-tornadic mesovortices is shown at the bottom of the table in bold. Regions are organized by North Central Plains (NCP), Central Plains (CP), South Central Plains (SCP), Southeast (SE), Tennessee Valley (TV), and Midwest (MW). . 97

A.2 The full dataset organized by region of the CONUS including the average lifetime of tornadic mesovortices ($T_{Lifetime}$) and non-tornadic mesovortices ($N_{Lifetime}$) in minutes and average path length for tornadic (T_{path}) and non-tornadic (N_{path}) mesovortices in kilometers. 97

LIST OF FIGURES

A.1 A schematic of cyclonic-anticyclonic mesovortexgenesis in QLCS storms via upward vortex-line tilting adapted from figure 16 of Atkins and Laurent (2009). Vortex lines are represented in gold, the inflow and updraft denoted in red, and the downdraft in blue. The green arrow is representative of the mesovortex and the gust front position is annotated in black. 68

A.2 Schematic of QLCS mesovortexgenesis through upward vortex-line tilting in (a) easterly shear where the cyclonic (anticyclonic) member resides to the north (south) of the updraft and (b) downward vortex-line tilting in westerly shear where the cyclonic (anticyclonic) member resides to the north (south) of the downward forcing. Adapted from Weisman and Davis (1998) as their figure 5. 69

A.3 A cyclonic-only mesovortex adapted from Atkins and Laurent (2009) figure 3. (a) Rainwater mixing ratio (g kg^{-1}) is shown in grey shading. Contoured vertical velocity in m s^{-1} with thin dashed lines representing negative values and solid lines representing positive values. Vertical vorticity is shown in thick solid contours beginning and incremented at 1×10^{-2} s^{-1}. Horizontal wind vectors are also included. (b) Equivalent potential temperature (K) is contoured in grey. Air parcel trajectories projected at 0.2 km are shown (solid black). The vector field represents horizontal vorticity and is plotted as in (a). All fields in both (a) and (b) are plotted at 0.2 km AGL. 70

A.4 Schematic of mesovortexgenesis and subsequent tornadogensis through the release of horizontal shearing instability (HSI). The viewing perspective is looking northwest from an elevated position. Adapted from Lee and Wilhelmson (1997b) as their figure 24. 71

A.5 Regions of the Continental United States (CONUS) which include the North Central Plains (NCP; blue), Central Plains (CP; green), South Central Plains (SCP; gold), Southeast (SE; red), Tennessee Valley (TV; pink), and Midwest (MW; brown) used to classify regions of all QLCS mesovortices retained in the dataset. 72

A.6 All tornadic (red) and non-tornadic (green) mesovortex paths tracked from each QLCS storms retained in the dataset. All radars used in the blended products are annotated including their locations (center of the blue circle), corresponding radial distance from each radar in kilometers, and corresponding 0.5° beam height in kilometers AGL. 73

A.7 A histogram showing the 0–1 km layer-maximum azimuthal shear magnitude throughout the lifetime of all tornadic mesovortices retained in the dataset. The mean (solid black) and median (dashed purple) are labeled. 74
A.8 Histograms of tornadic (red) and null (green) mesovortex lifetime using (a) TRAQS, (b) TOBAC, and (c) TORP. The mean (solid black) and median (dashed purple) are annotated. 75
A.9 The median time-height cross section of azimuthal shear following (a) tornadic and (b) null mesovortices plotted against time relative to the (a) tornado report or (b) peak maturity. (c) The difference between the tornadic and null median. Gold stipplings represent significantly different grid points between the tornadic and null median at 95% confidence (α=0.05). Values are contoured at 0.008 s^{-1} (dashed black) and 0.006 s^{-1} (solid black). 76
A.10 The distribution of range [km] from the nearest radar at the time of tornadogenesis for (a) all tornadic mesovortices and (b) all null mesovortices binned every 5 km. The mean (solid black) and median (dashed purple) are annotated on each panel and the sample sizes are annotated in each panel title. 77
A.11 Same as Fig. A.9, except for close-proximity mesovortices residing less than or equal to 75 km in range from the nearest radar at the time of tornadogenesis or peak-maturity. 78
A.12 Same as Fig. A.9, except for far-proximity mesovortices residing greater than 75 km in range from the nearest radar at the time of tornadogenesis or peak-maturity. 79
A.13 Median 0–1 km azimuthal shear for tornadic (solid red) and null (solid green) mesovortices with their corresponding interquartile range (25th and 75th percentile; shaded) on the time scale relative to tornadogenesis or peak maturity. Statistically significant differences between the tornadic and null median at 95% (open circle; α=0.05) and 99% (closed circle; α=0.01) confidence are annotated along with the sample size for tornadic (n_{tor}) and null (n_{ntor}) mesovortices in (a) close-proximity and (b) far-proximity which is annotated in the title of each panel. 80
A.14 Same as figure A.13, except showing the 4–6 km layer maximum in azimuthal shear. 81
A.15 Similar to Figure A.9, except showing the median DivShear maxima within the boxed region surrounding the location of all (a) tornadic and (b) null mesovortices retained in the dataset. Values are contoured at 0.003 s^{-1} (dashed black). 82
A.16 Similar to Figure A.14, except showing the 6–10 km AGL layer-maximum DivShear. 83
A.17 Similar to Figure A.15, except showing the median DivShear maximum for close-proximity (a) tornadic and (b) null mesovortices. 84

A.18 Similar to Figure A.15, except showing the median DivShear maximum for far-proximity (a) tornadic and (b) null mesovortices. 85
A.19 Similar to Figure A.9, except showing DivShear minimum illustrating the maximum convergence in the boxed region surrounding all (a) tornadic and (b) null mesovortices retained in the dataset. Values are contoured at -0.005 s^{-1} (dashed black) and -0.003 s^{-1} (solid black). . . 86
A.20 Similar to Figure A.13, except the 4–6km AGL layer-minimum DivShear, illustrating maximum convergence. 87
A.21 Similar to Figure A.19, except showing DivShear minimum for close-proximity (a) tornadic and (b) null mesovortices with (c) the difference between the tornadic and null median. 88
A.22 Similar to Figure A.19, except showing DivShear minima for far-proximity (a) tornadic and (b) null mesovortices with (c) the difference between the tornadic and null median. 89
A.23 Similar to Figure A.9, except showing differential reflectivity (Z_{DR}) maximum for close-proximity (a) tornadic and (b) null mesovortices. Significantly different grid points at 95% (α=0.05) confidence are annotated as black circles. Values are contoured at 2 dB (dashed black) and 1.5 dB (solid black). 90
A.24 Similar to Figure A.23, except showing differential reflectivity (Z_{DR}) maximum for far-proximity mesovortices. 91
A.25 Similar to Figure A.9, except showing the specific differential phase (KDP) maximum for close-proximity (a) tornadic and (b) null mesovortices. Significant grid points at 95% are shown as black circles. Values are contoured at 1.5 deg km^{-1} (dashed black) and 1 deg km^{-1} (solid black). 92
A.26 The correlation between column-integrated azimuthal shear maximum and column-integrated spectrum width maximum following each QLCS vortex in time prior to t_0 (shaded). Each product is integrated from 0.25–10 km AGL beginning 60 minutes prior to t_0 and ending at t_0 (shaded). Each panel on the left-most column represents all tornadic mesovortices that spawned (a) EF 0, (c), EF 1, (e) EF 2+ tornadoes. (g) All tornadic mesovortices regardless of spawned tornado strength on the EF scale. The panels on the right most column represent all null mesovortices for comparison. 93
A.27 The distribution of kinematic environmental parameters derived from the RAP reanalysis showing (a) the 0–3 km vertical wind shear magnitude, (b) the 0–1 km storm relative helicity, (c) the 0–6 km bulk wind shear magnitude, and (d) the 0–3 km storm relative helicity. The distribution of tornadic (left) and null (right) mesovortices are shown on each panel captured one hour prior to t_0. 94

A.28 Similar to Fig. A.27, except showing (a) the lapse rate at the most unstable lifted condensation level (MULFC), (b) the 0–1 km layer mean mixing ratio, (c) the surface equivalent potential temperature (θ_e), and (d) the surface-based CAPE. 95

Abstract

Quasi-linear convective system (QLCS) tornadoes have become an active area of research over the last several years. Through numerical simulations, it is theorized that QLCS vortex formation occurs near the surface in a quick response to heterogeneities along the baroclinic zone at the leading edge of the system. The mechanisms responsible for the development of vorticity in the lowest tens of meters involve storm-scale processes such as downdrafts, rear inflow jets, and friction from land interactions. The Multi-Radar Multi-Sensor (MRMS) systems contain operational algorithms that can observe storm-scale dynamic features taking advantage of the quality of the WSR-88D network. Blending numerous WSR-88D radars surrounding a target QLCS can provide a more complete three-dimensional image compared to a single radar view that captures storm-scale characteristics at both the low and upper levels, blended onto a 0.01° latitude by 0.01° longitude (∼1 km) and 0.005° latitude by 0.005° longitude (∼500 m) horizontal grid space. This study highlights testing of currently operational (e.g., dual-pol products and azimuthal shear) and experimental MRMS products (e.g., divergent shear and total shear) that aid in detecting QLCS meso-γ-scale (2–40 km) vortices and subsequent tornadoes in both the pre-tornadic and tornadic phases.

A total of 107 tornadic and 139 non-tornadic mesovortices are examined over 13 QLCS events spanning from 2019 through 2022. It was found that tornadic mesovortices often display deep, transient plumes of significantly enhanced cyclonic shear relative to non-tornadic mesovortices during the pre-tornadic phase. Further, signals displaying a significantly higher magnitude of mid-to-upper level divergence and low-to-mid level specific differential phase (KDP) is illustrated, indicative of transient precipitation-loaded updraft pulses manifesting during the hour prior tornadogenesis. Additionally, the ambient environment in which tornadic mesovortices manifest are characterized with steeper most unstable lifted condensation level (MULFC) lapse rates and higher surface-based CAPE relative to their non-tornadic counterpart. Higher

0–3 km AGL and 0–6 km AGL are also evident in tandem with higher 0–1 km AGL and 0–3 km AGL storm relative helicity (SRH). Non-tornadic mesovortices are often characterized with a higher magnitude of cyclonic shear and convergent shear at the near-surface relative to their tornadic counterpart during the period prior to their peak in 0–1 km AGL layer-maximum azimuthal shear. High variability and significant overlap in the interquartile range exists for all operational and experimental products for all tornadic and non-tornadic mesovortices retained in the dataset, indicating that the processes involved in QLCS tornado formation can vary on a case-by-case basis.

Chapter 1

Introduction

1.0.1 QLCS Mesovortexgenesis

Mesovortices within quasi-linear convective systems (QLCSs) have been studied through the use of numerical simulations and observations (e.g., Forbes and Wakimoto, 1983; Przybylinski, 1995; Davis and Galarneau, 2009; Goodnight et al., 2022; Lovell and Parker, 2022). Numerical modeling studies have continued to investigate the origins of low-level rotation acquired in the lowest tens of meters for all types of mesoscale convective complexes (MCCs) including mesoscale convective systems (MCS), bow-echoes, and QLCSs in an effort to understand and anticipate tornadogensis within these systems (Davies-Jones, 2000; Weisman and Trapp, 2003; Trapp and Weisman, 2003; Wakimoto et al., 2006; Boyer and Dahl, 2020; Marion and Trapp, 2021; Tochimoto and Niino, 2022). There exist a few proposed mechanisms that explain the development of positive vertical vorticity in the lowest tens of meters that aid in the QLCS mesovortexgenesis process.

The process of upward vortex-line tilting via the downdraft is an important mechanism for the development of meso-γ-scale (2–40 km) vortices (herein referred to as mesovortices) along the leading edge of QLCS storms first proposed by Davies-Jones and Brooks (1993). Pre-existing horizontal vorticity, or vortex lines, induced either baroclinically due to the interaction of temperature and density gradients between the

storm's cold pool and the ambient environment or frictionally due to surface-land interactions (e.g., Flournoy and Coniglio, 2019; Boyer and Dahl, 2020; Tochimoto and Niino, 2022), can be oriented parallel to the leading edge of the QLCS. A surge in the storm's downdraft can act as a forcing mechanism, able to lift, tilt and subsequently stretch the existing horizontal vorticity into the vertical by the storm's updraft, forming a vortex pair at both ends of the bowing segment (Fig. A.1). The resulting location of the cyclonic and anticyclonic member relative to the apex of the bowing segment is determined by the 0–2.5 km above ground layer (AGL) environmental wind shear vector. Weisman and Davis (1998) found that when the resulting shear vector is easterly (i.e., the magnitude of the horizontal wind field decreases with increasing height), the cyclonic member is shown to reside north of the apex while the anticyclonic member resides to the south of the apex (Fig. A.2a). However, when the resulting shear vector is westerly (i.e., the magnitude of the horizontal wind field increases with increasing height), the cyclonic member resides to the south of the apex while the anticyclonic member resides to the north of the apex (Fig. A.2b).

For the ambient environment to manifest an idealized easterly 0–2.5 km AGL shear vector, the near-surface horizontal velocity field must be of greater magnitude relative to the horizontal velocity field aloft. Additionally, the near-surface velocity field must be westerly. An idealized example of this is found after an outflow surge, where the near-surface velocity field is westerly and of greater magnitude relative to the velocity field aloft (Weisman and Davis, 1998). In this idealized sense, the magnitude of the horizontal flow field decreases with increasing height atop the storm's cold pool (Fig. A.2a; Weisman and Davis, 1998). Subsequently, the forcing for ascent by the downdraft acts to lift and tilt pre-existing horizontal vortex lines into the vertical by means of an updraft (Fig. A.2a). This process has been shown numerically to occur in both QLCSs as well as supercell thunderstorms (e.g., Markowski and Richardson, 2014;

Dahl et al., 2014; Rotunno et al., 2017; Boyer and Dahl, 2020). In QLCSs however, this process subsequently produces a vortex couplet where the cyclonic (anticyclonic) member resides to the north (south) of the apex of the bowing segment (Fig. A.2a).

An idealized scenario in which westerly 0–2.5 km AGL shear can manifest is when a surge in storm-induced outflow is weak coupled with strong ambient 0–2.5 km AGL shear. In this instance, a smaller magnitude of westerly near-surface flow exists as stronger westerly flow resides atop the storm's cold pool (Fig. A.2b). Unlike the previous example of vortex-line tilting via the updraft, forcing from the downdraft can promote subsidence along the leading edge of the system which acts to suppress horizontal vortex lines subsequently producing a vortex pair on both ends of the apex (Fig. A.2b). This scenario, coined upward vortex line tilting via the downdraft (e.g., Trapp and Weisman, 2003; Weisman and Trapp, 2003) results in the cyclonic (anticyclonic) member residing to the south (north) of the apex of the bowing segment (Fig. A.2b; Davies-Jones and Brooks, 1993; Weisman and Davis, 1998; Atkins and Laurent, 2009; Boyer and Dahl, 2020). In the Northern Hemisphere, the tilting and subsequent stretching of planetary vorticity by means of the updraft can aid in the intensification of the cyclonic member (Weisman and Trapp, 2003).

Atkins and Laurent (2009) describes the mechanisms responsible for the generation of a cyclonic-only mesovortex embedded in a simulated QLCS representative of the 10 June 2003 Saint Louis bow echo observed during the Bow Echo and Mesoscale Convective Vortex (MCV) Experiment (BAMEX; Davis et al., 2004). The cyclonic mesovortex was located on a gradient of equivalent potential temperature (θ_e), noting two source regions of parcels feeding into the development of the mesovortex (Fig. A.3). One source region of parcels originate in high θ_e air at low-levels in the inflow region while the other originates in low θ_e air behind the gust front aloft within the descending rear-inflow jet (RIJ). Descending parcels were noted to position themselves

largely parallel to the horizontal vorticity vectors, strongly suggesting that these parcel acquired streamwise horizontal vorticity on approach to the developing cyclonic mesovortex. These parcels were then tilted and stretched by the updraft along the storm's gust front (Atkins and Laurent, 2009).

High θ_e parcels entering the developing mesovortex from the near inflow region of the storm were shown to originate near the parcels' nadir on the order of 200 m AGL. Inflow parcels then encountered positive tilting, similar to descending parcels approaching the mesovortex from the northwest behind the storm's gust front (Atkins and Laurent, 2009). However, the magnitude of positive streamwise vorticity acquired from the inflow parcels were lower in magnitude when compared to the vertical vorticity acquired by descending parcels. This result suggests that the descending low θ_e parcels, originating behind the storm's outflow, appear to be the most important in generating and maintaining the cyclonic mesovortex through tilting of horizontal streamwise vorticity (Atkins and Laurent, 2009).

Similar results related to parcel source regions of a cyclonic QLCS mesovortex is discussed in Flournoy and Coniglio (2019), simulating a mature QLCS as part of the Plains Elevated Convection at Night (PECAN) experiment that took place on 6 June 2015 in South Dakota. During the development stage of a strengthening cyclonic mesovortex, parcel trajectories were shown to originate in the near-inflow region of the storm and behind the storm's gust front. Inflow parcels were shown to originate at the low-levels, between 100–300 m AGL while descending parcels originate at 1 km AGL (Atkins and Laurent, 2009; Flournoy and Coniglio, 2019; Boyer and Dahl, 2020). Further, Flournoy and Coniglio (2019) showed that inflow parcels entering the developing mesovortex had little vertical vorticity before reaching the gust front and the storm's updraft. However, parcels originating from the storm's downdraft in a developing RIJ behind the gust front had a higher magnitude of vertical vorticity

acquired during descent on approach to the developing cyclonic mesovortex. These parcels then began to ascend into the low-level updraft (Atkins and Laurent, 2009; Flournoy and Coniglio, 2019).

The existence of horizontal vorticity along the leading edge of the system can be induced baroclinically or mechanically through the effects of environmental wind shear (e.g., Weisman and Trapp, 2003; Wheatley and Trapp, 2008; Atkins and Laurent, 2009; Schaumann and Przybylinski, 2012; Flournoy and Coniglio, 2019; Boyer and Dahl, 2020; Tochimoto and Niino, 2022). However, numerical simulations have shown that surface friction may play an important role in the generation of horizontal vorticity prior to mesovortexgenesis and subsequent tornadogenesis in QLCS storms (e.g., Markowski et al., 2012; Schenkman et al., 2014; Schenkman and Xue, 2015; Xu et al., 2015; Tochimoto and Niino, 2022).

A numerical simulation of a strong, long-lived QLCS mesovortex on 8-9 May 2007 in central Oklahoma was performed by Schenkman et al. (2012). A backward trajectory analysis from the low-level updraft of this mesovortex reveals the presence of a strong rotor situated to the northwest of the simulated tornado-like vortex (TLV) in the near-surface inflow[1]. When surface-friction is turned off in the simulation, the rotor and TLV are absent, indicating that the rotor manifests by means of the modeled surface-friction. The interaction between the storm outflow and frictionally generated near-surface horizontal vorticity was identified as the primary factor responsible for the formation of the rotor and subsequent TLV.

These studies suggest that surface friction may affect the horizontal vorticity by modifying the wind profile at the near the surface, which in turn can enhance the horizontal vorticity that is first generated by baroclinic processes (e.g., Roberts et al., 2016).

[1]Dahl et al. (2012) hypothesized that backward trajectory computations may be susceptible to errors especially near strong confluent flow in the vicinity of simulated mesovortices. Location errors in these trajectories primarily manifest as inflow trajectories that originate at the near-surface in the inflow region of the simulated vortex.

The inclusion of surface friction in a numerical simulation of a QLCS storm has been found to significantly affect QLCS tornado intensity, its path, and its longevity that was first observed in work by Schenkman et al. (2014). This highlights the importance of considering surface friction when studying the acquisition of vertical vorticity needed for QLCS mesovortexgenesis. However, the extent to which these methods adequately incorporate the influence of friction remains uncertain (Davies-Jones, 2021). Semi-slip boundary conditions incorporated in numerical simulations can spawn mesovortices and subsequent TLVs atypically early in simulated time, resulting in atypical storm behavior when compared to field observations (Davies-Jones, 2021).

An ingredients-based approach used heavily in current operational settings for anticipating QLCS mesovortices was first proposed by Schaumann and Przybylinski (2012) and coined the "three-ingredients method" (3IM). 3IM details an ingredients-based approach used to anticipate mesovortexgenesis in warm season QLCSs. Incorporated in the 3IM is a balance between the low-level environmental wind shear and the storm-induced cold pool. When a portion of the QLCS resides in an area in which the ambient low-level shear balances the storm's cold pool, or becomes slightly shear-dominant, the result leads to upright updrafts able to tilt existing horizontal baroclinic vorticity into the vertical via upward or downward vortex-line tilting processes described above for mature QLCSs.

The second ingredient of the 3IM is where the 0–3 km line-normal bulk shear magnitude is equal to or greater than 15 m s^{-1} (30 knots). Enhanced 0–3 km line-normal bulk shear characterized in the ambient environment acts to sustain convection at the leading edge of the system. The third ingredient involves an outflow-induced bowing segment observed on radar reflectivity that is associated with a descending rear-inflow jet (RIJ).

Case studies detailing this method appear to be relevant for anticipating areas within the storm capable of mesovortexgenesis (e.g., Gibbs, 2021; Goodnight et al., 2022). However, nearly half of mesovortexgenesis events analyzed by Ungar (2022) using proximity soundings were observed in sub-critical regimes relating the 0–3 km line-normal wind shear magnitude. This result emphasizes that the QLCS mesovortexgenesis process is highly variable and can occur when the 0–3 km line-normal bulk shear is below the 3IM threshold of 15 m s^{-1}.

The final mechanism discussed on the relation to QLCS mesovortexgenesis is the release of horizontal shearing instability (HSI) along the leading edge of the system. An extraction of energy from the mean ambient flow along the horizontal plane is converted into a maxima in vorticity (Conrad and Knupp, 2019). Numerical simulations that examine the role of HSI in mesovortexgenesis show that the vorticity generated is strongest at the near-surface which decreases with height up through 3 km AGL (Lee and Wilhelmson, 1997a,b). A schematic displaying the mesovortexgenesis process and subsequent tornadogenesis is outlined in figure A.4 adapted from the numerical simulations performed by Lee and Wilhelmson (1997b).

Buban and Ziegler (2016) performed a numerical simulation to resolve time scales at which mesovortices develop in an environment characterized by 16 m s^{-1} vertical wind shear, favoring the release of HSI. Their analysis reveals that discrete mesovortices develop 25-30 minutes into the simulation. Small time scales are apparent in relation to mesovortexgenesis in environments that favor the release of HSI which produces an additional operational forecasting challenge, should QLCS mesovortices begin the tornadogenesis process.

The notion that not all QLCS mesovortices subsequently produce tornadoes creates an additional forecasting challenge in the operational setting where lead times may not be as adequate to that of supercell tornadoes (e.g., Brotzge et al., 2013). Namely, the

three-ingredients method is used as a skillful ingredients-based approach to anticipate tornado potential in QLCS mesovortices operationally.

1.0.2 Sensitivity of QLCS Mesovortices

QLCS mesovortices may last as long as a few hours, yet QLCS tornadoes may only persist for a few minutes (Weisman and Trapp, 2003). Across the central and eastern United States, over 21% of all tornado reports occur from QLCS storms (Ashley et al., 2019). QLCS tornadoes are more prevalent at night when compared to right-moving (RM) supercell tornadoes, and more often lack clear evidence of a condensation funnel (Trapp et al., 2005; Ashley et al., 2019; Thompson, 2023). This creates the notion that the majority of QLCS tornadoes are based on damage assessments, of which tornado strength is often more weak (EF1 to EF2) with fewer strong (EF3+) relative to RM supercell tornadoes (Trapp et al., 2005; Smith et al., 2012; Thompson, 2023).

This creates an operational forecasting and nowcasting challenge to anticipate tornadoes from QLCS mesovortices due to their quick "spin up" nature (e.g., Trapp et al., 1999; Brotzge et al., 2013). A timely effort must be made to identify and diagnose QLCS mesovortices whether entering their tornadic phase or remaining non-tornadic to save both life and property.

In environments characterized by shear magnitudes of 15 m s^{-1} or less in the 0–2.5 km or 0–5 km AGL layer, Weisman and Trapp (2003) found that the QLCS mesovortices materialized are significantly weaker, shallower, and shorter-lived compared to deep and stronger mesovortices when the environmental shear vector exceeds 20 m s^{-1} or greater in these layers. Strong mesovortices, as noted by Lovell and Parker (2022) exhibit greater depth and longevity, increasing the likelihood of detection in an operational setting by the current radar network across the continental United States (CONUS). Strong mesovortices often display sustained surface vorticity and

near-ground updrafts for several minutes while weak mesovortices may lack this superposition, but often display impressive mid-level vorticity and mid-level updraft intensity (Lovell and Parker, 2022).

The numerical simulations performed by Lovell and Parker (2022) notes a lack in cyclonic-anticyclonic mesovortex couplets which contradicts past numerical studies (e.g., Weisman and Trapp, 2003; Atkins and Laurent, 2009). Yet, this finding highlights the importance of ambient streamwise vorticity in QLCS environments. When comparing tornadic mesovortices from their non-tornadic counterpart, it was found that nearly 20% of non-tornadic events briefly displayed a collocation of low-level updraft and low-level vertical vorticity, similar to the vertical structure in their simulated tornadic events (Lovell and Parker, 2022). If the residence time is increased for parcels entering the collocation of vertical vorticity and the updraft, the probability for a surface-vortex to manifest is increased (Lovell and Parker, 2022). The characteristics that best distinguish tornadic potential in QLCS vortex structures are namely reflectivity and radial velocity confined to the lowest 1 km AGL, which poses a challenge for detection since adequate radar coverage is confined to close-proximity of the radar itself (e.g., Davis and Parker, 2014).

Distributions of environmental parameters such as 0–3 km lapse rate and 0–3 km convective available potential energy (CAPE) are shown to be significantly different between weaker and stronger mesovortices (Lovell and Parker, 2022). Yet, the magnitudes of these differences are much smaller compared to the fields themselves indicating that operational forecasters may struggle to distinguish tornadic potential when assessing QLCS mesovortices using environmental parameters alone.

For tornadic QLCS mesovortices, sensitivity experiments were conducted regarding QLCS tornado intensity performed by Marion and Trapp (2021). Through their numerical simulations, additional curvature to the hodograph (i.e., enhanced deep layer

shear) produced stronger and longer-lived TLVs. Their work also highlights that TLV intensity is highly correlated to the parent low-level mesocyclone width ($r^2 = 0.61$). A weaker correlation exists between low-level updraft intensity and TLV intensity ($r^2 = 0.41$). In other words, their work highlights that the width of the low-level mesocyclone has influence in the intensity of the simulated TLVs. Stronger TLVs are associated with wider mesocyclones coupled with strong deep layer shear in the lowest 6 km regardless of the low-level updraft intensity.

Numerical simulations have highlighted a few important features related to the genesis of tornadoes occurring after the manifestation of intense low-mid level rotation (e.g., Davies-Jones et al., 2001; Schenkman et al., 2012; Boyer and Dahl, 2020; Marion and Trapp, 2021; Houser et al., 2022; Goodnight et al., 2022; Tochimoto and Niino, 2022). A conceptual model of tornadogensis discussed in Schenkman et al. (2012) includes an updraft that forms along the leading edge of the bowing segment which acts to tilt and subsequently stretch crosswise southward-oriented vortex lines, forming a vortex arc and subsequent vortex pair on both ends of the bowing segment (e.g., Trapp and Weisman, 2003; Tochimoto and Niino, 2022). Preference is given to the cyclonic member given the presence of background cyclonic vorticity in the northern hemisphere (e.g., Trapp and Weisman, 2003). As the cyclonic circulation begins to intensify, an increase in the low-level horizontal flow is realized ahead of the gust front while the generation of horizontal vorticity at the near-surface may be caused by surface drag (e.g., Schenkman et al., 2012; Xu et al., 2015; Tochimoto and Niino, 2022). This horizontal rotor is then forced to rise from ascent driven by the reinforced forward flank gust front (FFGF) after a surge in westerly momentum is caused by downdrafts from within the storm, leading to an intense low-level updraft (Schenkman et al., 2012). Concentrated vorticity surrounding the cyclonic mesovortex is then stretched by the intense low-level updraft, leading to the genesis of a simulated TLV (Schenkman et al.,

2012). This process is demonstrated for one QLCS that occurred on 8-9 May 2007, so the processes described may be limited by the experimental design (Schenkman et al., 2012).

1.0.3 Single-Radar Case Studies

Previous studies have used single-radar azimuthal shear or rotational velocity as a way to identify, study, and track mesovortices (Atkins et al., 2004, 2005; Davis and Parker, 2014). In a case study performed by Atkins et al. (2004), this work details the evolution of the 29 June 1998 derecho that propagated through Southeastern Iowa and eastern Illinois. After tracking seven tornadic and six non-tornadic mesovortices embedded within the bowing segment using rotational velocity, it was found that these tornadic mesovortices tend to be stronger in rotational magnitude and deeper in the column relative to their non-tornadic counterparts (Atkins et al., 2004). Similar results are discussed in a separate case study that details a bow echo occurring on 10 June 2003 near St. Louis, Missouri (Atkins et al., 2005). Using single-radar azimuthal shear in lieu of single-radar rotational velocity, tornadic mesovortices embedded within the system consistently retain stronger rotation in the 0–3 km AGL layer which deepened in the minutes prior to tornadogenesis.

A larger sample size of tornadic and non-tornadic QLCS mesovortices occurring in environments characterized by high shear (0–6 km bulk wind difference $\geq$18 m s^{-1} [35 knots]) and low CAPE ($<$ 500 J kg^{-1}) was performed by Davis and Parker (2014) using single-radar azimuthal shear. This study tracked 95 tornadic and 135 non-tornadic mesovortices and recorded azimuthal shear along the vortex tracks in both supercell and non-supercell convective modes.

Their results display statistically significant differences in the evolution of azimuthal shear between non-supercell tornadic and non-tornadic mesovortices within a 60 km

range of the radar below 1.3° in elevation (beam height < 1.4 km AGL). Non-supercell tornadic mesovortices display a larger magnitude in azimuthal shear nearly ten minutes prior to tornadogensis up through 1.4 km AGL. This is a result consistent with previous work and observations detailed in Atkins et al. (2004, 2005). Beyond 60 km in range from the radar, there were no statistically significant results able to distinguish non-supercell tornadic from non-tornadic mesovortices using single-radar azimuthal shear alone.

For High-Shear, Low-CAPE (HSLC) non-supercell mesovortices that became tornadic, azimuthal shear had increased in the minutes leading up to tornadogenesis while mesovortices that remained non-tornadic either decreased in magnitude of azimuthal shear, or remained in a quasi-steady state at 0.5° elevation within 60 km in range (beam height < 0.5 km AGL). Statistically significant differences in azimuthal shear were apparent for these mesovortices at the 95% confidence level from 5–10 min before to 1–5 min after the tornado or the issuance of the tornado warning for non-tornadic mesovortices. Physically, these results suggest that the low-level rotation increases in the minutes prior to tornadogensis in non-supercell tornadic mesovortices, yet rotation remains in a near quasi-steady state for non-tornadic mesovortices (Davis and Parker, 2014).

1.0.4 Multi-Radar Capabilities

Unlike the methods described in Davis and Parker (2014), where a single radar is used for analysis, this study incorporates a three-dimensional gridded analysis of WSR-88D observations via the Multi-Radar Multi-Sensor (MRMS) system (Smith et al., 2016a) to explore properties of mature QLCSs. The MRMS system combines data from multiple radar sources to create a more comprehensive and accurate representation of the storm structure. In this case, the main objective of this work is to incorporate radar

observations from multiple WSR-88Ds to create a three-dimensional gridded analysis of the parent QLCS, which can be analyzed to better understand the dynamics of QLCS mesovortices at all levels throughout its life cycle.

Performing this blend will allow most QLCS mesovortices identified to remain in close proximity to radars that are used in blending, keeping consistent with methods described in the previous literature for single-radar mesovortex observations (e.g., Atkins et al., 2004, 2005; Davis and Parker, 2014). This is important because it allows for a more thorough representation about the evolution of tornadic and non-tornadic QLCS mesovortices.

For this analysis, QLCS mesovortices are identified and tracked in time to discover differences in which tornadic (non-tornadic) mesovortices behave prior to tornadogenesis (peak maturity in rotational velocity) across the central and eastern United States. Understanding how tornadic and non-tornadic mesovortices behave can help to improve QLCS tornado forecasting and warning decisions in the operational setting. Specifically, this work aims to identify statistically significant differences in QLCS mesovortex evolution using gridded MRMS products. Further, the main objective of the work presented herein is to determine which MRMS derived products are the most effective in differentiating tornadic mesovortices from their non-tornadic counterparts in QLCS storms. The acquisition of level II radar observations and the methods performed to construct this analysis will be discussed in the next chapter.

Chapter 2

Data & Methods

To ensure this analysis is current, only QLCS storms occurring in or after the year 2019 were included in the dataset (Table A.1). The selection of each event date was based on subjective criteria to ensure that the dominant mode of convection resembles a QLCS mode and that all mesovortices at the time of tornadogenesis (tornadic) or peak rotational velocity (non-tornadic) occurred along the leading edge of the parent QLCS. Following suit with previous convective mode classification schemes, a QLCS event must resemble a well-defined bow echo and line observed on radar reflectivity (e.g., Smith et al., 2012; Ashley et al., 2019). Further, each QLCS event consists of contiguous reflectivity at or above 40 dBZ with a length-to-width ratio of at least 3 to 1, following the convective mode classification scheme in Trapp et al. (2005).

The dataset developed and analyzed in this study includes a total of 13 QLCS events occurring in different regions of the CONUS (Table A.2; The regions of the CONUS defined in this study are shown in Figure A.5). A total of 107 tornadic and 139 non-tornadic QLCS mesovortices are identified and each mesovortex is tracked in time by means of azimuthal shear (Fig. A.6).

2.0.1 Data Acquisition

For each QLCS event in the dataset, single-radar WSR-88D Level II observations are retrieved from the Amazon Web Service (AWS) database for each radar included in

the blended suite. The number of radars used in the blend for each event is provided in Table A.1. To ensure reliable three-dimensional gridded products, a minimum of four radars are required for the following analysis. The selection of radars used in the blend is based on their proximity to the parent QLCS. Radars located within a range of less than 100 km from the parent storm provide higher spatial resolution at the lowest levels (i.e., less than 3 km AGL) relative to radars situated in farther proximity (i.e., greater than 100 km in range) due to the effects of beam broadening (e.g., Giangrande and Ryzhkov, 2003; Ryzhkov, 2007; Gorgucci and Baldini, 2015). However, with multiple radars observing storm characteristics, each at their own respective beam heights above radar level (ARL) and look-angles relative to the parent storm, the limitations of using single-radar for analyses (i.e., beam broadening, beam elevation, and rotation signals relative to the orientation of the beam) are mitigated.

The observational period for each QLCS event was subjectively determined and rounded to the nearest hour. In some cases, the dominant mode of convection is initially discrete supercells in the subdomain of interest, prior to the initiation of the QLCS. However, as the initially discrete storms grow upscale into a QLCS mode through storm-induced outflow interactions or upon the arrival of strong external forcing (e.g., Dial et al., 2010), the dominant mode of convection thus becomes the QLCS. The start time of observation is defined as the time at which the QLCS becomes the dominant mode of convection, rounded to the nearest hour (Table A.2). The end time of observation is defined as the time at which the QLCS enters its dissipation stage, accompanied by no organized rotation along the leading edge of the system and/or a maximum reflectivity of the system falling below 40 dBZ. The ending time was also rounded to the nearest hour.

2.0.2 Operational and Experimental Products

The suite of algorithms housed under the Warning Decision Support System-Integrated Information (WDSS-II; Lakshmanan et al., 2007; Smith et al., 2016b) is employed to derive various products from the acquired Level II data. For each WSR-88D used in the blend, radial velocity was subject to dealiasing using the Radar Operations Center (ROC) two-dimensional velocity dealiasing algorithm (2DVDA) before MRMS products were computed (e.g., Jing and Wiener, 1993; Conway and Hondl, 1997; Losey-Bailor et al., 2019).

The computation of azimuthal and divergent shear (herein referred to as AzShear and DivShear, respectively) on a single WSR-88D radar involves utilizing the Linear Least Squares Derivative (LLSD) method on the dealiased radial velocity data (Smith and Elmore, 2004; Mahalik et al., 2019). The set of equations aimed at quantifying the gradients in radar observations yields part of the radial (divergent) and azimuthal (rotational) components of horizontal shear, estimating one-half of the two-dimensional horizontal divergence and vertical vorticity equations, respectively (Mahalik et al., 2019). The LLSD algorithm is housed within the w2circ algorithm in the WDSS-II framework (Lakshmanan et al., 2007; Smith et al., 2016b; Mahalik et al., 2019). This algorithm is used to compute all MRMS products advertised herein.

Both AzShear and DivShear represent the LLSD gradients on the radial velocity fields where positive (negative) AzShear values represent cyclonic (anticyclonic) rotation across an azimuth and positive (negative) DivShear values represent divergence (convergence) along a radial (Mahalik et al., 2019). Strong circulations often surpass an AzShear magnitude of ± 0.01 s^{-1} where the most intense circulations can obtain an AzShear magnitude in excess of ± 0.05 s^{-1} (Mahalik et al., 2019).

DivShear is an experimental product aimed at highlighting substorm-scale features such as convergence boundaries, storm-top divergence, and downbursts (e.g., Smith and

Elmore, 2004; Heinselman et al., 2008; Mahalik et al., 2019). DivShear is calculated in units of s^{-1}, identical to the units of AzShear. Since rotation signatures are often compact and near-circular, Mahalik et al. (2019) discusses that quasi-linear features, such as convergence boundaries, are resolved as a function of the radar viewing angle. For instance, a convergence zone at the leading edge of a bowing segment from a mature QLCS may be oriented parallel to the radar beam, resulting in locally lower AzShear and DivShear magnitudes when performing a single-radar analysis.

To compute the radial and azimuth components of the LLSD, the dealiased radial velocity data undergo a gate-relative 3x3 median filter to reduce noise found within the signal. The normal, linear, least squares derivatives for the radial (Eq. 2.1), azimuthal (Eq. 2.2), and constant (Eq. 2.3) components adapted from equations 6a-6c in Mahalik et al. (2019) are shown where

$$\frac{\partial R}{\partial u_r} = 0 = \sum_{k=0}^{mxn} 2(-u_k + u_0 + u_r \Delta r_k + u_\theta \Delta\theta_k) w_k \Delta r_k \tag{2.1}$$

$$\frac{\partial R}{\partial u_\theta} = 0 = \sum_{k=0}^{mxn} 2(-u_k + u_0 + u_r \Delta r_k + u_\theta \Delta\theta_k) w_k \Delta\theta_k \tag{2.2}$$

$$\frac{\partial R}{\partial u_0} = 0 = \sum_{k=0}^{mxn} 2(-u_k + u_0 + u_r \Delta r_k + u_\theta \theta_k) w_k. \tag{2.3}$$

For these sets of equations, R represents the sum of squares while u_r, u_θ, and u_0 represent the radial, azimuthal, and constant components (shears) of the radial velocity fields, respectively. Both m and n represent the LLSD kernel dimensions in the azimuthal (i = 0 to i = m) and radial (j = 0 to j = n) directions, respectively with k denoting each point (i, j) within the kernel itself. Both $\Delta\theta_k$ and Δr_k represent the offset in azimuth and range at point k within the kernel, respectively from the kernel center ($\theta = 0$, r = 0). w_k is the weighting coefficient applied at each point k within the

LLSD kernel. Illustrating complete derivation of the LLSD algorithm used to compute azimuthal and divergent shears is beyond the scope of this work, the reader is referred to Mahalik et al. (2019).

Following the AzShear and DivShear computations, a reflectivity mask is applied to the computed AzShear values over the LLSD kernel to address the unreliability of radial velocities co-located with poorly returned signal from the radar. In earlier versions of the LLSD algorithm, AzShear would be removed if the corresponding radar reflectivity at the same gate was less than 20 dBZ. However, this logic has been proven to be too drastic as mesocyclones and embedded mesovortices in convective systems can occur in weak echo regions (e.g.; Funk et al., 1999; Mahale et al., 2012). Consequently, this process was modified in an effort to retain AzShear found in the weak echo regions of convective systems by dilating the reflectivity. After the AzShear computation, reflectivity is dilated 5-fold on the polar grid to smooth over noise in the reflectivity returns. AzShear still found in gates with dilated reflectivity below 20 dBZ are then excluded. This process is repeated for every elevation angle native to the WSR-88D. Each radar's corresponding AzShear and DivShear magnitudes are placed onto a 0.005° latitude by 0.005° longitude (∼500 m) horizontal grid space.

Velocity gradient (herein referred to as total shear) is the third MRMS product used to analyze the QLCS mesovortices retained in the dataset. Total shear is simply the magnitude between the azimuthal and divergent shears shown in equation 2.4

$$V_T = \sqrt{A_s^2 * D_s^2} \tag{2.4}$$

where V_T is the total shear, ${A_s}^2$ is the squared quantity of AzShear, and ${D_s}^2$ is the squared quantity of DivShear. Total shear is derived for each WSR-88D used in the blend and placed onto the identical 0.005° latitude by 0.005° longitude grid space.

Reflectivity, dealiased radial velocity, and other dual-polarization products are placed onto a 0.01° latitude by 0.01° longitude ($\sim$ 1 km) horizontal grid space. The vertical resolution of all products remain consistent that stretch from 250 m between 0.25–3 km AGL to 500 m from 3–9 km AGL and finally to 1 km from 9–20 km AGL.

To obtain a two-dimensional field of AzShear, DivShear, and total shear, the vertical layer-maximum is computed where the highest value within a specified vertical layer is kept. For instance, 0–1 km AGL layer-maximum AzShear is simply the maximum value of AzShear taken at each grid point between the lowest elevation angle and the elevation angle(s) with a beam height below 1 km AGL. For this analysis, the 0–1 km AGL, 0–3 km AGL, 4–6 km AGL, and 6–10 km AGL layers are used to evaluate vortex evolution during the pre-tornadic or pre-maturity phase for tornadic and non-tornadic QLCS mesovortices, respectively.

The elevation angles used to compute the 0–1 km layer maximum products on the grid space include radar returns below 1° elevation while excluding all radar observations above 7° in elevation. If the beam height between 1° and 7° exceeds 1 km AGL, the radar data is excluded. For 0–3 km AGL layer maximum products, radar returns below 1° elevation are included while data above 20° elevation is excluded. Similar as before, if the beam height between 1° and 20° exceeds 3 km AGL, this data is also excluded. The 4–6 km AGL layer retains data below 9° elevation and excludes data above 36° elevation. The 6–10 km AGL layer retains data below 36° elevation and excludes data above 60° in elevation. If the WSR-88D does not include observations from elevation angles described here, the data retained or discarded will match the range of elevation angles retained or discarded depending on the layer-maximum that is being computed.

2.0.3 Multi-Radar Blending

Following the computations of AzShear, DivShear, and total shear on each WSR-88D used for blending, these products, along with reflectivity, radial velocity, and dual-polarization products are then merged onto the three dimensional grid space using the w2merger algorithm housed in the WDSS-II framework (Lakshmanan et al., 2006). When merging scalar data (e.g., AzShear, DivShear, reflectivity, etc.) onto a grid point in the volume grid (herein referred to as a voxel), the value of the voxel becomes the weighted sum of all observations from each gate at the location of the voxel since there could exist multiple radar estimates from each radar that is being used in the blend. For instance, Lakshmanan et al. (2006) describes that in the case of a Terminal Doppler Weather Radar (TDWR) volume scan, there could be multiple scans at the same elevation angle, producing multiple data points that straddle the voxel. To resolve this discrepancy, the data are weighted by distance and the most current data point is used. The weight of an observation (δ; Eq. 2.5) is given by

$$\delta = \delta_e \exp\left[-\left(\frac{t^2 r^2}{\beta}\right)\right], \tag{2.5}$$

$$\delta_e = \exp\left[\alpha^3 \ln(0.005)\right] \tag{2.6}$$

where δ_e is the elevation angle weight (Eq. 2.6), α is angular separation of the voxel from the center of the beam of an elevation scan as a fraction of either the beamwidth or the angular distance to the next higher or lower beam, t is the time difference between the time when the radar observation was made and the time of the grid, r is the range gate from where the observation was taken, and β is a constant of 17.36 s^2 km^2, a number chosen through experimentation by Lakshmanan et al. (2006).

For example, AzShear estimates from a single WSR-88D is a function of the beam angle relative to the mesovortex itself. Therefore, when merging multiple AzShear estimates onto the grid space, each radar will sample a different AzShear magnitude of the same vortex. The weighted sum of all measurements will become the value placed onto the grid space and used herein. The weighted sum becomes a more accurate estimate about the nature of the mesovortex being sampled, rather than using azimuthal shear derived from a single-radar with one beam angle (Lakshmanan et al., 2006).

The temporal resolution of each radar within the blended suite is unique, typically on the order of 5 minutes or less when convection is present within the radar's domain (e.g., Brown et al., 2000). Since the radars are not synchronized when merged together, their update times remain native to the instrument, leading to asynchronous updates in the three-dimensional gridded volume. Consequently, a portion of the three-dimensional gridded space may update in reflectivity while other portions remain fixed at the previous reflectivity scan, resulting in an incomplete representation of the current state of the system due to the asynchronicity in temporal resolution, causing spatial errors. However, Lakshmanan et al. (2006) discusses that if the radar coverage patterns (VCPs) were synchronized, it would not be possible to sample convection using multiple radars at different heights almost simultaneously due to the storm residing at multiple distances relative to each radar (Lakshmanan et al., 2006). Since asynchronicity exists among all radars used in the blend, the temporal resolution of the volume grid is set at two minutes in an effort to reduce spatial errors and smudging of the cells (Lakshmanan et al., 2006). The reader is referred to Lakshmanan et al. (2006) for more information regarding multi-radar blending and its capabilities.

2.0.4 Mesovortex Identification

Table A.1 references the total count of tornadic and non-tornadic QLCS mesovortices identified in each QLCS storm. Azimuthal shear in the 0–1 km AGL layer (herein referred to as AzShear01) is used to subjectively identify both tornadic and non-tornadic mesovortices in each QLCS event. This was done to ensure similar characteristics exist between tornadic mesovortices and their non-tornadic counterparts. However, the methods employed to identify and retain tornadic events differ from those used to identify and retain non-tornadic events.

Each tornadic QLCS vortex retained in the dataset is associated with a damage path defined in the National Weather Service (NWS) Damage Assessment Toolkit (DAT). The latitude and longitude coordinates of the path, the time of the initial tornado report, and the strength of each tornado on the Enhanced Fujita (EF) scale are recorded. Tornadic mesovortices are identified by collocating the local maxima in AzShear01 with the time of the start of the damage path.

A primary focus of this work is to understand the evolution of the pre-tornadic and post-tornadic phase using blended MRMS products. Thus, each tornadic vortex is tracked backward and forward in time relative to the time of the start of the damage path. This time is referred to as t_0. The methods that describe the tracking algorithms used to track tornadic and non-tornadic mesovortices will be discussed in the following section of this chapter.

Identifying a non-tornadic vortex (herein referred to as a null vortex) presents a greater challenge in terms of both its identification using AzShear01 and determining an analogous timestamp to tornadogenesis for tracking purposes (i.e., its t_0). This challenge is due to the absence of any distinct meteorological phenomenon or impact documented during the vortex's lifetime (e.g., visual documentation of meteorological

phenomena, a damage path, or a local storm report). To keep this analysis as controlled as possible, the definition of a null vortex must resemble similar characteristics to their tornadic counterpart. All tornadic mesovortices retained in the dataset are cyclonic in nature, therefore any anticyclonic null mesovortex is excluded. An analysis of AzShear01 throughout the lifetime of tornadic mesovortices illustrate that the majority of these mesovortices are characterized by AzShear01 at or just above 0.01 s^{-1} at some instance(s) during their lifetime where the median value of AzShear01 following all tornadic mesovortices in the dataset is approximately 0.012 s^{-1} (Fig. A.7). Therefore, a null mesovortex is best defined as having an isolated local maxima in AzShear01 in excess of 0.01 s^{-1} that resides in close proximity to the leading edge of the QLCS where no tornado or wind damage report is documented within a 50 km radius. Following the null vortex through time over the course of its life-cycle, the time at which AzShear01 is maximized along the null vortex path represents the most probable time for a tornado to occur, yielding the time that is analogous to tornadogenesis for tornadic mesovortices and thus referred to as t_0 in null mesovortices. This is time is coined peak-maturity, since AzShear01 is maximized which by definition includes the time of peak rotational velocity.

2.0.5 Vortex Tracking Algorithms

After t_0 has been established for each mesovortex identified, both tornadic and null mesovortices are tracked forwards and backwards in time relative to the start of the damage path or the time of peak maturity, respectively. Time bounds were set at a maximum of $\pm$ 60 minutes relative to t_0. To increase confidence in the accuracy of the tracks used for the results, three tracking algorithms are incorporated and compared. Each tracking algorithm is designed with unique methods used to track the center of each mesovortex and is discussed in-depth here.

A tracking algorithm was developed for this work to track all mesovortices retained in the dataset. This algorithm is coined Tracking AzShear in QLCS Storms (TRAQS). First, a 0.12° latitude by 0.12° longitude (∼13 km) box surrounding the location of maximum AzShear01 is drawn at the time of tornadogensis or peak maturity (t_0). To derive the vortex's track throughout the pre-tornadic or pre-maturity phase, the gridded AzShear01 is allowed to change by one time step backwards as the box remains fixed in space at t_0. The location and magnitude of the new maxima within the box is recorded and a new box of identical dimensions is placed around the new location of peak AzShear01 at this new time step. The location of the new maximum in AzShear01 is recorded which represents the new location of the vortex center. This process continues until the magnitude of AzShear01 falls below a threshold of 0.006 s^{-1}. An identical process is used to track each mesovortex in the post-tornadic or post-maturity phase except AzShear01 is allowed to change forward in time as the box from the previous time step remains fixed in space.

The second tracking algorithm incorporated in this analysis is the Tracking and Object-Based Analysis of Clouds (TOBAC; Heikenfeld et al., 2019). Specifically, the feature detection capabilities of TOBAC was used to pinpoint the location of the mesovortex center throughout its life cycle by means of a threshold of the input two-dimensional field of interest. In this instance, AzShear01 was used to pinpoint the vortex center with a threshold of 0.006 s^{-1}. TOBAC's feature detection incorporates an erosion technique adapted from the scikit-image library (van der Walt et al., 2014) to mitigate large interconnected regions of several features when regions are detected above the input threshold. To do this, the erosion technique shrinks the identified regions from the edges by a selected length or number of pixels (Heikenfeld et al., 2019). Ultimately, this reduction removes the connecting ridges between the interconnected features and enhances detection capabilities (Heikenfeld et al., 2019).

At t_0, TOBAC's feature detection was incorporated to isolate the location of each mesovortex on the grid space using AzShear01. When tracking the mesovortex forward in time, the AzShear01 field progressed forward in time and new features were detected by TOBAC. A distance filter was applied to isolate the features in proximity to the previous vortex location. The distance filter retains newly detected mesovortices within a 0.12° latitude by 0.12° longitude (∼13 km) box centered on the previous location of the mesovortex. The new location of the vortex is recorded and this process continues until the local maxima in AzShear01 falls below the threshold. This process is repeated for tracking the mesovortex backward in time prior to t_0. For more information on the capabilities of TOBAC, the reader is referred to Heikenfeld et al. (2019).

The third algorithm incorporated in this comparison is the Tornado Probability Algorithm (TORP; Sandmæl et al., 2023). This algorithm is built into the suite of algorithms housed in the WDSS-II framework and uses gridded single-radar MRMS products as predictors to estimate a probability of tornado occurrence in organized convection. This is accomplished using machine learning techniques integrated into the TORP framework. TORP ingests observations using single-radar analyses and tracks the identified mesovortex through time, producing probabilistic guidance related to tornadic potential over the course of its lifetime (Sandmæl et al., 2023).

TORP produces tornado probabilities using Level II single-radar data which includes reflectivity (Z_H), dealiased radial velocity, velocity spectrum width (SW), and other dual-polarization products including specific differential phase (ϕ_{DP}), correlation coefficient (ρ_{HV}), and differential reflectivity (Z_{DR}). The dealiasing algorithm used is the Build 19 version of the 2DVDA, identical to the dealiasing algorithm used herein.

TORP identifies storm objects (i.e., a mesovortex) using an AzShear threshold of 0.006 s^{-1}. These objects are identified by grouping radar gates displaying enhanced AzShear at or above the threshold, indicative of high rotation using a depth-first search

recursive algorithm (Tarjan, 1972; Sandmæl et al., 2023). Objects that consist of four or less gates become discarded to reduce the total number of objects associated with noise in the radial velocity returns, and must reside within 160 km from the radar itself (Sandmæl et al., 2023).

TORP records the location of each object identified which is used as the mesovortex track in this comparative analysis. To obtain a mesovortex track, TORP is initialized at a t_0 that corresponds to a particular mesovortex which becomes the object in question. All required fields that TORP uses to produce its probabilistic guidance is fed into the algorithm and these fields are allowed to progress forward in time while TORP records the object location. This same process is repeated for the period prior to t_0. Once the local maxima in AzShear01 falls below the threshold, the track is complete. Given that TORP uses single-radar fields only, the magnitude of AzShear01 in the single-radar analysis may not match the magnitude of the AzShear01 in the multi-radar analysis due to the beam angle relative to the axis of rotation of the mesovortex in question. Therefore, the data provided by each radar used in the blend will produce slightly different tracks for the same mesovortex. Since each mesovortex track produced by the ingestion of each radars' observations are quite similar, a track was picked at random and used in the comparative analysis. To learn more about TORP and its capabilities, the reader is referred to Sandmæl et al. (2023).

The distribution of vortex lifetime derived from each tracking algorithm is shown in Fig. A.8. For all tornadic events, TRAQS displays the highest mean and median of vortex lifetime whereas TOBAC displays the lowest (Fig. A.8a,c,e). The difference in median lifetime between TRAQS and TOBAC is approximately 15 minutes. Since TORP ingests single-radar observations, the azimuthal shear magnitude of each vortex in this case is lower relative to the azimuthal shear magnitude when numerous radars are blended together in the multi-radar analysis. This subsequently lowers the total

sample size of both tornadic and null mesovortices able to be tracked due to the set AzShear01 threshold of 0.006 s^{-1}.

When using the random-walk technique in TOBAC, the majority of null mesovortices are characterized with lifetimes less than 50 minutes, however both TRAQS and TORP tracking algorithms display a more even spread in lifetime distributions for null mesovortices (Fig. A.8b,d,f). Since there is no absolute "truth" to a mesovortex track, it is difficult to statistically compare the performance of each tracking algorithm and isolate the best one to use in the corresponding analysis. Since there exist no significant differences between vortex lifetime and the tracks themselves, TRAQS will be incorporated to track all mesovortices in the following analysis.

Chapter 3

Operational and Experimental Product Analysis

In this study, a controlled experiment is conducted to ensure that comparable characteristics of AzShear01 are present in both tornadic and null QLCS mesovortices. A central hypothesis of this research posits that currently available operational products, including AzShear, along with experimental products, such as DivShear and Total Shear can illustrate differences about the evolution of tornadic and null mesovortices in the QLCS storms retained in the dataset. Using the three-dimensional gridded space, profiles of AzShear, DivShear, and Total Shear are generated along the path of each mesovortex. This chapter will discuss the differences in tornadic and null QLCS mesovortex evolution, providing insight into the utility of these products for diagnosing tornadic potential in QLCS mesovortices.

To create profiles of MRMS products over the lifetime of each vortex, a 0.03° latitude by 0.03° longitude (∼3 km) box is centered around the coordinates of each vortex center[1] at all discrete height levels along its path. Rather than capturing the direct profile at the exact location of the vortex center, the maximum value within the boxed region at each height level is retained to provide a representative profile in the vicinity of the vortex in an effort to reduce spatial errors caused by coarse WSR-88D observations when relayed onto the same gridded space. The profiles are then placed

[1]For this work, the center of the QLCS vortex is defined as the location of maximum AzShear01 within the boxed region surrounding the vortex.

on a time scale relative to tornadogenesis for tornadic mesovortices and relative to peak maturity for null mesovortices.

To ensure an accurate distribution and to limit biased results from small sample sizes on the time-height grid, the median of each grid point on the time-height cross section is calculated if five or more data points exist, following similar methods described in Davis and Parker (2014). Since not every QLCS vortex is traced backward to 60 minutes prior to t_0, the highest quality median and sample size are displayed when considering the time frame between 20 minutes prior through 20 minutes after t_0.

When analyzing null mesovortices, the following must be considered. The absence of a damage path defined in the NWS DAT along the path of each null mesovortex provides high confidence that these mesovortices are truly non-tornadic. However, a damage path may not be defined if a tornado was never reported. Unfortunately, this plausible scenario is extremely difficult to address when approaching these rigorous scientific questions. Therefore, it is assumed that each null vortex is truly non-tornadic, yet some caution must be taken when interpreting the following results. An additional caveat to these results is that regionality and seasonality are variable, given the dataset retains QLCSs throughout the warm and cold seasons across the central and eastern CONUS. Merely, this work aims to provide an in-depth analysis about the performance of various MRMS products in a multi-radar framework on QLCS mesovortex evolution.

3.0.1 Azimuthal Shear

Significant differences between tornadic and null mesovortices exist mainly in the post-tornadic or post-maturity regime after t_0 regarding the median AzShear time-height cross section (Fig. A.9). Mainly above 2 km AGL after t_0, the median AzShear displayed in tornadic mesovortices remain much larger in magnitude relative to nulls,

indicating a significantly deeper column of cyclonic shear (Fig. A.9a). This signal persists for approximately 30 minutes after t_0 until the enhanced AzShear weakens rapidly (Fig. A.9a). Using the 0.006 s^{-1} isosurface as a proxy for the separation of noise and signal in cyclonic rotation (e.g., Davis and Parker, 2014), the altitude of this isosurface is situated at nearly 3.5 km AGL for 30 minutes after t_0 in tornadic events (Fig. A.9a). However, in null events, the column of cyclonic shear is approximately 1 km lower after peak cyclonic rotation is realized (Fig. A.9b). The prolonged period of significantly enhanced cyclonic shear shown in tornadic events after t_0 is a unique feature shown in tornadic events alone. Thus, it is plausible that this signal may be induced by the tornadic nature of these mesovortices, which are not present in the retained null mesovortices. Further, AzShear variance is higher in tornadic mesovortices when compared to nulls, especially below 2 km AGL, yet the maximum variance of all tornadic mesovortices retained is two orders of magnitude less than the AzShear values themselves (not shown). This variance may arise due to the regionality and seasonality of the mesovortices sampled, however the variance remains small enough where noise is suppressed in the median.

The identification of statistical significance between tornadic and null mesovortices is performed using a Monte Carlo simulation iterated 10000 times. First, the difference between the tornadic and null median is computed (e.g., Fig. A.9c). Then, a random sample of identical size to the sample size of the observed tornadic mesovortices (e.g, 107 cross sections) are taken, however the individual time-height cross sections taken at random are picked from either the tornadic or null mesovortex distribution. This same method is applied to create a median cross section of identical sample size to that of all observed null events (e.g., 139 samples). The median time-height cross section of AzShear, in this case, is computed for these two random samples and the difference between the two medians are retained. This process is repeated 10000 times to obtain a

distribution of median differences made up of the random samples. At each grid point, the percentile of which the observed median difference falls within in the distribution of the random sample median difference is computed. For this work, if the percentile of the observed median difference is below the 5th percentile or above the 95th percentile, this grid point is significantly different between the observed tornadic and null median time-height cross sections with 95% confidence (α=0.05).

Due to the coarse temporal resolution of the volume grid, each QLCS tornado produced by each tornadic mesovortex cannot thoroughly be resolved making it difficult to pinpoint the time at which each tornadic mesovortex enters and exits is tornadic phase. Given the brief nature of most QLCS tornadoes, the first five minutes after t_0 will represent the time frame analogous to the tornadic phase. During the first five minutes after t_0, AzShear below 3 km AGL is shown to be higher in magnitude more often in null events relative to tornadic events (Fig. A.9c). Yet, the null events retained here typically display a decrease in AzShear01 magnitude more rapidly after t_0 when compared to their tornadic counterpart.

Only a few significant differences exist prior to t_0 during the pre-tornadic or pre-maturity phase in the median AzShear time-height cross section. A few details are illustrated in this regime that can be skillful in differentiating tornadic mesovortices from nulls using AzShear alone. The first illustrating a signal of persistent cyclonic rotation on the order of 0.008 s^{-1} displayed in the 1–3 km AGL layer throughout the majority of the pre-tornadic phase of tornadic events (Fig. A.9a). A common significantly different feature observed in tornadic events are deep plumes of enhanced AzShear extending upwards of 3 km AGL from the near-surface, whereas these features remain absent in null events prior to t_0 (Fig. A.9b). This result remains consistent with previous work detailing deeper columns of rotation in tornadic mesovortices using only

single-radar analyses, especially in HSLC environments (e.g., Atkins et al., 2004, 2005; Davis and Parker, 2014).

Between 20 through 10 minutes prior to t_0, tornadic mesovortices display a larger magnitude of AzShear between 2–3 km AGL relative to null mesovortices (Fig. A.9a). Nulls however, realize a similar increase in cyclonic rotation beginning 10 minutes prior to peak maturity or later (Fig. A.9c). Ten minutes prior to t_0 through t_0, null mesovortices display significantly larger magnitudes of AzShear relative to tornadic mesovortices below 3 km AGL (Fig. A.9b). These results signify that null mesovortices may often display a peak AzShear magnitude larger than that of tornadic mesovortices at the near-surface, yet the depth of enhanced cyclonic rotation at the time of peak-maturity and shortly thereafter is often more transient in the case of null events.

Twenty minutes prior to t_0, both the median AzShear in tornadic and null mesovortices evolve quite similarly in the 0–3 km AGL layer (Fig. A.9). Hence, there exists some ambiguity in using low-level AzShear alone as a proxy for diagnosing tornadic potential. Such products include AzShear01 and 0–3 km layer-maximum AzShear (AzShear03). Undoubtedly, both AzShear01 and AzShear03 are extremely skillful in identifying QLCS mesovortices, especially since AzShear01 is used to identify and track all tornadic and null events retained herein. However, the depth of the retained QLCS mesovortices have been shown to vary over the course of their lifetimes (not shown). AzShear01 signals pertaining to extremely shallow ($\leq$ 1 km AGL) mesovortices may not ever manifest in the AzShear01 signals, leading to a lower probability of detection should these events arise.

It is well-known that the quality of radar sampling decreases as range increases away from the radar, which is primarily caused by beam broadening. As range increases, the height of the beam elevates as per the effects of Earth's curvature. Consequently, a radar sampling a mesovortex in far-proximity will not only return broad gates of

reflectivity and radial velocity than a mesovortex in close-proximity, the mesovortex in far-proximity will be sampled at a higher altitude by the lowest elevation angle set native to the WSR-88D in question. From this, a mesovortex in far-proximity might display higher returns of rotational velocity if the signal of rotation extends deep in the column, thus raising the magnitude of AzShear. For example, if a QLCS vortex resides approximately 100 km away from the closest radar, the 0.5° elevation beam height at the location of the mesovortex will reside at nearly 1 km AGL. Therefore, the 0–1 km layer will likely possess more samples closer to 1 km AGL than at the near-surface, unlike samples from a mesovortex within 20 km in range from the radar. At this range, the 0.5° elevation beam resides closer to the near-surface, around 170 m AGL. Therefore, results comparing tornadic and null mesovortices regardless of range from the nearest radar may induce a high-AzShear bias that favors mesovortices at far-proximity from the closest radar. To ease the resulting high-AzShear bias induced by range from the nearest radar, all mesovortices are grouped by their distance.

At t_0, the mean and median range relative to the nearest radar are similar for both tornadic and null events (Fig. A.10). Since both tornadic and null events are characterized by a mean and median range of 75 km rounded to the nearest kilometer, all mesovortices are organized into two regimes: close-proximity and far-proximity. Close-proximity mesovortices are those that reside less than or equal to 75 km in range from the closest radar at t_0. Far-proximity mesovortices are those that reside in excess of 75 km in range from the closest radar at t_0. If a vortex manifests in excess of 75 km of the nearest radar and deviates into the close-proximity threshold by the start of its damage path or at the time of peak-maturity, the vortex is classified as a close-proximity vortex. The same ideology holds true for a vortex manifesting in close-proximity and deviates into the far-proximity regime by t_0, where the vortex is

classified as a far-proximity vortex. However, the majority of all mesovortices retained in the dataset do not cross-over into the other regimes during their lifetimes.

In terms of the AzShear evolution for close-proximity tornadic events, deep pronounced plumes of enhanced cyclonic AzShear extend just above 3 km AGL during the pre-tornadic phase (Fig. A.11a). However, close-proximity null mesovortices display a larger magnitude of AzShear below 2 km AGL prior to t_0 (Fig. A.11b,c). In close-proximity to the nearest radar, where spatial resolution is improved, it is evident that tornadic events display significantly higher AzShear above 2 km AGL while null events display significantly higher AzShear below 2 km AGL beginning nearly 25 minutes prior to t_0.

Tornadic mesovortices in far-proximity display significantly higher AzShear in the lowest 3 km AGL from 60 minutes through 20 minutes prior to t_0 (Fig. A.12a). Starting 10 minutes prior to t_0, far-proximity null events begin to show significantly higher AzShear below 3 km AGL up through t_0 and onward (Fig. A.12b). For both close and far-proximity mesovortices, the AzShear magnitude below 3 km is shown to be higher in null events when compared to tornadic events. This signal is shown to manifest approximately 5–10 minutes prior to t_0. However, AzShear magnitude above 3 km AGL is shown to be significantly larger in tornadic events starting 50 minutes through 20 minutes prior to t_0 in far-proximity mesovortices and 20 minutes through t_0 in close proximity mesovortices.

Since AzShear below 3 km AGL is shown to be significantly higher in far-proximity tornadic mesovortices relative to nulls beginning nearly 40–50 minutes prior to t_0, AzShear01 is able to highlight these significant differences as well (Fig. A.13). Small overlap in the interquartile range (IQR) exists between tornadic and null events at this time period in far-proximity mesovortices, yet much more overlap is apparent in close-proximity mesovortices prior to t_0 (Fig. A.13). Approximately 10 minutes prior,

AzShear01 increases substantially in both close-proximity tornadic and null events, catering no statistical significance (Fig. A.13a).

Even with the small overlap in IQR in during the period prior to t_0, the IQR in tornadic events is shown to be broad (Fig. A.13b). Upon further analysis, nearly 21% of far-proximity tornadic mesovortices were actually pre-existing supercell mesocyclones that merged into the parent QLCS from 30–31 May 2022 in the north central plains of the United States. Supercell mesocyclones characterized by AzShear can be larger in magnitude compared to AzShear measured in QLCS mesovortices (e.g., Davis and Parker, 2014; Flournoy et al., 2022). In this instance, all tornadic mesovortices occurring on this day reside at or above the median and subsequently raises the spread in the IQR. Given that there exists little overlap in the tornadic and null IQR 20 minutes prior through t_0, ambiguity exists when using AzShear01 alone to diagnose tornadic potential in the QLCS mesovortices retained in this dataset. Similar results are displayed for 0–3 km layer-maximum AzShear (not shown).

Close-proximity tornadic mesovortices are shown to display significantly enhanced AzShear above 3 km AGL starting nearly 40 minutes prior to t_0 (See Fig. A.11a,c). However, 4–6 km AGL layer-maximum AzShear (AzShear46) seldom denotes statistical significance when diagnosing tornadic potential in close-proximity mesovortices (Fig. A.14a). Only some close-proximity tornadic mesovortices are characterized by AzShear46 in excess of 0.012 s^{-1}, while the 75th percentile of AzShear46 sampled in close-proximity null mesovortices seldom reach 0.012 s^{-1} from 60 minutes through 10 minutes prior to t_0. After t_0, close-proximity tornadic mesovortices often display a higher magnitude of AzShear46 relative to nulls when in their post-tornadic phase (i.e., $\geq$ 5 minutes after t_0). A rapid reduction in AzShear46 magnitude is apparent in close-proximity null mesovortices after peak low-level cyclonic rotation is reached (Fig. A.14a). In close proximity mesovortices 30 minutes prior to t_0, tornadic events

typically display an AzShear46 magnitude between 0.009 s^{-1} and 0.018 s^{-1} while nulls display a range between 0.007 s^{-1} and 0.013 s^{-1}.

AzShear46 in far-proximity mesovortices remain significantly higher in magnitude relative to far-proximity null events from 60 minutes through 20 minutes prior to t_0 (Fig. A.14b). Here, tornadic events typically display an AzShear46 magnitude between 0.01 s^{-1} and 0.018 s^{-1}. During the same time frame, null events display an AzShear46 magnitude between 0.005 s^{-1} and 0.013 s^{-1}. Beginning 20 minutes prior through t_0 and beyond, no discernible differences are found between far-proximity tornadic and null mesovortices in terms of their cyclonic shear in the 4–6 km AGL layer.

3.0.2 Divergent Shear

DivShear is able to quantify the divergence along the radial by using raw radial velocity as input sampled by each WSR-88D used in the blended suite (Smith and Elmore, 2004; Mahalik et al., 2019). Similar to the methods described to obtain profiles of AzShear, the same method applies to compute DivShear profiles. By retaining the *maximum* value of DivShear in the boxed region surrounding the location of the vortex at each discrete height level, it is possible to quantify the amount of maximum divergence surrounding each vortex to understand differences about the evolution of the pre-tornadic and pre-maturity phases.

When including all mesovortices regardless of range from the nearest radar, tornadic events display significantly higher DivShear beginning 25 minutes prior to t_0 extending from the near-surface through 6 km AGL (Fig. A.15a). This signal of enhanced divergence on the order of 0.003 s^{-1} first manifests around the same time enhancements are illustrated in AzShear, on the order of 0.008 s^{-1} (See Fig. A.9a). The persistent signal of enhanced divergence throughout the 0–6 km AGL layer remains throughout the tornadic and into the post-tornadic phase of the median tornadic mesovortex. Although

the evolution of AzShear below 3 km AGL is quite similar between tornadic and null events, the absence of enhanced divergence below 6 km AGL in null mesovortices is a statistically different feature which can aid in the detection of tornadic potential among mesovortices (Fig. A.15b,c).

At the median, tornadic mesovortices realize significantly higher DivShear on the order of 0.003 s^{-1} first observed near 10 km AGL at 60 minutes prior to t_0 that then translates into the 0–6 km AGL layer beginning 20 minutes prior to t_0 and lasting into the post-tornadic phase. By computing the 6–10 km AGL layer maximum DivShear (DivShear610), close-proximity tornadic events display higher DivShear relative to null events beginning 40 minutes through 5 minutes prior to t_0 (Fig. A.16a). Within five minutes prior to t_0, both close-proximity tornadic and null mesovortices are characterized with similar magnitudes of DivShear610, yet tornadic events illustrate a history of higher divergence aloft. Similar results are shown for far-proximity mesovortices (Fig. A.16b). However, far-proximity tornadic mesovortices realize an increase in DivShear610 25 minutes prior to t_0 compared to 40 minutes prior in close-proximity tornadic events.

Close-proximity tornadic mesovortices relay significantly higher DivShear from the near-ground through 10 km AGL not apparent in null mesovortices, yet this signal is maximized in the 2–6 km AGL layer (Fig. A.17). Using the 0.006 s^{-1} isosurface of AzShear as a proxy for vortex depth of these mesovortices, the transient plumes of enhanced cyclonic rotation extend to a depth between 3–4 km AGL (See Fig. A.11a). With this in mind, the DivShear maxima in these mesovortices reside near the top of the median vortex, indicating divergence signatures atop the vortex related to an updraft noted from 40 minutes prior to t_0 throughout the post-tornadic phase. Moreover, a significantly weaker signal of median divergence atop the median null mesovortex is

evident, yet a similar magnitude of median AzShear is present suggesting a reduction in updraft intensity throughout the pre-maturity phase relative to tornadic events.

Close-proximity nulls exhibit near-surface divergence extending to 4 km AGL beginning 5 minutes prior to peak-maturity, yet this signal is much shallower when compared to close-proximity tornadic events (Fig. A.17. Given that both close-proximity tornadic and null events display a similar magnitude of DivShear in the lowest 4 km AGL, it is plausible that this signal may resemble a surge in outflow as the magnitude of the near-ground horizontal flow becomes amplified, yet the divergence signal related to the outflow surge near t_0 extends much deeper in the column in close-proximity tornadic events.

In far-proximity tornadic mesovortices, there exists two separate regimes of significantly enhanced DivShear relative to null events (Fig. A.18a). Beginning 60 minutes through 20 minutes prior to t_0, DivShear is maximized in the 8–10 km AGL layer before the secondary maximum is visualized the below 4 km AGL 20 through 10 minutes prior to t_0. Near t_0 however, an amplification of DivShear below 4 km AGL is absent unlike close-proximity tornadic events. Since these mesovortices reside at a greater distance from the radars, it is possible an outflow surge may exist below the beam height of the lowest elevation, removing the amplified DivShear signal near t_0 apparent in close-proximity tornadic events. This same explanation can be applied to far-proximity null events.

3.0.3 Convergent Shear

To capture profiles of convergent shear, the same method used to capture DivShear profiles is performed, except the *minimum* value of DivShear within the 0.03° latitude by 0.03° longitude (∼3 km) box is captured at all discrete height levels surrounding the location of the vortex along its path. Negative values of DivShear represent radial

convergence and herein referred to as convergent shear for the sake of simplicity. Results presented in this section will use the observed negative values of DivShear.

Both the median tornadic and null vortex time-height cross section display a maximum in convergent shear at the near-surface that decreases with height up through 10 km AGL (Fig. A.19). All tornadic and null events regardless of range from the nearest radar display similar magnitudes of convergent shear below 3 km AGL, yet null events are characterized with slightly higher near-surface convergence relative to their tornadic counterpart. Beginning 20 minutes through 10 minutes prior to t_0 , tornadic mesovortices associate with a deepening and amplifying column of convergent shear extending to just above 2 km AGL on the order of -0.005 s^{-1} (Fig. A.19a). This signal illustrating the transient plumes of convergent shear is not apparent at the median in null events, rather a prolonged period of deep convergent shear during the same period of time (Fig. A.19b).

Tornadic mesovortices are characterized with significantly larger convergent shear above 3 km AGL relative to nulls (Fig. A.19). As time approaches the tornadic phase, convergent shear becomes amplified below 8 km AGL, noting an approximate 4 km increase in depth over a span of 10 minutes when using the -0.003 s^{-1} isosurface as a proxy for the depth of enhanced convergence (Fig. A.19a). Median convergent shear in null events illustrate a quasi-steady convergent shear depth over time, both during the pre-maturity phase and through the post-maturity phase (Fig. A.19b).

A significant difference between the two medians, invariant of distance from the closest radar, is that tornadic mesovortices display deeper profiles of convergent shear relative to the median null vortex prior to t_0. The evolution of the pre-tornadic phase displays transient, yet deep plumes of significantly enhanced convergence realized in the 4–6 km AGL layer relative to nulls. In this layer, the transient plumes of amplified convergence are observed to occur multiple times in a cyclic nature throughout the

pre-tornadic phase (Fig. A.19a). This signal displaying a cyclic nature in enhanced convergent shear in the 4–6 km AGL layer mostly occurs in close-proximity mesovortices.

Upon investigating the evolution of the IQR of convergent shear for close-proximity tornadic mesovortices, the spread of observed convergent shear magnitudes in this layer becomes larger, indicative of increasing variability within the pre-tornadic phase (Fig. A.20a). This result indicates that the evolution of mid-to-upper level convergent shear varies substantially within the pre-tornadic phase close-proximity tornadic events. On the other hand, the spread of observed 4–6 km convergent shear in close-proximity null events is not as large (Fig. A.20a). During the pre-maturity phase, 4–6 km convergent shear ranges from approximately -0.002 s^{-1} to -0.006 s^{-1} whereas convergent shear in the close-proximity tornadic events range from -0.002 s^{-1} to -0.01 s^{-1} during the pre-tornadic phase.

Due to the existence of large variability in 4–6 km AGL convergent shear in the pre-tornadic phase, it is evident that about half of the close-proximity tornadic events realize convergent shear in excess of -0.006 s^{-1} in the minutes leading up to t_0. To pinpoint the exact processes involved allowing the close-proximity tornadic mesovortices retained in the dataset to realize convergent shear in excess of -0.006 s^{-1} has yet to be explored.

For tornadic mesovortices in far-proximity, the variability of 4–6 km AGL layer maxima in convergent shear remains small during the pre-tornadic phase where convergent shear ranges from -0.002 s^{-1} to -0.006 s^{-1} (Fig. A.20b). Similarly, convergent shear in the pre-maturity phase of far-proximity null events are shown to range from -0.002 s^{-1} to -0.005 s^{-1} (Fig. A.20b). From this, there exist only modest significant differences aimed at diagnosing tornadic potential for mesovortices in far-proximity from the nearest radar using convergent shear alone.

A significantly more pronounced and deeper column of convergent shear extending through 10 km AGL is displayed in close-proximity tornadic mesovortices beginning 20 minutes prior to t_0 (Fig. A.21a). Close-proximity null events associate with a persistent shallow column of convergent shear maximized at the near-ground throughout the entire pre-maturity phase (Fig. A.21b). Approximately 5 minutes prior to t_0, both tornadic and null events display a deepening column of convergent shear, yet tornadic events associate with a significantly deeper column that exceeds 10 km AGL when compared to close-proximity nulls.

Far-proximity tornadic events are characterized with higher magnitudes of convergent shear compared to far-proximity nulls at the near-ground beginning 40 minutes through 20 minutes prior to t_0 (Fig. A.22a). Transient plumes of significantly enhanced convergent shear appear during this time period in the pre-tornadic phase, yet this signal is removed from 20 minutes prior to t_0 through the tornadic phase. Nearly 10 minutes prior to t_0, null mesovortices are shown to obtain significantly higher convergent shear from that of their tornadic counterpart below 2 km AGL (Fig. A.22b). Similarly, null events also display a significantly higher magnitude of AzShear during the same period of time, indicating a signal that could resemble a localized area of strong near-surface convergence associated with a localized low pressure perturbation given the enhanced near-ground cyclonic shear.

3.0.4 Dual-Polarization Products

There are differences related to the maximum differential reflectivity (Z_{DR}) within the boxed region surrounding each mesovortex through time between close-proximity tornadic and null mesovortices, mainly above 6 km AGL prior to t_0 (Fig. A.23). Beginning 60 minutes through 30 minutes prior to t_0, close-proximity tornadic events display a

higher magnitude of Z_{DR} below 6 km AGL relative to null events on the order of approximately 0.5 dB (Fig. A.23). From 30 minutes through 10 minutes prior to t_0, a signal denoting a reduction in Z_{DR} is noted tornadic events, mainly below 2 km AGL whereas a signal displaying an enhancement in Z_{DR} below 2 km AGL is noted in null events.

During the tornadic phase above 6 km AGL, the median Z_{DR} magnitude is significantly lower in close-proximity tornadic mesovortices when compared to all close-proximity nulls (Fig. A.23). The results thus far have highlighted that deeper columns of convergent shear and AzShear along with a persistent signal of enhanced DivShear is illustrated atop the median close-proximity tornadic mesovortex, indicative of strong rotation updrafts during the pre-tornadic phase. Given a significant reduction in DivShear atop the median close-proximity null mesovortex, it is possible that the signal of strong updrafts within the pre-tornadic phase are able to loft large hydrometeors away from the vortex center, effectively lowering Z_{DR} magnitude throughout the column in the vicinity of the vortex.

Far-proximity tornadic mesovortices display significantly large Z_{DR} below 6 km AGL from 60 minutes through 20 minutes prior to t_0 (Fig. A.24). Compared to close-proximity mesovortices, far-proximity tornadic events display higher Z_{DR} magnitude relative to nulls in this layer 20 minutes longer in the pre-tornadic phase. Beginning 20 minutes prior to t_0 through t_0, Z_{DR} magnitude above 6 km AGL is significantly lower in far-proximity tornadic mesovortices relative to nulls. Both close and far-proximity tornadic events show a similar evolution in terms of Z_{DR} where tornadic events associated with lower Z_{DR} magnitude above 6 km AGL relative to null mesovortices.

During the pre-tornadic phase of the median close-proximity tornadic mesovortex evolution, small enhancements in Z_{DR} are collocated in time with small enhancements in specific differential phase (KDP) early on in the vortex lifetime up through 30

minutes prior to t_0 (Fig. A.25a). Below 4 km AGL, the magnitude of KDP in close-proximity tornadic mesovortices is significantly higher relative to nulls by 1–1.5 deg km^{-1}, especially between 60 to 40 minutes prior to t_0.

Similar to the median KDP evolution in tornadic events, null mesovortices display pulses of enhanced KDP, yet the magnitude of these pulses are on the order of 1–1.5 deg km^{-1} from 60 minutes through 10 minutes prior to peak-maturity and extend to just above 2 km AGL(Fig. A.25b). However, an increase in KDP is realized 10 minutes prior to t_0 of similar magnitude to that of the median tornadic vortex where no significant differences exist between the two below 3 km AGL.

After t_0, the magnitude of KDP tapers off dramatically 10 minutes after peak-maturity in close-proximity null mesovortices while tornadic events maintain enhanced magnitudes of KDP for approximately 20–30 minutes longer after the tornadic phase (Fig. A.25b). Upon further analysis, similar results are displayed for far-proximity mesovortices (not shown). However, KDP below 1 km AGL resides on the order of 3 deg km^{-1}, while KDP below 1 km AGL in far-proximity null events are sampled on the order of 2.5 deg km^{-1}.

3.0.5 Product Correlations

Several notable differences have been observed between tornadic and null mesovortices when integrating MRMS product profiles and correlating these products to others during the pre-tornadic and pre-maturity phase (e.g., Fig. A.26). Across the range of products discussed thus far, correlating each unique combination of products is performed to assess whether differences exist between tornadic and null mesovortices prior to t_0. These products include layer maximum products for the 0–1 km AGL, 0–3 km AGL, and 6–10 km AGL layer, as well as the three-dimensional products for AzShear, DivShear maxima and minima, total shear, and dual-polarization products

such as Z_{DR} and KDP. To generate a product analogous to the layer-maximum product for each three-dimensional product, values were summed from 0.25 km AGL through 10 km AGL during the period prior to t_0. A total of 552 unique combinations of products are assessed. Correlations were calculated for every unique combination of products, and a linear regression was performed on the resulting data. The coefficients of the best-fit line were normalized by the standard deviation of the predictor variable for an accurate comparison. The coefficients relating to tornadic and null mesovortices were subtracted from each other to determine the pair of products exhibiting the greatest difference in normalized coefficient, which will be discussed next.

A notable difference in product correlations between tornadic and null mesovortices in close-proximity to the nearest radar is observed through integrated AzShear and integrated spectrum width (Fig. A.26). Tornadic mesovortices, especially tornadic mesovortices that produce EF0 tornadoes, are characterized by a distinct regime. Most notably this regime consists of column integrated AzShear below 0.04 s^{-1} when column-integrated spectrum width is greater than 50 m s^{-1} at some instance(s) during the pre-tornadic phase (Fig. A.26a). Approximately 43% of this regime consists of data points occurring at some instance between 20 minutes prior to t_0 through t_0, yet column-integrated AzShear and column-integrated spectrum width are shown to reach these thresholds at instances in excess of 40 minutes prior to t_0. Further, this signal manifests in approximately 11% (12 tornadic mesovortices) of all tornadic mesovortices retained in the dataset occurring in all regions except the central plains, providing evidence that this signal does not pertain to one specific region across the CONUS.

AzShear and spectrum width are positively correlated in both tornadic and null mesovortices (Fig. A.26). Intuitively, an increase in cyclonic shear at a range gate yields an increase in the radial velocity variance within the same gate hence increasing

the spectrum width that is sampled. In tornadic mesovortices that spawn EF0 tornadoes, the pre-tornadic phase is characterized by low column-integrated AzShear in tandem with low column-integrated spectrum width relative to tornadic mesovortices that spawn EF1+ tornadoes during their lifetime (Fig. A.26a,c,e). Throughout the column, a decrease in AzShear can be related to a downdraft signal yielding the presence of anticyclonic shear in the vicinity of the vortex. Further, the decrease in spectrum width can be associated with more uniform radial velocity measurements within the gate from the effects of the surging outflow. However, it should be noted that this signal occurs in approximately 11% of all tornadic mesovortices retained and in all referenced regions of CONUS except the central plains. A higher volume of QLCS mesovortices may provide additional insight, especially in tornadic mesovortices that produce EF0 tornadoes.

In all tornadic mesovortices represented in the dataset, column-integrated AzShear is larger with increasing spectrum width relative to nulls (Fig. A.26g,h). Tornadic mesovortices have been shown to associate with deeper and stronger cyclonic shear relative to their non-tornadic counterpart (See Fig. A.9). This relationship is correlated higher in tornadic mesovortices (r^2=0.65) compared to nulls (r^2=0.48), indicating more variability in column-integrated AzShear in null mesovortices.

Chapter 4

Environmental Composites

Environmental parameters, such as the 0–3 km and 0–6 km wind shear magnitude, 0–1 km and 0–3 km storm relative helicity, the lapse rate at the most unstable lifted condensation level (MULFC), 0–1 km mean mixing ratio, surface equivalent potential temperature (θ_e), and surface-based CAPE are captured in the vicinity of all tornadic and null mesovortices in an effort to understand whether differences exist and if they are able to discern tornadic potential. Data was gathered from the Rapid Refresh (RAP) archive with a spatial resolution of 0.18° in longitude and 0.12° in latitude (∼53 km x ∼34 km) and a temporal resolution of one hour. The environmental parameters at the corresponding grid point in closest proximity to each mesovortex is captured at one hour prior to t_0, rounded to the closest hour of the RAP grid. This was performed in an effort to prognose tornadic potential in all QLCS mesovortices prior to tornadogenesis or peak-maturity.

All RAP data is subject to quality control, given the plausible scenario of questionable data at the grid point being retained for analysis. For each thermodynamic and kinematic variable's distribution, a value is removed if the value is beyond three standard deviations away from the mean of the sample.

One hour prior to t_0, modest differences exist in terms of the environmental shear magnitude and storm relative helicity (SRH; Fig. A.27). The 0–3 km wind shear magnitude represented in all tornadic mesovortices one hour prior to t_0 illustrates a bi-modal distribution (Fig. A.27a). Two peaks are set at approximately 13 m s^{-1} and

23 m s^{-1} with a median of 21 m s^{-1} rounded to the nearest integer. The median 0–3 km wind shear magnitude represented in null mesovortices resides at 19 m s^{-1} rounded to the nearest integer. However, significant overlap exists in the IQR.

The environment in the vicinity of null events are characterized with lower 0–1 km SRH relative to their tornadic counterpart at the median (Fig. A.27b). However, two peaks in null environments are realized were each peak is centered around 100 m^2 s^{-2} and again at 450 m^2 s^{-2}. 0–1 km SRH in tornadic events are fairly uniform where 0–1 km SRH between 100–400 m^2 s^{-2} is observed often within the hour prior to t_0. There are also instances where null mesovortices manifest in environments with 0–1 km SRH exceeding 500 m^2 s^{-2}, a threshold in which no tornadic mesovortex retained in the dataset has manifest in. Similar comparative results are shown for 0–3 km SRH (Fig. A.27d).

In terms of deep layer shear, tornadic mesovortices reside in environments with nearly 5 m s^{-1} more 0–6 km wind shear than their non-tornadic counterpart at the median (Fig. A.27c). Often, the environment in which tornadic mesovortices manifest is characterized with 0–6 km wind shear above 20 m s^{-1} (80% of all tornadic events in the hour prior to t_0) whereas null mesovortices often manifest when the 0–6 km wind shear magnitude is below 30 m s^{-1} (72% of all null events). From results discussed in Lovell and Parker (2022) and Ungar (2022), ambient deep layer shear in excess of 20 m s^{-1} is associated with stronger and deeper mesovortices when compared to mesovortices originating in an ambient environment with deep layer shear below 20 m s^{-1}. From the operational and experimental MRMS product time-height cross sections, tornadic mesovortices are associated with a higher magnitude of AzShear and are shown to be approximately 2 km deeper relative to their non-tornadic counterpart at the median.

Similar to the ambient environments characterized by kinematics, only modest differences are found between tornadic and null mesovortices described in thermodynamic

variables (Fig. A.28). One hour prior to t_0, mesovortices that become tornadic during their lifetime reside in environments where the lapse rate at the most unstable level of free convection (MULFC) is 0.5 K km^{-1} lower compared to vortices that remain non-tornadic throughout their lifetime at the median (Fig. A.28a). Moreover, a smaller spread in the 0–1 km mean mixing ratio is evident in tornadic mesovortices, where most tornadic events manifest in mean 0–1 km mixing ratios between 10–15 g kg^{-1}. The majority of null events manifest in 0–1 km mean mixing ratio values between 8–16 g kg^{-1} (Fig. A.28b). Similar results about the spread are illustrated in θ_e (Fig. A.28c).

Surface-based convective available potential energy (SBCAPE) is nearly 250 J kg^{-1} higher in tornadic events relative to nulls at the median (Fig. A.28d). A near-uniform distribution exists for SBCAPE measured in the ambient environment one hour prior to t_0 in which tornadic mesovortices manifest. The resulting spread in measured SBCAPE values where the majority of tornadic mesovortices manifest in is between 200–1000 J kg^{-1}, noting the 25th and 75th percentiles, respectively. Contrarily, null mesovortices often manifest in two regimes of SBCAPE, noting a bi-modal distribution. The majority of null events tend to manifest when SBCAPE is below 250 J kg^{-1} while the secondary local maxima is in excess of 1000 J kg^{-1}. Both of these regimes are within the 25th and 75th percentile to that of tornadic events, noting an overlap in spread.

There exist modest differences in the ambient environment when diagnosing tornadic potential, yet these parameters illustrate overlap in their IQR. Following suit with Lovell and Parker (2022), the differences between parameters derived in the ambient environment of tornadic and nulls mesovortices are smaller than the magnitude of the fields themselves, offering little guidance in determining tornadic potential when used alone. A caveat to this analysis is that the RAP grids remain quite coarse in both the spatial and temporal dimension relative to the small-scale mesovortices that manifest within the parent QLCS. If lowered, it is possible that some environmental

parameters (i.e., MULFC lapse rate, SBCAPE, 0–6 km wind shear magnitude, and 0–3 km SRH) may offer skill in diagnosing tornadic potential. This effort will be part of future work.

Chapter 5

Summary and Conclusions

A total of 107 tornadic and 139 non-tornadic QLCS mesovortices stemming from 13 QLCS storms were tracked over the course of their lifetimes to statistically compare tornadic mesovortices from their non-tornadic counterpart using both operational and experimental MRMS products. For each QLCS storm, numerous WSR-88Ds surrounding each parent storm were blended onto a three dimensional grid space. Using the WSR-88D level II data, operational products such as AzShear and experimental MRMS products such as DivShear and total shear were computed onto the three-dimensional grid space using the suite of algorithms housed in the WDSS-II framework.

QLCS mesovortices were identified using AzShear01 and tracked forwards and backwards in time relative to t_0. In tornadic mesovortices, t_0 corresponds to the time at which the tornado was reported derived from the NWS DAT. In null mesovortices, t_0 corresponds to the time at which AzShear01 is maximized along the path of the vortex, noting peak-maturity in its measured cyclonic shear. This time essentially maximizing the probability for a tornado to occur, yet failed to do so given the absence of a tornado damage path in the NWS DAT.

To better understand the differences in mesovortex evolution leading up to successful or failed tornadogenesis, vertical profiles of both operational and experimental products were retained and statistically compared along the path of each vortex through time. However, due to the coarse spatial and temporal resolution of each WSR-88D used to generate the three-dimensional grid space of all products analyzed herein, true

vertical profiles of MRMS products may not fully represent the vortex itself. Therefore, the maximum value of each product is retained at all native height levels of the grid space within a 0.03° latitude by 0.03° longitude (∼3 km) box surrounding the mesovortex location to ensure that each profile is representative. The profiles for tornadic and null mesovortices are compared statistically by subtracting the median time-height cross section of each product.

5.0.1 Close-Proximity QLCS Mesovortices

Mesovortices retained in the dataset were split by distance relative to the nearest radar where close-proximity mesovortices reside within 75 km in range and far-proximity mesovortices reside in excess of 75 km in range. This was done to mitigate sampling biases (i.e., beam broadening and beam height) of each WSR-88D used in the blend.

In composite vertical time-height plots of azimuthal shear, close-proximity null mesovortices exhibit higher magnitudes of AzShear below 1 km AGL relative to tornadic mesovortices. However, close-proximity tornadic mesovortices exhibit deep transient plumes of significantly enhanced cyclonic rotation during the pre-tornadic phase, beginning approximately 50 minutes prior to t_0. Transient plumes of enhanced cyclonic shear of the same magnitude are absent in the median null mesovortex prior to t_0. The 0.006 s^{-1} isosurface of AzShear, used as a proxy to separate signal from noise, is nearly 1–2 km deeper in tornadic events relative to null events. This result keeps consistent with previous findings using single-radar analyses comparing tornadic and null QLCS mesovortices (e.g., Atkins et al., 2004, 2005), and especially in HSLC environments in the southeastern United States (e.g., Davis and Parker, 2014). Further, the multi-radar analyses is able to resolve the evolution about the depth of these mesovortices as well as illustrate signals of transient updraft pulses during the pre-tornadic phase, noted by plumes of enhanced cyclonic shear and convergent shear.

Approximately 20 minutes prior to t_0, the median azimuthal shear in both close-proximity tornadic and null mesovortices undergo a similar evolution in the lowest 3 km AGL where amplifications in AzShear are realized of similar magnitude. Consequently, in the context of this dataset, low-level layer maximum products of azimuthal shear (i.e., 0–1 km or 0–3 km) exhibit some ambiguity in distinguishing tornadic potential when used alone. Nonetheless, low-level layer-maximum azimuthal shear is highly effective in the identification of most QLCS mesovortices.

Close-proximity tornadic mesovortices display significantly higher DivShear during the period prior to t_0 relative to nulls, indicating that the transient plumes noted in AzShear might be correlated to rotating updraft pulses not observed at the same magnitude in null events. Beginning 20 minutes prior to t_0, tornadic mesovortices display maximum divergence in the 2–6 km AGL layer that persists throughout the tornadic and into the post-tornadic phase. However, 10 minutes prior to t_0, null mesovortices tend to display slightly higher near-ground divergence relative to tornadic mesovortices, yet both show an enhancement at the near-surface. This signal can indicative of near-ground acceleration in the horizontal wind field associated with a surge in outflow at the leading edge of the parent QLCS storm beginning just prior to t_0.

Close-proximity tornadic events are often characterized with significantly deeper convergence that extends beyond 10 km AGL starting 20 minutes prior to t_0 through their tornadic phase and afterwards. In the 20 minutes prior to t_0 in null events, deep columns of convergence at the same magnitude to that of tornadic mesovortices is absent at the median ($\sim$-0.003 s^{-1}). Below 2 km AGL from 60 minutes through 10 minutes prior to t_0, close-proximity null mesovortices often obtain higher convergent shear relative to tornadic mesovortices, albeit not a significant difference held at 95% confidence.

KDP in close-proximity tornadic events is often significantly higher relative to null events. This signal is illustrated both in the pre-tornadic phase, tornadic phase, and post-tornadic phase. High magnitudes of KDP are often shown aloft, extending upwards of 4 km AGL indicating that along with deep columns of cyclonic shear and divergent shear, the rotating updrafts are often characterized with higher volumes of hydrometeors acting to deflecting the beam by 2 deg km^{-1} or more below 4 km AGL, indicative of precipitation-loaded updraft pulses. This signal remains an absent feature in null mesovortices until 10 minutes prior to peak-maturity.

Following close-proximity tornadic mesovortices, the median Z_{DR} time-height cross section indicates a signal of decreasing Z_{DR} below 4 km AGL throughout the pre-tornadic phase while close-proximity nulls display a signal of increasing low-level Z_{DR} below 2 km AGL during the pre-maturity phase. Given deep transient plumes of enhanced convergent and cyclonic shear are shown along with a mere 250 J kg^{-1} of higher SBCAPE in the tornadic mesovortex distributions, it is plausible that the decreasing Z_{DR} signal can be indicative of size sorting. Further, high magnitudes of KDP on the order of 1.5-2 deg km^{-1} indicate that the resolved updrafts occur in regions of high precipitation concentration. Thus, updraft pulses during the pre-tornadic phase may act to loft hydrometeors away from the vicinity of the vortex, essentially lowering the Z_{DR} magnitude below 4 km AGL prior to t_0.

In the case of null events, updraft pulses are of lesser magnitude relative to their tornadic counterpart with a smaller magnitude of divergent shear atop the mesovortex at the median. Given an increase in Z_{DR} magnitude in the vicinity of these mesovortices, episodes of updraft pulses during the pre-maturity phase may not be as efficient when attempting to loft large hydrometeors away from the mesovortex center, leading to a high concentration of large hydrometeors below 2 km AGL beginning 30 minutes prior to peak maturity and onward.

5.0.2 Far-Proximity QLCS Mesovortices

In far-proximity QLCS mesovortices characterized by AzShear, tornadic events display higher AzShear relative to nulls below 3 km AGL beginning 60 minutes through 20 minutes prior to t_0. However, 10 minutes prior to t_0 an onward, null mesovortices obtain higher magnitudes of median AzShear below 3 km AGL. This signal persists throughout the time period after t_0. A similar feature between close and far-proximity QLCS mesovortices is that null events tend to display higher AzShear relative to their tornadic counterpart 10 minutes prior to t_0.

Two areas of amplified DivShear during the pre-tornadic phase are illustrated in far-proximity tornadic mesovortices. From 60 minutes through 20 minutes prior to t_0, far-proximity tornadic mesovortices illustrate amplified DivShear above 6 km AGL than transitions to the 0–4 km AGL layer 20 minutes prior to t_0 through t_0. In far-proximity nulls, DivShear of the same order of magnitude to that of tornadic mesovortices is shown below 1 km AGL, yet is more transient. The absence of enhanced median mid-to-upper level divergence in null events is a compelling difference relative to mesovortices with tornadic potential.

Tornadic mesovortices observed in far-proximity to the closest radar display transient plumes of enhanced convergent shear beginning 60 minutes through 30 minutes prior to t_0, indicative of transient rotating updraft pulses given given enhanced AzShear at the same period in time. In a similar fashion to close-proximity null events, far-proximity null events do not display enhanced convergent shear aloft, indicating shallower updraft pulses throughout the time period prior to t_0 given high near-surface convergent shear.

Further, a similar signal represented in Z_{DR} magnitude is shown in far-proximity mesovortices to that of close-proximity mesovortices. A signal in the median time-height cross section of Z_{DR} illustrates a decrease in magnitude below 4 km AGL while

null events associate with an increase in Z_{DR} magnitude below 2 km AGL. Given that signals showing transient updraft pulses are still resolved in far-proximity mesovortices, it is plausible that these updraft pulses may act to loft hydrometeors away from the vicinity of tornadic mesovortices retained in the dataset. Further, KDP magnitudes in excess of 1.5 deg km^{-1} can illustrate that these updraft pulses associated with tornadic mesovortices occur in regions of high precipitation concentration, a similar result to that of close-proximity mesovortices.

5.0.3 Product Correlations

To further quantify and illustrate trends able to distinguish tornadic potential in QLCS vortices, all three-dimensional products are integrated from 0.25 km AGL through 10 km AGL to produce a two-dimensional product such that all MRMS products analyzed can be correlated. A total of 552 unique combinations of products were correlated and linearly regressed to compare trends in the pre-tornadic evolution against the pre-maturity evolution. When correlating column-integrated AzShear with column-integrated spectrum width, it was found that the a distinct regime exists separating tornadic mesovortices that produce EF0 tornadoes from the rest of the dataset collected. When column-integrated AzShear falls below 0.04 s^{-1} in tandem with column-integrated spectrum width greater than 50 m s^{-1} at some instance(s) during the pre-tornadic phase, this signal is correlated highly for tornadic QLCS mesovortices that produce EF0 tornadoes. This signal is apparent in approximately 12 tornadic mesovortices (11% of all tornadic mesovortices retained) occurring in all regions of the CONUS except the central plains. However, only one QLCS storm was retained from the central plains. A larger sample size volume would bring higher confidence as to whether this signal remains unique for tornadic mesovortices that produce EF0 tornadoes.

5.0.4 RAP Analyses

One hour prior to t_0, it is found that the 0–3 and 0–6 km shear magnitude and 0–1 km and 0–3 km SRH differ the most between tornadic and null mesovortices regardless of proximity to the nearest radar. The 0–3 km and 0–6 km wind shear magnitude is approximately 5 and 7 m s^{-1} greater in the vicinity of tornadic mesovortices when compared to nulls, respectively at the median. The 0–1 km SRH and 0–3 km SRH magnitude is approximately 80 m^2 s^{-2} and 100 m^2 s^{-2} greater in the vicinity of tornadic mesovortices when compared to nulls, respectively at the median. However, these differences remain less than the actual values themselves indicating that kinematic environmental parameters may struggle to distinguish tornadic potential in QLCS mesovortices, similar to results described in Lovell and Parker (2022).

In terms of thermodynamic variables in the vicinity of tornadic and null mesovortices, the lapse rate at the most-unstable LFC is approximately 0.5 K km^{-1} higher in null events when compared to tornadic events at the median. This result can explain the suppressed and shallower updrafts in the minutes prior to t_0 shown through AzShear, DivShear and convergent shear noted in null events at the median. Further SBCAPE remains lower in null events, suppressing upward motions from parcels originating at the near-surface.

A much narrower distribution exists in terms of the 0–1 km mean mixing ratio in the vicinity of tornadic mesovortices where the IQR ranges from approximately 11–14 g kg^{-1}. The environment surrounding null events in the hour prior to t_0 displays a much wider distribution of 0–1 km mean mixing ratios, indicating high variability in terms of moisture content during the pre-maturity phase of these vortices.

Both surface θ_e and SBCAPE are quite similar between tornadic and null mesovortices at the median, yet SBCAPE is shown to take a much wider distribution of values in tornadic events ranging from 0 to just under 1000 J kg^{-1} derived from the bounds of

the IQR. Null events are characterized by a bi-modal distribution where the majority of null events typically manifest in SBCAPE below 500 J kg^{-1} while a second majority manifest above 1000 J kg^{-1}.

5.0.5 Operational Applications

Considerable variability exists with regard to all gridded MRMS products presented herein for both the retained tornadic and null QLCS mesovortices. This is especially true 10–15 minutes prior t_0, which may pose challenges for now-casting operations aimed at assessing tornadic potential in QLCS mesovortices in a real-time operational setting. The results offered herein can provide a unique set of tools that can support an increase in forecaster confidence when assessing tornadic potential in QLCS mesovortices which manifest along the leading edge of the identified system.

From the retained tornadic mesovortices, deeper columns of both convergent and cyclonic shear are present relative to their non-tornadic counterpart. Additionally, a signal illustrating sustained divergence is present in the 2–6 km (6–10 km AGL) AGL layer on the order of 0.003 s^{-1} in close-proximity (far-proximity) mesovortices. From this, future work would include the development of a rotational and divergence depth algorithm aimed at assessing the extent to which the dynamic response of a mesovortex is realized within the column using the multi-radar analysis. Further, this algorithm can be implemented into the WDSS-II framework which can be used in tandem with TORP (Sandmæl et al., 2023) or other machine learning algorithms in an effort to enhance probabilistic guidance on tornadic potential of QLCS mesovortices.

Reference List

Ashley, W., A. Haberlie, and J. Strohm, 2019: A climatology of quasi-linear convective systems and their hazards in the united states. *Weather and Forecasting*, **34**, https://doi.org/10.1175/WAF-D-19-0014.1.

Atkins, N. T., J. M. Arnott, R. W. Przybylinski, R. A. Wolf, and B. D. Ketcham, 2004: Vortex structure and evolution within bow echoes. part i: Single-doppler and damage analysis of the 29 june 1998 derecho. *Monthly Weather Review*, **132 (9)**, 2224 – 2242, https://doi.org/10.1175/1520-0493(2004)132⟨2224:VSAEWB⟩2.0.CO;2, URL https://journals.ametsoc.org/view/journals/mwre/132/9/1520-0493_2004_132_2224_vsaewb_2.0.co_2.xml.

Atkins, N. T., C. S. Bouchard, R. W. Przybylinski, R. J. Trapp, and G. Schmocker, 2005: Damaging surface wind mechanisms within the 10 june 2003 saint louis bow echo during bamex. *Monthly Weather Review*, **133 (8)**, 2275 – 2296, https://doi.org/10.1175/MWR2973.1, URL https://journals.ametsoc.org/view/journals/mwre/133/8/mwr2973.1.xml.

Atkins, N. T., and M. S. Laurent, 2009: Bow echo mesovortices. part ii: Their genesis. *Monthly Weather Review*, **137 (5)**, 1514 – 1532, https://doi.org/10.1175/2008MWR2650.1, URL https://journals.ametsoc.org/view/journals/mwre/137/5/2008mwr2650.1.xml.

Boyer, C. H., and J. M. L. Dahl, 2020: The mechanisms responsible for large near-surface vertical vorticity within simulated supercells and quasi-linear storms. *Monthly Weather Review*, **148 (10)**, 4281 – 4297, https://doi.org/10.1175/MWR-D-20-0082.1, URL https://journals.ametsoc.org/view/journals/mwre/148/10/mwrD200082.xml.

Brotzge, J. A., S. E. Nelson, R. L. Thompson, and B. T. Smith, 2013: Tornado probability of detection and lead time as a function of convective mode and environmental parameters. *Weather and Forecasting*, **28 (5)**, 1261 – 1276, https://doi.org/https://doi.org/10.1175/WAF-D-12-00119.1, URL https://journals.ametsoc.org/view/journals/wefo/28/5/waf-d-12-00119_1.xml.

Brown, R. A., V. T. Wood, and D. Sirmans, 2000: Improved wsr-88d scanning strategies for convective storms. *Weather and Forecasting*, **15 (2)**, 208 – 220, https://doi.org/10.1175/1520-0434(2000)015⟨0208:IWSSFC⟩2.0.CO;2, URL https://journals.ametsoc.org/view/journals/wefo/15/2/1520-0434_2000_015_0208_iwssfc_2_0_co_2.xml.

Buban, M. S., and C. L. Ziegler, 2016: The formation of small-scale atmospheric vortices via horizontal shearing instability. *Journal of the Atmospheric Sciences*,

73 (5), 2061 – 2084, https://doi.org/10.1175/JAS-D-14-0355.1, URL https://journals.ametsoc.org/view/journals/atsc/73/5/jas-d-14-0355.1.xml.

Conrad, D. M., and K. R. Knupp, 2019: Doppler radar observations of horizontal shearing instability in quasi-linear convective systems. *Monthly Weather Review*, **147 (4)**, 1297 – 1318, https://doi.org/10.1175/MWR-D-18-0257.1, URL https://journals.ametsoc.org/view/journals/mwre/147/4/mwr-d-18-0257.1.xml.

Conway, J. W., and K. D. Hondl, 1997: Minimizing the doppler dilemma using a unique redundant scanning strategy and multiple pulse repetition frequency dealiasing algorithm. *Preprints: 28th Conference on Radar Meteorology*, American Meteorological Society, Austin, TX,, 315–316.

Dahl, J. M. L., M. D. Parker, and L. J. Wicker, 2012: Uncertainties in trajectory calculations within near-surface mesocyclones of simulated supercells. *Monthly Weather Review*, **140 (9)**, 2959 – 2966, https://doi.org/https://doi.org/10.1175/MWR-D-12-00131.1, URL https://journals.ametsoc.org/view/journals/mwre/140/9/mwr-d-12-00131.1.xml.

Dahl, J. M. L., M. D. Parker, and L. J. Wicker, 2014: Imported and storm-generated near-ground vertical vorticity in a simulated supercell. *Journal of the Atmospheric Sciences*, **71 (8)**, 3027 – 3051, https://doi.org/https://doi.org/10.1175/JAS-D-13-0123.1, URL https://journals.ametsoc.org/view/journals/atsc/71/8/jas-d-13-0123.1.xml.

Davies-Jones, R., 2000: A lagrangian model for baroclinic genesis of mesoscale vortices. part i: Theory. *Journal of the Atmospheric Sciences*, **57 (5)**, 715 – 736, https://doi.org/10.1175/1520-0469(2000)057⟨0715:ALMFBG⟩2.0.CO;2, URL https://journals.ametsoc.org/view/journals/atsc/57/5/1520-0469_2000_057_0715_almfbg_2.0.co_2.xml.

Davies-Jones, R., 2021: Invented forces in supercell models. *Journal of the Atmospheric Sciences*, **78 (9)**, 2927 – 2939, https://doi.org/https://doi.org/10.1175/JAS-D-21-0082.1, URL https://journals.ametsoc.org/view/journals/atsc/78/9/JAS-D-21-0082.1.xml.

Davies-Jones, R., and H. Brooks, 1993: *Mesocyclogenesis from a Theoretical Perspective*, 105–114. American Geophysical Union (AGU), https://doi.org/https://doi.org/10.1029/GM079p0105, URL https://agupubs.onlinelibrary.wiley.com/doi/abs/10.1029/GM079p0105, https://agupubs.onlinelibrary.wiley.com/doi/pdf/10.1029/GM079p0105.

Davies-Jones, R., R. J. Trapp, and H. B. Bluestein, 2001: *Tornadoes and Tornadic Storms*, 167–221. American Meteorological Society, Boston, MA, https://doi.org/10.1007/978-1-935704-06-5_5, URL https://doi.org/10.1007/978-1-935704-06-5_5.

Davis, C., and Coauthors, 2004: The bow echo and mcv experiment: Observations and opportunities: Observations and opportunities. *Bulletin of the American Meteorological Society*, **85 (8)**, 1075 – 1094, https://doi.org/https://doi.org/10.1175/BAMS-85-8-1075, URL https://journals.ametsoc.org/view/journals/bams/85/8/bams-85-8-1075.xml.

Davis, C. A., and T. J. Galarneau, 2009: The vertical structure of mesoscale convective vortices. *Journal of the Atmospheric Sciences*, **66 (3)**, 686 – 704, https://doi.org/10.1175/2008JAS2819.1, URL https://journals.ametsoc.org/view/journals/atsc/66/3/2008jas2819.1.xml.

Davis, J. M., and M. D. Parker, 2014: Radar climatology of tornadic and nontornadic vortices in high-shear, low-cape environments in the mid-atlantic and southeastern united states. *Weather and Forecasting*, **29 (4)**, 828 – 853, https://doi.org/10.1175/WAF-D-13-00127.1, URL https://journals.ametsoc.org/view/journals/wefo/29/4/waf-d-13-00127_1.xml.

Dial, G. L., J. P. Racy, and R. L. Thompson, 2010: Short-term convective mode evolution along synoptic boundaries. *Weather and Forecasting*, **25 (5)**, 1430 – 1446, https://doi.org/10.1175/2010WAF2222315.1, URL https://journals.ametsoc.org/view/journals/wefo/25/5/2010waf2222315_1.xml.

Flournoy, M. D., and M. C. Coniglio, 2019: Origins of vorticity in a simulated tornadic mesovortex observed during pecan on 6 july 2015. *Monthly Weather Review*, **147 (1)**, 107 – 134, https://doi.org/10.1175/MWR-D-18-0221.1, URL https://journals.ametsoc.org/view/journals/mwre/147/1/mwr-d-18-0221.1.xml.

Flournoy, M. D., A. W. Lyza, M. A. Satrio, M. R. Diedrichsen, M. C. Coniglio, and S. Waugh, 2022: A climatology of cell mergers with supercells and their association with mesocyclone evolution. *Monthly Weather Review*, **150 (2)**, 451 – 461, https://doi.org/https://doi.org/10.1175/MWR-D-21-0204.1, URL https://journals.ametsoc.org/view/journals/mwre/150/2/MWR-D-21-0204.1.xml.

Forbes, G. S., and R. M. Wakimoto, 1983: A concentrated outbreak of tornadoes, downbursts and microbursts, and implications regarding vortex classification. *Monthly Weather Review*, **111 (1)**, 220 – 236, https://doi.org/10.1175/1520-0493(1983)111⟨0220:ACOOTD⟩2.0.CO;2, URL https://journals.ametsoc.org/view/journals/mwre/111/1/1520-0493_1983_111_0220_acootd_2_0_co_2.xml.

Funk, T. W., K. E. Darmofal, J. D. Kirkpatrick, V. L. DeWald, R. W. Przybylinski, G. K. Schmocker, and Y.-J. Lin, 1999: Storm reflectivity and mesocyclone evolution associated with the 15 april 1994 squall line over kentucky and southern indiana. *Weather and Forecasting*, **14 (6)**, 976 – 993, https://doi.org/10.1175/1520-0434(1999)014⟨0976:SRAMEA⟩2.0.CO;2, URL https://journals.ametsoc.org/view/journals/wefo/14/6/1520-0434_1999_014_0976_sramea_2_0_co_2.xml.

Giangrande, S., and A. V. Ryzhkov, 2003: The quality of rainfall estimation with the polarimetric wsr-88d radar as a function of range. *31st International Conference on Radar Meteorology*, American Meteorological Society, Seattle, WA, 357–360.

Gibbs, J. G., 2021: Evaluating precursor signals for qlcs tornado and higher impact straight-line wind events. *Journal of Operational Meteorology*, **9 (5)**, 62 – 75, https://doi.org/https://doi.org/10.15191/nwajom.2021.0905, URL https://repository.library.noaa.gov/view/noaa/33475/noaa_33475_DS1.pdf.

Goodnight, J. S., D. A. Chehak, and R. J. Trapp, 2022: Quantification of qlcs tornadogenesis, associated characteristics, and environments across a large sample. *Weather and Forecasting*, **37 (11)**, 2087 – 2105, https://doi.org/10.1175/WAF-D-22-0016.1, URL https://journals.ametsoc.org/view/journals/wefo/37/11/WAF-D-22-0016.1.xml.

Gorgucci, E., and L. Baldini, 2015: Influence of beam broadening on the accuracy of radar polarimetric rainfall estimation. *Journal of Hydrometeorology*, **16 (3)**, 1356 – 1371, https://doi.org/https://doi.org/10.1175/JHM-D-14-0084.1, URL https://journals.ametsoc.org/view/journals/hydr/16/3/jhm-d-14-0084_1.xml.

Heikenfeld, M., P. J. Marinescu, M. Christensen, D. Watson-Parris, F. Senf, S. C. van den Heever, and P. Stier, 2019: tobac 1.2: towards a flexible framework for tracking and analysis of clouds in diverse datasets. *Geoscientific Model Development*, **12 (11)**, 4551–4570, https://doi.org/10.5194/gmd-12-4551-2019, URL https://gmd.copernicus.org/articles/12/4551/2019/.

Heinselman, P. L., D. L. Priegnitz, K. L. Manross, T. M. Smith, and R. W. Adams, 2008: Rapid sampling of severe storms by the national weather radar testbed phased array radar. *Weather and Forecasting*, **23 (5)**, 808 – 824, https://doi.org/https://doi.org/10.1175/2008WAF2007071.1, URL https://journals.ametsoc.org/view/journals/wefo/23/5/2008waf2007071_1.xml.

Houser, J. L., H. B. Bluestein, K. Thiem, J. Snyder, D. Reif, and Z. Wienhoff, 2022: Additional evaluation of the spatiotemporal evolution of rotation during tornadogenesis using rapid-scan mobile radar observations. *Monthly Weather Review*, **150 (7)**, 1639 – 1666, https://doi.org/https://doi.org/10.1175/MWR-D-21-0227.1, URL https://journals.ametsoc.org/view/journals/mwre/150/7/MWR-D-21-0227.1.xml.

Jing, Z., and G. Wiener, 1993: Two-dimensional dealiasing of doppler velocities. *Journal of Atmospheric and Oceanic Technology*, **10 (6)**, 798 – 808, https://doi.org/https://doi.org/10.1175/1520-0426(1993)010⟨0798:TDDODV⟩2.0.CO;2, URL https://journals.ametsoc.org/view/journals/atot/10/6/1520-0426_1993_010_0798_tddodv_2_0_co_2.xml.

Lakshmanan, V., T. Smith, K. Hondl, G. J. Stumpf, and A. Witt, 2006: A real-time, three-dimensional, rapidly updating, heterogeneous radar merger technique for reflectivity, velocity, and derived products. *Weather and Forecasting*, **21 (5)**, 802 – 823, https://doi.org/https://doi.org/10.1175/WAF942.1, URL https://journals.ametsoc.org/view/journals/wefo/21/5/waf942_1.xml.

Lakshmanan, V., T. Smith, G. Stumpf, and K. Hondl, 2007: The warning decision support system–integrated information. *Weather and Forecasting*, **22 (3)**, 596 – 612, https://doi.org/10.1175/WAF1009.1, URL https://journals.ametsoc.org/view/journals/wefo/22/3/waf1009_1.xml.

Lee, B. D., and R. B. Wilhelmson, 1997a: The numerical simulation of non-supercell tornadogenesis. part i: Initiation and evolution of pretornadic misocyclone circulations along a dry outflow boundary. *Journal of the Atmospheric Sciences*, **54 (1)**, 32 – 60, https://doi.org/10.1175/1520-0469(1997)054⟨0032:TNSONS⟩2.0.CO;2, URL https://journals.ametsoc.org/view/journals/atsc/54/1/1520-0469_1997_054_0032_tnsons_2.0.co_2.xml.

Lee, B. D., and R. B. Wilhelmson, 1997b: The numerical simulation of nonsupercell tornadogenesis. part ii: Evolution of a family of tornadoes along a weak outflow boundary. *Journal of the Atmospheric Sciences*, **54 (19)**, 2387 – 2415, https://doi.org/10.1175/1520-0469(1997)054⟨2387:TNSONT⟩2.0.CO;2, URL https://journals.ametsoc.org/view/journals/atsc/54/19/1520-0469_1997_054_2387_tnsont_2.0.co_2.xml.

Losey-Bailor, A., W. D. Zittel, and Z. Jing, 2019: Improving doppler velocity coverage on the wsr-88d by using low prfs with 2dvda. 3 – 25, URL https://www.roc.noaa.gov/wsr88d/PublicDocs/Publications/Losey-BailorEtAl2019_ImprovingDoppVelCoverageLowPRFs_39thICRM.pdf.

Lovell, L. T., and M. D. Parker, 2022: Simulated qlcs vortices in a high-shear, low-cape environment. *Weather and Forecasting*, **37 (6)**, 989 – 1012, https://doi.org/10.1175/WAF-D-21-0133.1, URL https://journals.ametsoc.org/view/journals/wefo/37/6/WAF-D-21-0133.1.xml.

Mahale, V. N., J. A. Brotzge, and H. B. Bluestein, 2012: An analysis of vortices embedded within a quasi-linear convective system using x-band polarimetric radar. *Weather and Forecasting*, **27 (6)**, 1520 – 1537, https://doi.org/10.1175/WAF-D-11-00135.1, URL https://journals.ametsoc.org/view/journals/wefo/27/6/waf-d-11-00135_1.xml.

Mahalik, M. C., B. R. Smith, K. L. Elmore, D. M. Kingfield, K. L. Ortega, and T. M. Smith, 2019: Estimates of gradients in radar moments using a linear least squares derivative technique. *Weather and Forecasting*, **34 (2)**, 415 – 434, https://doi.org/https://doi.org/10.1175/WAF-D-18-0095.1, URL https://journals.ametsoc.org/view/journals/wefo/34/2/waf-d-18-0095_1.xml.

Marion, G. R., and R. J. Trapp, 2021: Controls of quasi-linear convective system tornado intensity. *Journal of the Atmospheric Sciences*, **78 (4)**, 1189 – 1205, https://doi.org/10.1175/JAS-D-20-0164.1, URL https://journals.ametsoc.org/view/journals/atsc/78/4/JAS-D-20-0164.1.xml.

Markowski, P., and Coauthors, 2012: The pretornadic phase of the goshen county, wyoming, supercell of 5 june 2009 intercepted by vortex2. part ii: Intensification of low-level rotation. *Monthly Weather Review*, **140 (9)**, 2916 – 2938, https://doi.org/10.1175/MWR-D-11-00337.1, URL https://journals.ametsoc.org/view/journals/mwre/140/9/mwr-d-11-00337.1.xml.

Markowski, P. M., and Y. P. Richardson, 2014: The influence of environmental low-level shear and cold pools on tornadogenesis: Insights from idealized simulations. *Journal of the Atmospheric Sciences*, **71 (1)**, 243 – 275, https://doi.org/https://doi.org/10.1175/JAS-D-13-0159.1, URL https://journals.ametsoc.org/view/journals/atsc/71/1/jas-d-13-0159.1.xml.

Przybylinski, R. W., 1995: The bow echo: Observations, numerical simulations, and severe weather detection methods. *Weather and Forecasting*, **10 (2)**, 203 – 218, https://doi.org/10.1175/1520-0434(1995)010⟨0203:TBEONS⟩2.0.CO;2, URL https://journals.ametsoc.org/view/journals/wefo/10/2/1520-0434_1995_010_0203_tbeons_2_0_co_2.xml.

Roberts, B., M. Xue, A. D. Schenkman, and D. T. Dawson, 2016: The role of surface drag in tornadogenesis within an idealized supercell simulation. *Journal of the Atmospheric Sciences*, **73 (9)**, 3371 – 3395, https://doi.org/https://doi.org/10.1175/JAS-D-15-0332.1, URL https://journals.ametsoc.org/view/journals/atsc/73/9/jas-d-15-0332.1.xml.

Rotunno, R., P. M. Markowski, and G. H. Bryan, 2017: "near ground" vertical vorticity in supercell thunderstorm models. *Journal of the Atmospheric Sciences*, **74 (6)**, 1757 – 1766, https://doi.org/https://doi.org/10.1175/JAS-D-16-0288.1, URL https://journals.ametsoc.org/view/journals/atsc/74/6/jas-d-16-0288.1.xml.

Ryzhkov, A. V., 2007: The impact of beam broadening on the quality of radar polarimetric data. *Journal of Atmospheric and Oceanic Technology*, **24 (5)**, 729 – 744, https://doi.org/https://doi.org/10.1175/JTECH2003.1, URL https://journals.ametsoc.org/view/journals/atot/24/5/jtech2003_1.xml.

Sandmæl, T. N., and Coauthors, 2023: The tornado probability algorithm: A probabilistic machine learning tornadic circulation detection algorithm. *Weather and Forecasting*, https://doi.org/10.1175/WAF-D-22-0123.1, URL https://journals.ametsoc.org/view/journals/wefo/aop/WAF-D-22-0123.1/WAF-D-22-0123.1.xml.

Schaumann, J. S., and R. W. Przybylinski, 2012: Operational application of 0–3 km bulk shear vectors in assessing quasi linear convective system mesovortex and tornado

potential. American Meteorological Society, Nashville, TN, USA, 142, URL https://ams.confex.com/ams/26SLS/webprogram/Paper212008.html.

Schenkman, A., and M. Xue, 2015: Bow-echo mesovortices: A review. *Atmospheric Research*, **170**, https://doi.org/10.1016/j.atmosres.2015.11.003.

Schenkman, A. D., M. Xue, and M. Hu, 2014: Tornadogenesis in a high-resolution simulation of the 8 may 2003 oklahoma city supercell. *Journal of the Atmospheric Sciences*, **71 (1)**, 130 – 154, https://doi.org/10.1175/JAS-D-13-073.1, URL https://journals.ametsoc.org/view/journals/atsc/71/1/jas-d-13-073.1.xml.

Schenkman, A. D., M. Xue, and A. Shapiro, 2012: Tornadogenesis in a simulated mesovortex within a mesoscale convective system. *Journal of the Atmospheric Sciences*, **69 (11)**, 3372 – 3390, https://doi.org/10.1175/JAS-D-12-038.1, URL https://journals.ametsoc.org/view/journals/atsc/69/11/jas-d-12-038.1.xml.

Smith, B. T., R. L. Thompson, J. S. Grams, C. Broyles, and H. E. Brooks, 2012: Convective modes for significant severe thunderstorms in the contiguous united states. part i: Storm classification and climatology. *Weather and Forecasting*, **27 (5)**, 1114 – 1135, https://doi.org/https://doi.org/10.1175/WAF-D-11-00115.1, URL https://journals.ametsoc.org/view/journals/wefo/27/5/waf-d-11-00115_1.xml.

Smith, T., and K. Elmore, 2004: The use of radial velocity derivatives to diagnose rotation and divergence. *11th Conference on Aviation, Range, and Aerospace*, Hyannis, MA, American Meteorological Society, P5.6.

Smith, T. M., and Coauthors, 2016a: Multi-radar multi-sensor (mrms) severe weather and aviation products: Initial operating capabilities. *Bulletin of the American Meteorological Society*, **97 (9)**, 1617 – 1630, https://doi.org/10.1175/BAMS-D-14-00173.1, URL https://journals.ametsoc.org/view/journals/bams/97/9/bams-d-14-00173.1.xml.

Smith, T. M., and Coauthors, 2016b: Multi-radar multi-sensor (mrms) severe weather and aviation products: Initial operating capabilities. *Bulletin of the American Meteorological Society*, **97 (9)**, 1617 – 1630, https://doi.org/https://doi.org/10.1175/BAMS-D-14-00173.1, URL https://journals.ametsoc.org/view/journals/bams/97/9/bams-d-14-00173.1.xml.

Tarjan, R., 1972: Depth-first search and linear graph algorithms. *SIAM Journal on Computing*, **1 (2)**, 146–160, https://doi.org/10.1137/0201010, URL https://doi.org/10.1137/0201010.

Thompson, R. L., 2023: A comparison of right-moving supercell and quasi-linear convective system tornadoes in the contiguous united states 2003–2021. *Weather and Forecasting*, https://doi.org/https://doi.org/10.1175/WAF-D-23-0006.

1, URL https://journals.ametsoc.org/view/journals/wefo/aop/WAF-D-23-0006.1/WAF-D-23-0006.1.xml.

Tochimoto, E., and H. Niino, 2022: Tornadogenesis in a quasi-linear convective system over kanto plain in japan: A numerical case study. *Monthly Weather Review*, **150 (1)**, 259 – 282, https://doi.org/10.1175/MWR-D-20-0402.1, URL https://journals.ametsoc.org/view/journals/mwre/150/1/MWR-D-20-0402.1.xml.

Trapp, R. J., E. D. Mitchell, G. A. Tipton, D. W. Effertz, A. I. Watson, D. L. Andra, and M. A. Magsig, 1999: Descending and nondescending tornadic vortex signatures detected by wsr-88ds. *Weather and Forecasting*, **14 (5)**, 625 – 639, https://doi.org/https://doi.org/10.1175/1520-0434(1999)014⟨0625:DANTVS⟩2.0.CO;2, URL https://journals.ametsoc.org/view/journals/wefo/14/5/1520-0434_1999_014_0625_dantvs_2_0_co_2.xml.

Trapp, R. J., S. A. Tessendorf, E. S. Godfrey, and H. E. Brooks, 2005: Tornadoes from squall lines and bow echoes. part i: Climatological distribution. *Weather and Forecasting*, **20 (1)**, 23 – 34, https://doi.org/https://doi.org/10.1175/WAF-835.1, URL https://journals.ametsoc.org/view/journals/wefo/20/1/waf-835_1.xml.

Trapp, R. J., and M. L. Weisman, 2003: Low-level mesovortices within squall lines and bow echoes. part ii: Their genesis and implications. *Monthly Weather Review*, **131 (11)**, 2804 – 2823, https://doi.org/10.1175/1520-0493(2003)131⟨2804:LMWSLA⟩2.0.CO;2, URL https://journals.ametsoc.org/view/journals/mwre/131/11/1520-0493_2003_131_2804_lmwsla_2.0.co_2.xml.

Ungar, M., 2022: Using radiosonde observations to assess the 'three-ingredients' method to forecast qlcs mesovortices. M.S. thesis, University of Oklahoma, 1866 pp.

van der Walt, S., and Coauthors, 2014: scikit-image: image processing in Python. *PeerJ*, **2**, e453, https://doi.org/10.7717/peerj.453, URL https://doi.org/10.7717/peerj.453.

Wakimoto, R. M., H. V. Murphey, C. A. Davis, and N. T. Atkins, 2006: High winds generated by bow echoes. part ii: The relationship between the mesovortices and damaging straight-line winds. *Monthly Weather Review*, **134 (10)**, 2813 – 2829, https://doi.org/https://doi.org/10.1175/MWR3216.1, URL https://journals.ametsoc.org/view/journals/mwre/134/10/mwr3216.1.xml.

Weisman, M. L., and C. A. Davis, 1998: Mechanisms for the generation of mesoscale vortices within quasi-linear convective systems. *Journal of the Atmospheric Sciences*, **55 (16)**, 2603 – 2622, https://doi.org/10.1175/1520-0469(1998)055⟨2603:MFTGOM⟩2.0.CO;2, URL https://journals.ametsoc.org/view/journals/atsc/55/16/1520-0469_1998_055_2603_mftgom_2.0.co_2.xml.

Weisman, M. L., and R. J. Trapp, 2003: Low-level mesovortices within squall lines and bow echoes. part i: Overview and dependence on environmental shear. *Monthly Weather Review*, **131 (11)**, 2779 – 2803, https://doi.org/10.1175/1520-0493(2003)131⟨2779:LMWSLA⟩2.0.CO;2, URL https://journals.ametsoc.org/view/journals/mwre/131/11/1520-0493_2003_131_2779_lmwsla_2.0.co_2.xml.

Wheatley, D. M., and R. J. Trapp, 2008: The effect of mesoscale heterogeneity on the genesis and structure of mesovortices within quasi-linear convective systems. *Monthly Weather Review*, **136 (11)**, 4220 – 4241, https://doi.org/https://doi.org/10.1175/2008MWR2294.1, URL https://journals.ametsoc.org/view/journals/mwre/136/11/2008mwr2294.1.xml.

Xu, X., M. Xue, and Y. Wang, 2015: The genesis of mesovortices within a real-data simulation of a bow echo system. *Journal of the Atmospheric Sciences*, **72 (5)**, 1963 – 1986, https://doi.org/10.1175/JAS-D-14-0209.1, URL https://journals.ametsoc.org/view/journals/atsc/72/5/jas-d-14-0209.1.xml.

1 Figures

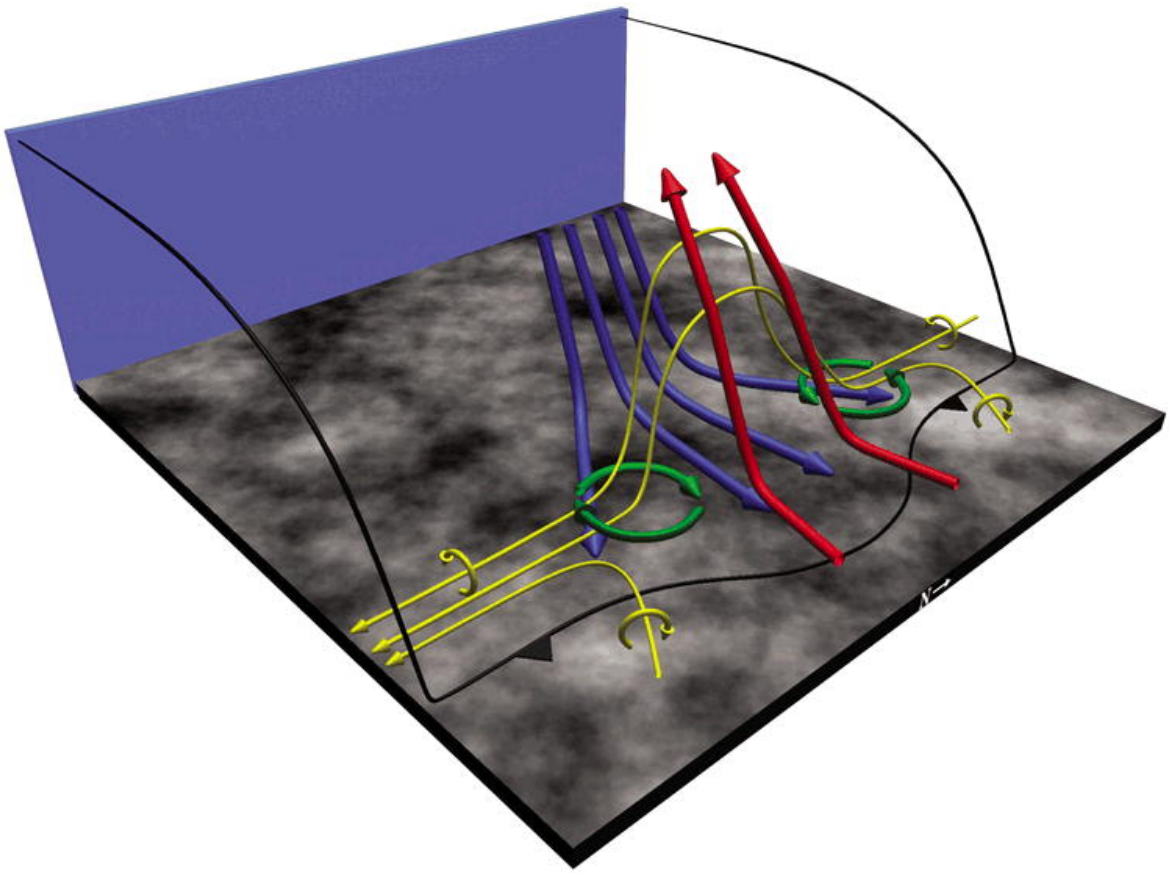

Figure A.1: A schematic of cyclonic-anticyclonic mesovortexgenesis in QLCS storms via upward vortex-line tilting adapted from figure 16 of Atkins and Laurent (2009). Vortex lines are represented in gold, the inflow and updraft denoted in red, and the downdraft in blue. The green arrow is representative of the mesovortex and the gust front position is annotated in black.

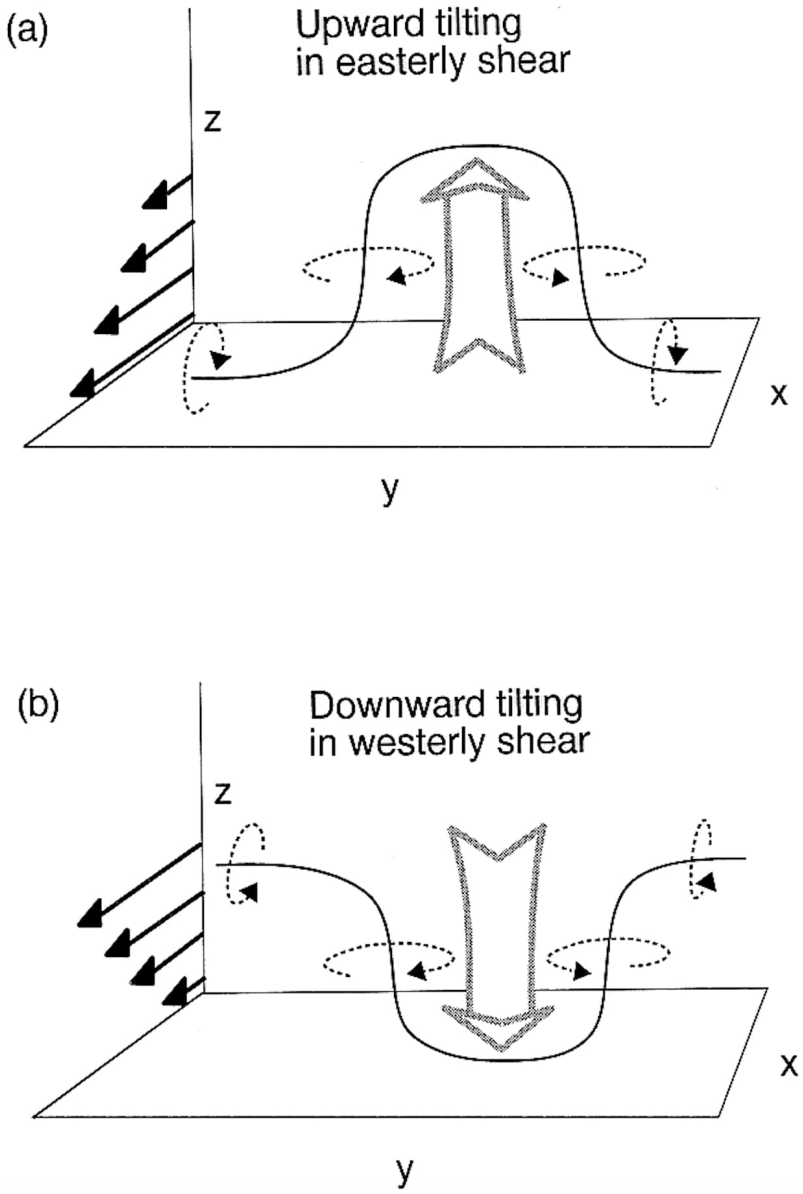

Figure A.2: Schematic of QLCS mesovortexgenesis through upward vortex-line tilting in (a) easterly shear where the cyclonic (anticyclonic) member resides to the north (south) of the updraft and (b) downward vortex-line tilting in westerly shear where the cyclonic (anticyclonic) member resides to the north (south) of the downward forcing. Adapted from Weisman and Davis (1998) as their figure 5.

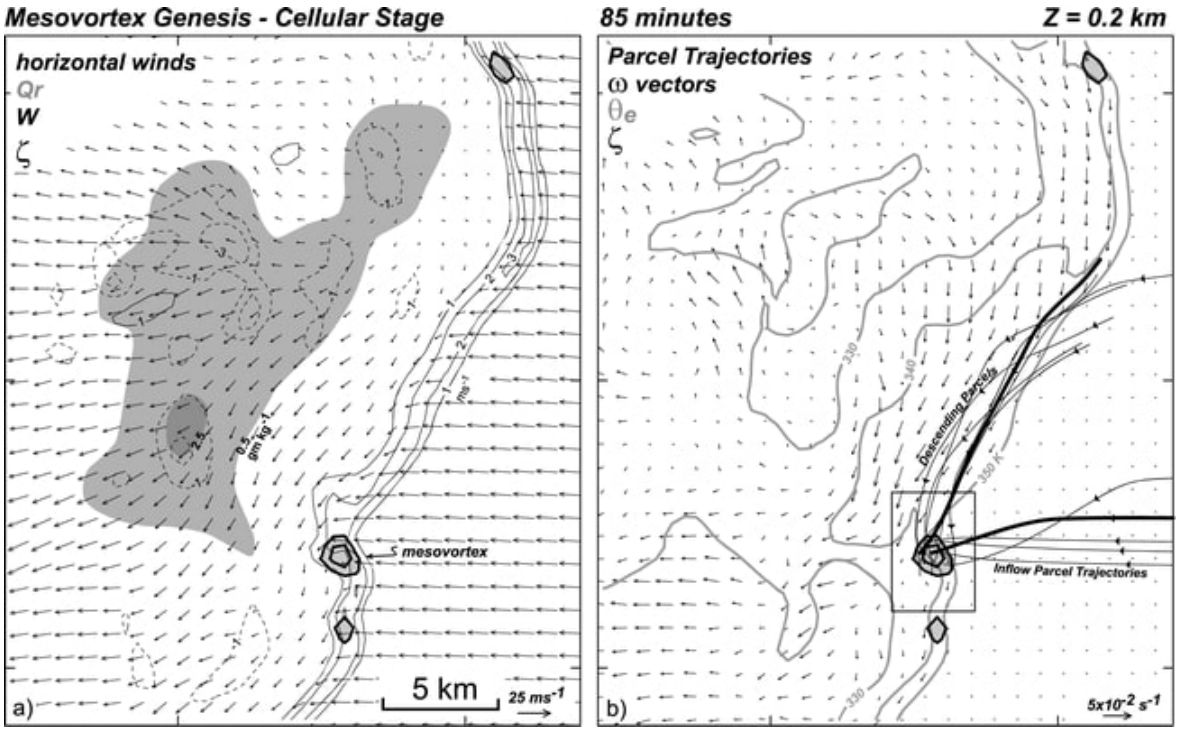

Figure A.3: A cyclonic-only mesovortex adapted from Atkins and Laurent (2009) figure 3. (a) Rainwater mixing ratio (g kg^{-1}) is shown in grey shading. Contoured vertical velocity in m s^{-1} with thin dashed lines representing negative values and solid lines representing positive values. Vertical vorticity is shown in thick solid contours beginning and incremented at 1×10^{-2} s^{-1}. Horizontal wind vectors are also included. (b) Equivalent potential temperature (K) is contoured in grey. Air parcel trajectories projected at 0.2 km are shown (solid black). The vector field represents horizontal vorticity and is plotted as in (a). All fields in both (a) and (b) are plotted at 0.2 km AGL.

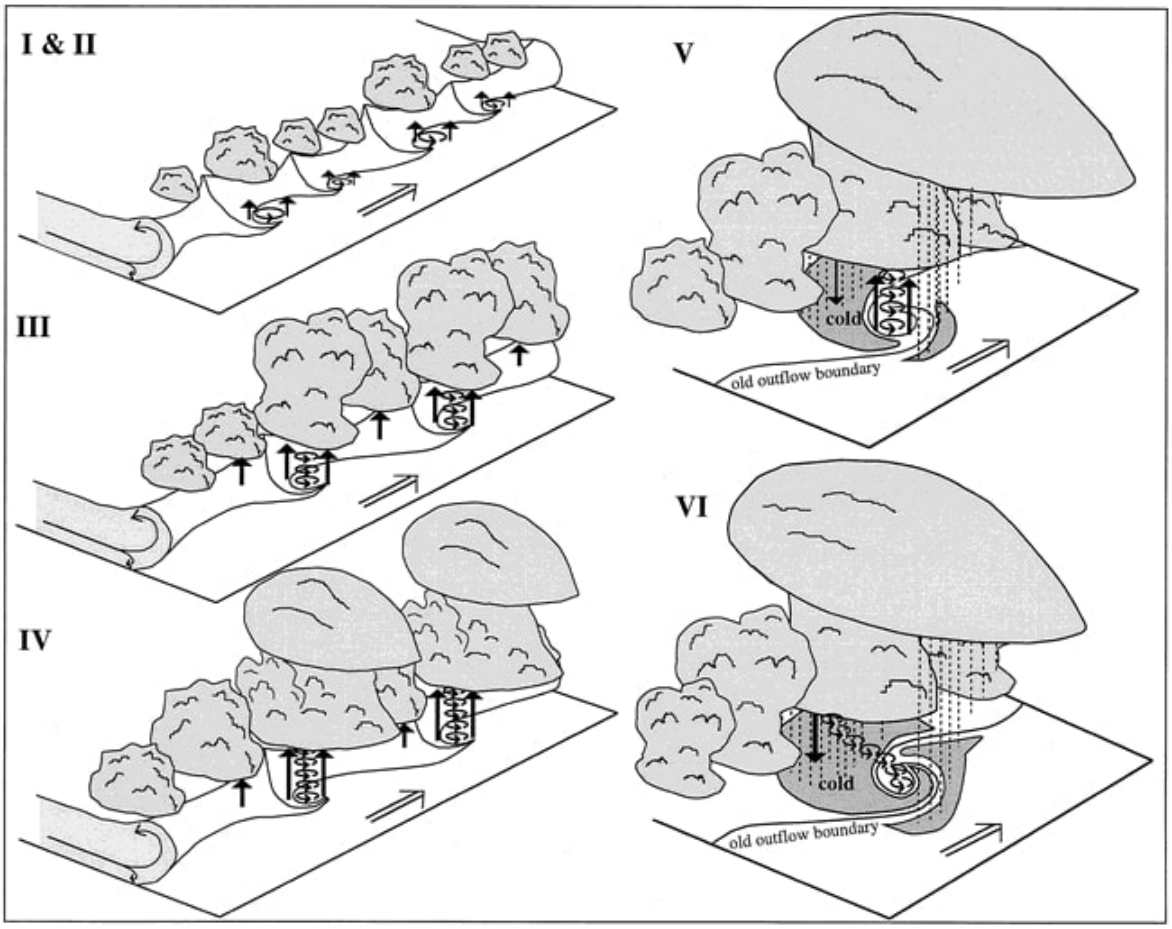

Figure A.4: Schematic of mesovortexgenesis and subsequent tornadogensis through the release of horizontal shearing instability (HSI). The viewing perspective is looking northwest from an elevated position. Adapted from Lee and Wilhelmson (1997b) as their figure 24.

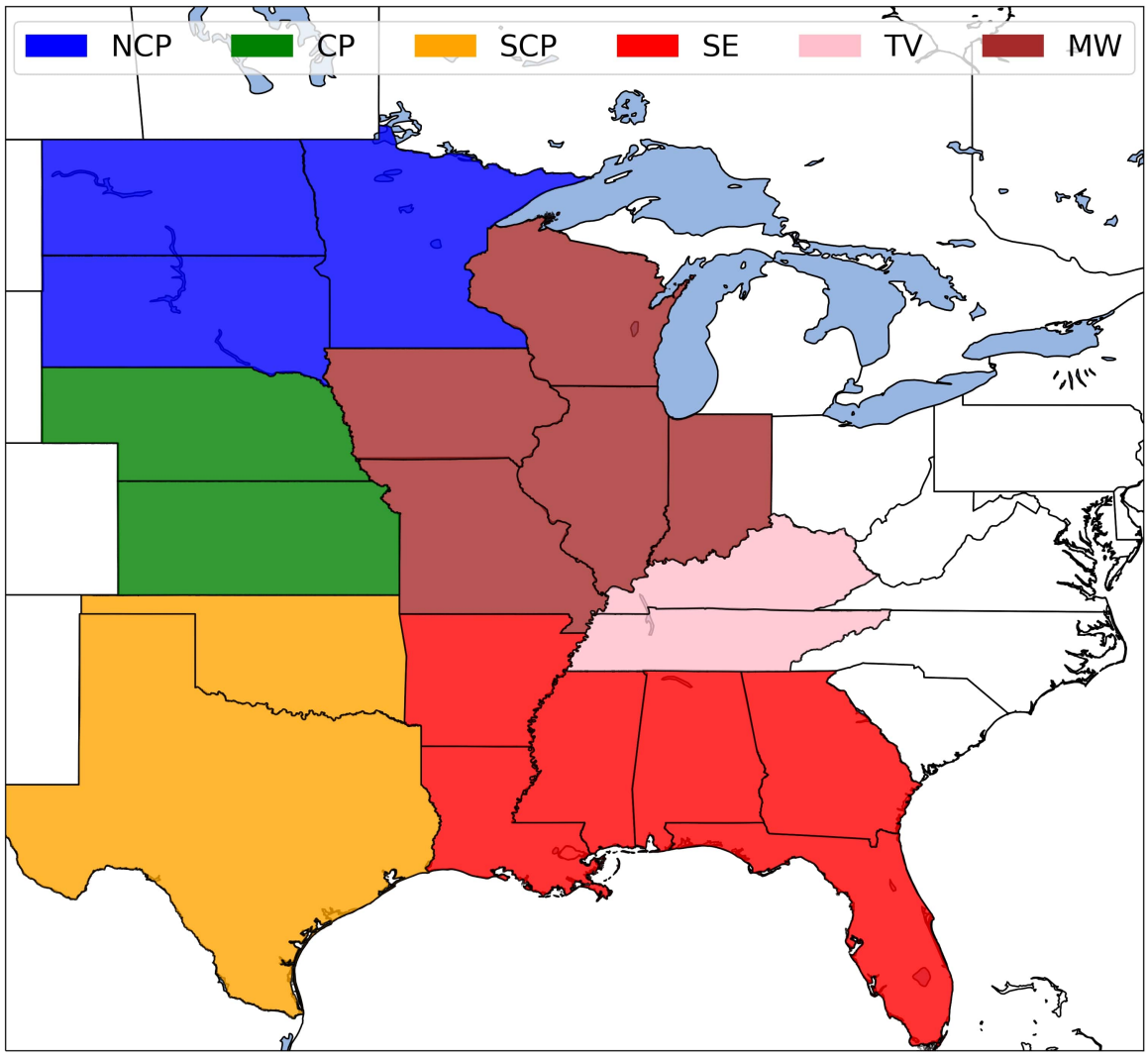

Figure A.5: Regions of the Continental United States (CONUS) which include the North Central Plains (NCP; blue), Central Plains (CP; green), South Central Plains (SCP; gold), Southeast (SE; red), Tennessee Valley (TV; pink), and Midwest (MW; brown) used to classify regions of all QLCS mesovortices retained in the dataset.

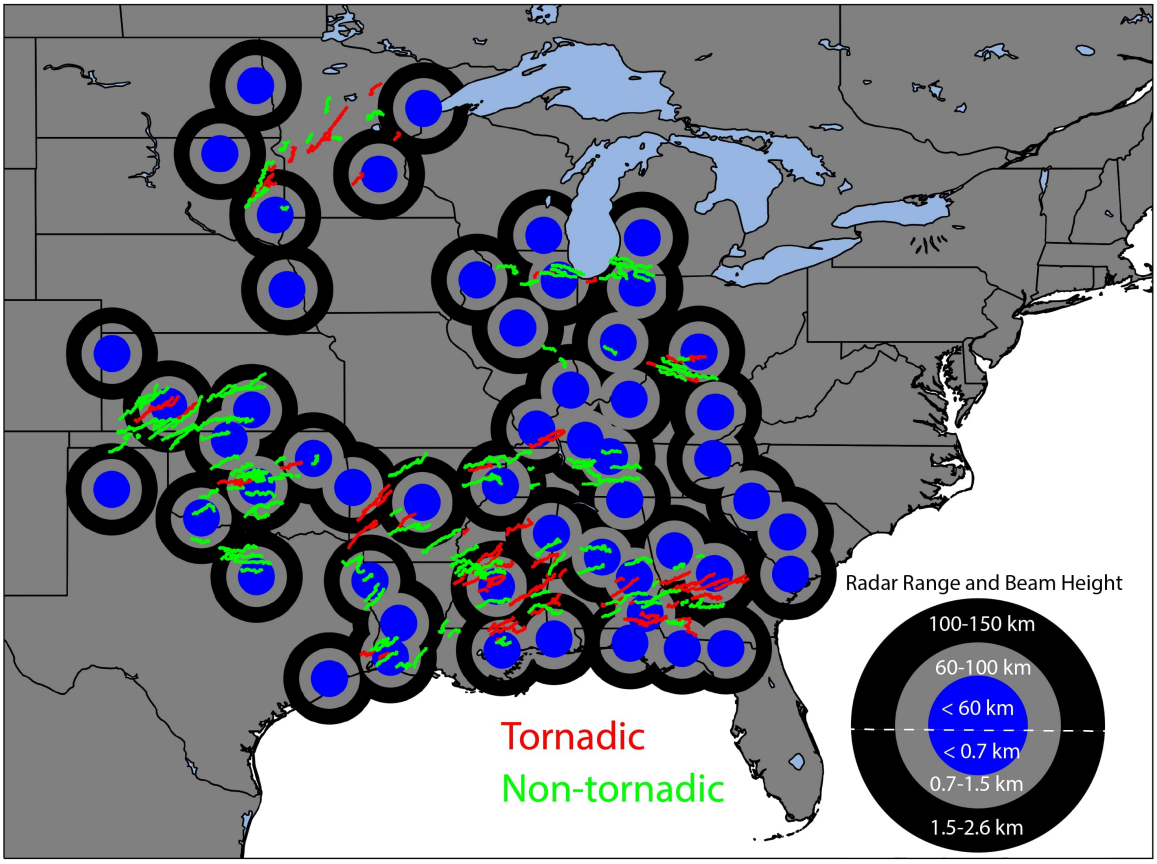

Figure A.6: All tornadic (red) and non-tornadic (green) mesovortex paths tracked from each QLCS storms retained in the dataset. All radars used in the blended products are annotated including their locations (center of the blue circle), corresponding radial distance from each radar in kilometers, and corresponding 0.5° beam height in kilometers AGL.

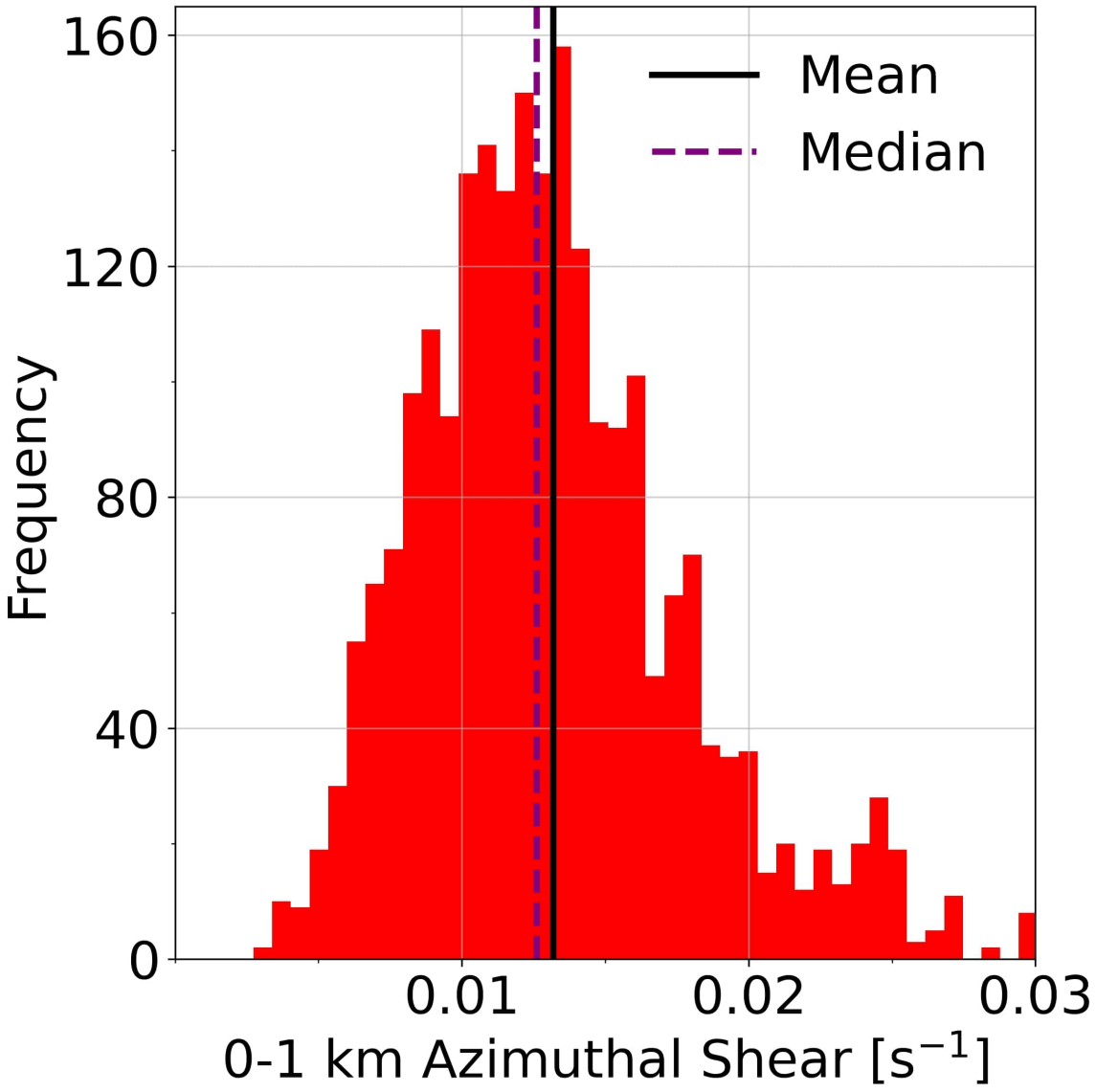

Figure A.7: A histogram showing the 0–1 km layer-maximum azimuthal shear magnitude throughout the lifetime of all tornadic mesovortices retained in the dataset. The mean (solid black) and median (dashed purple) are labeled.

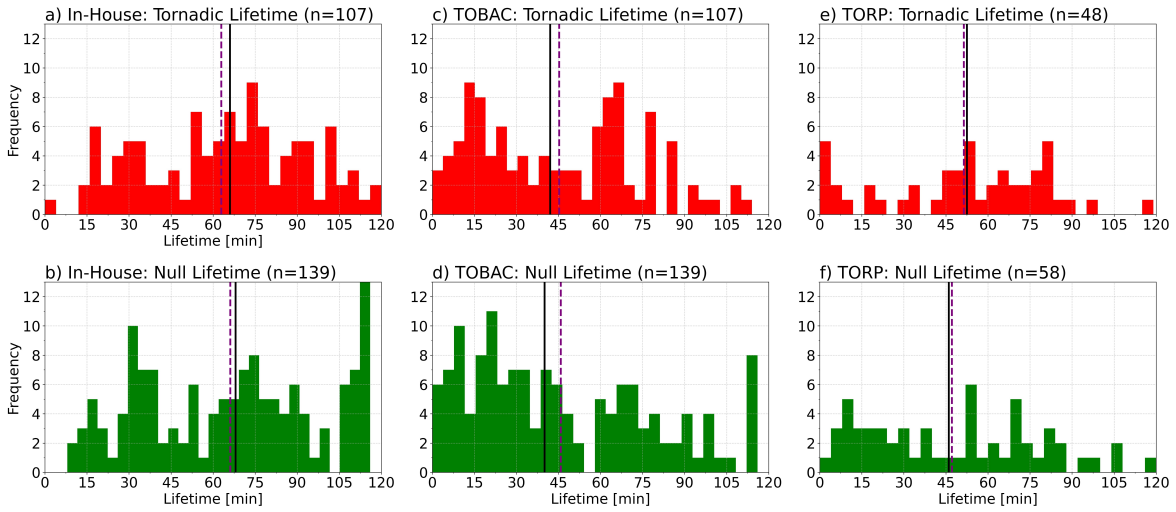

Figure A.8: Histograms of tornadic (red) and null (green) mesovortex lifetime using (a) TRAQS, (b) TOBAC, and (c) TORP. The mean (solid black) and median (dashed purple) are annotated.

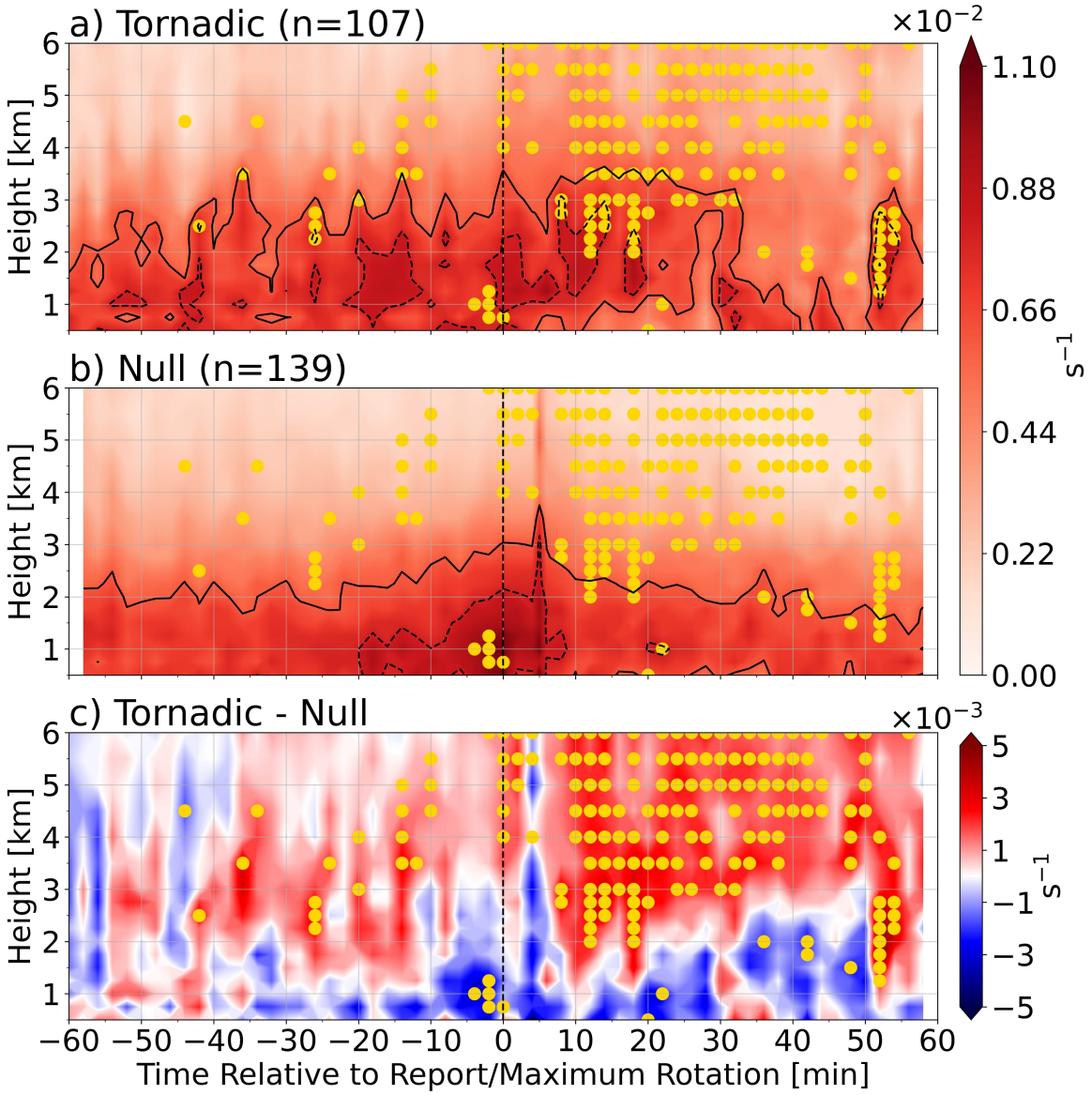

Figure A.9: The median time-height cross section of azimuthal shear following (a) tornadic and (b) null mesovortices plotted against time relative to the (a) tornado report or (b) peak maturity. (c) The difference between the tornadic and null median. Gold stipplings represent significantly different grid points between the tornadic and null median at 95% confidence (α=0.05). Values are contoured at 0.008 s^{-1} (dashed black) and 0.006 s^{-1} (solid black).

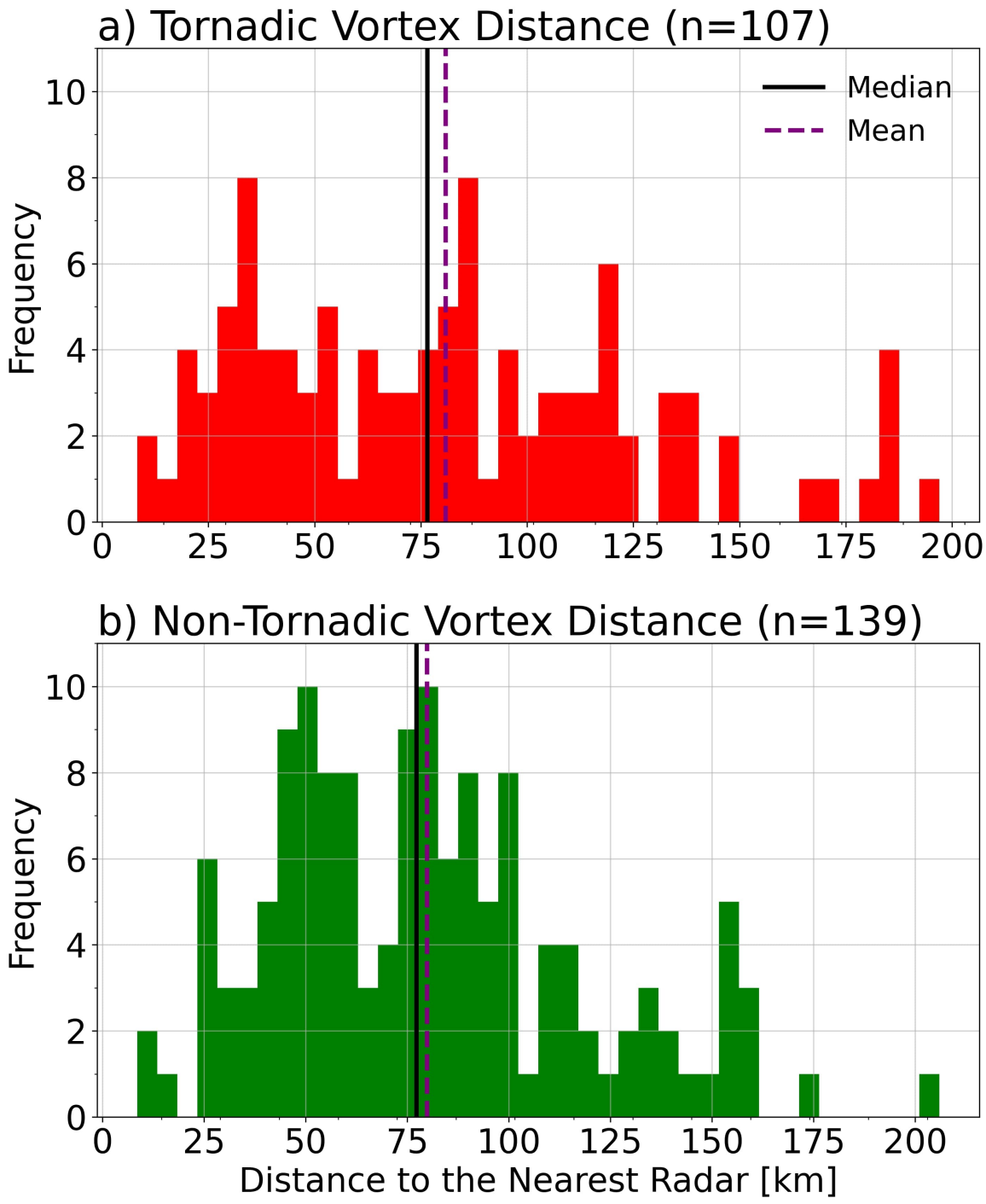

Figure A.10: The distribution of range [km] from the nearest radar at the time of tornadogenesis for (a) all tornadic mesovortices and (b) all null mesovortices binned every 5 km. The mean (solid black) and median (dashed purple) are annotated on each panel and the sample sizes are annotated in each panel title.

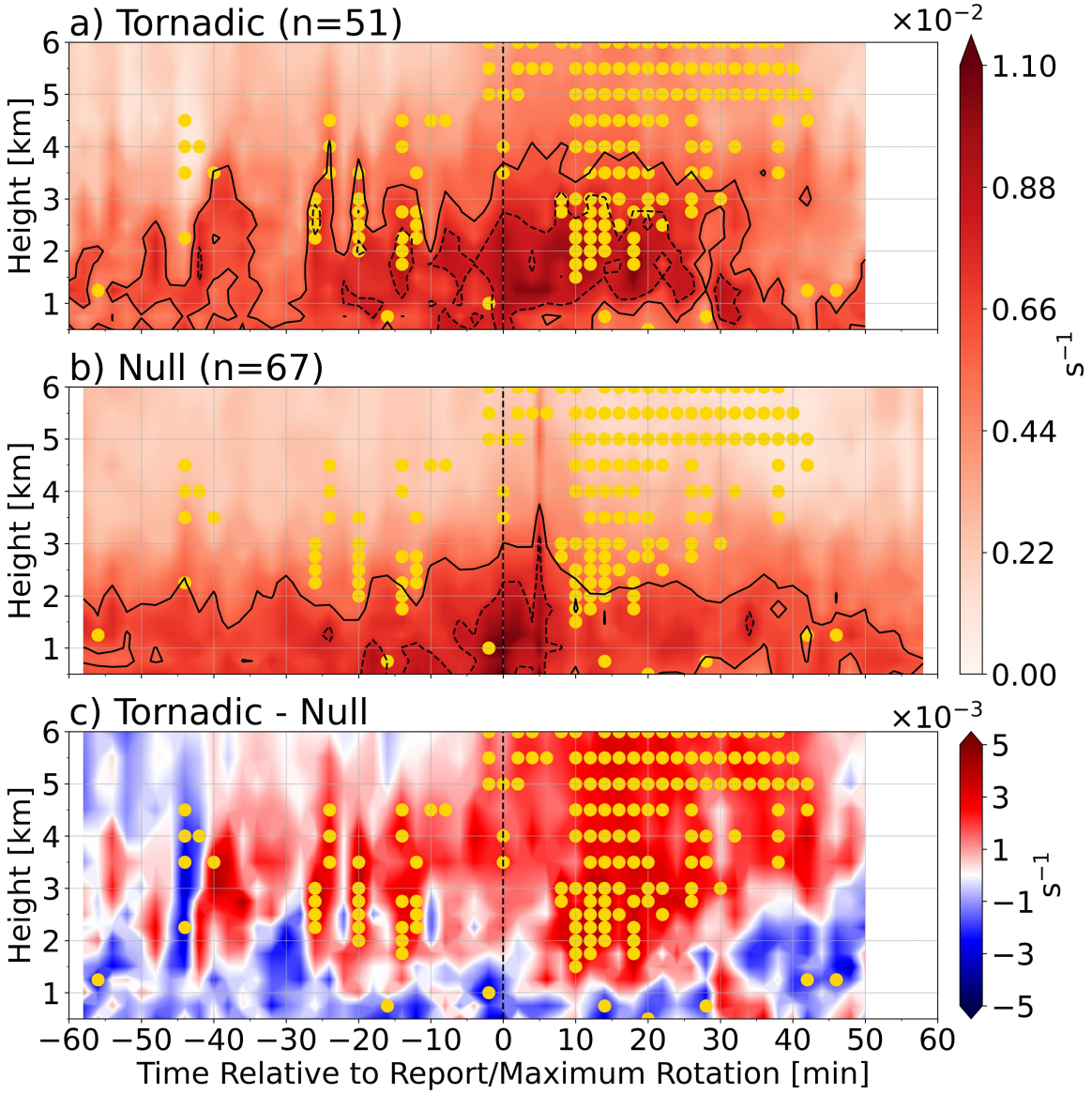

Figure A.11: Same as Fig. A.9, except for close-proximity mesovortices residing less than or equal to 75 km in range from the nearest radar at the time of tornadogenesis or peak-maturity.

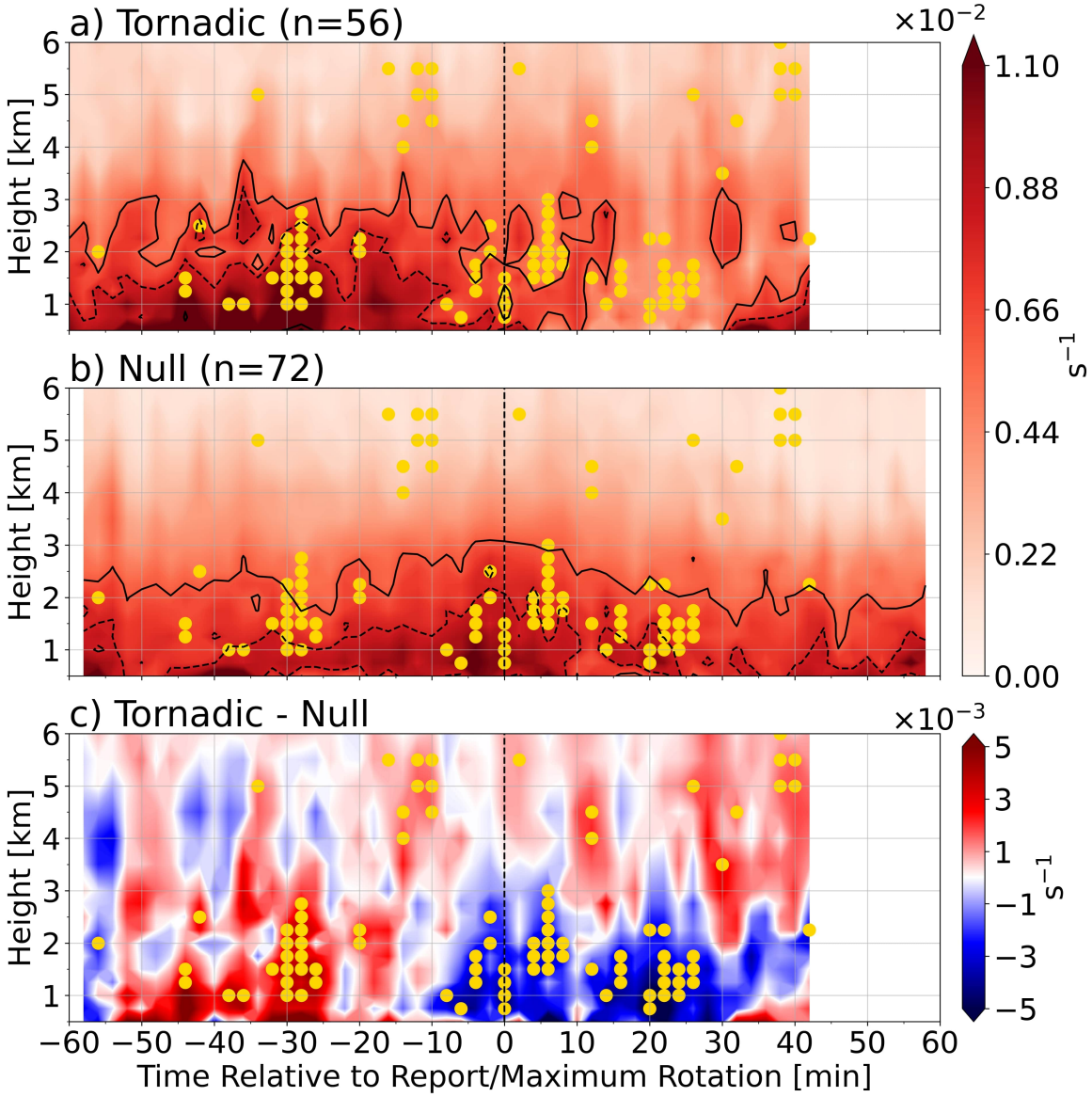

Figure A.12: Same as Fig. A.9, except for far-proximity mesovortices residing greater than 75 km in range from the nearest radar at the time of tornadogenesis or peak-maturity.

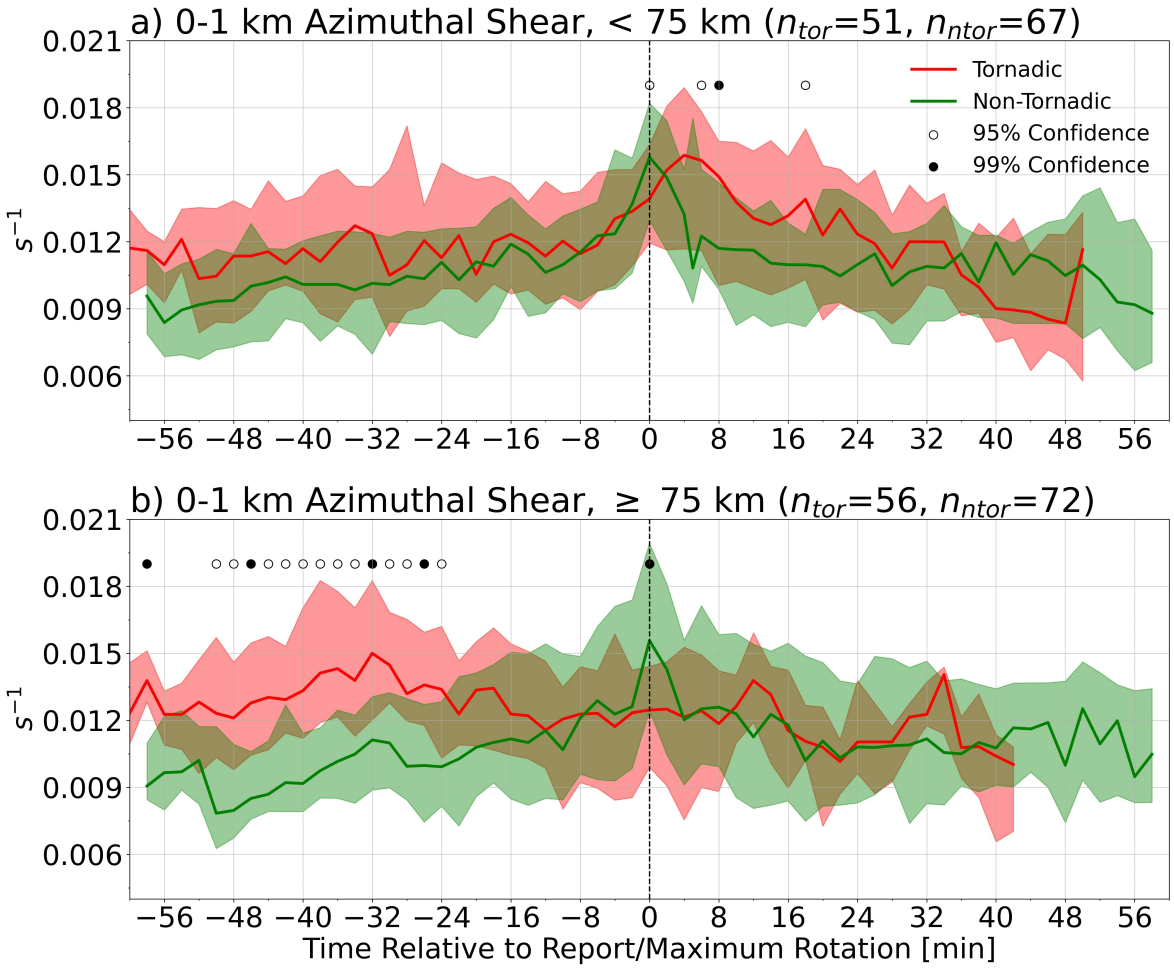

Figure A.13: Median 0–1 km azimuthal shear for tornadic (solid red) and null (solid green) mesovortices with their corresponding interquartile range (25th and 75th percentile; shaded) on the time scale relative to tornadogenesis or peak maturity. Statistically significant differences between the tornadic and null median at 95% (open circle; α=0.05) and 99% (closed circle; α=0.01) confidence are annotated along with the sample size for tornadic (n_{tor}) and null (n_{ntor}) mesovortices in (a) close-proximity and (b) far-proximity which is annotated in the title of each panel.

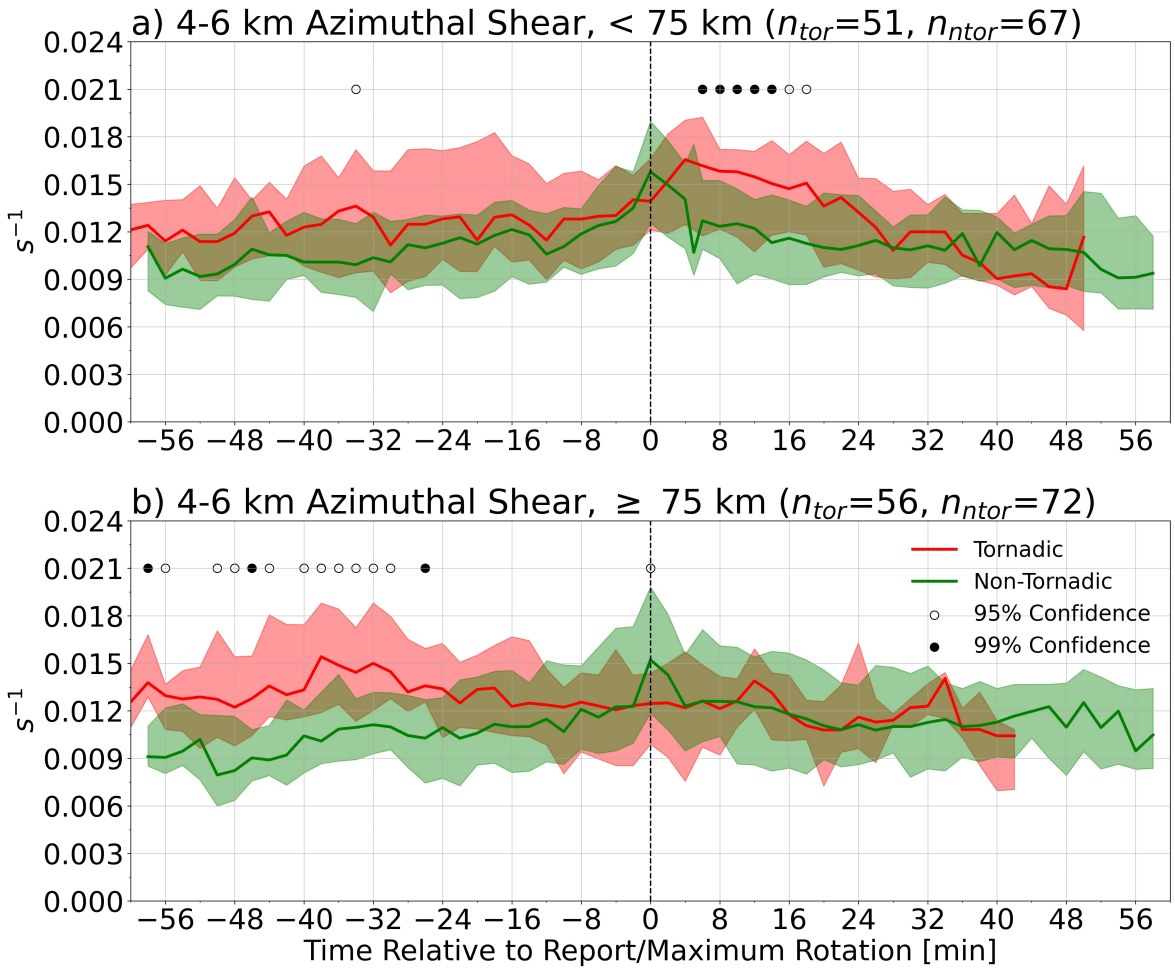

Figure A.14: Same as figure A.13, except showing the 4–6 km layer maximum in azimuthal shear.

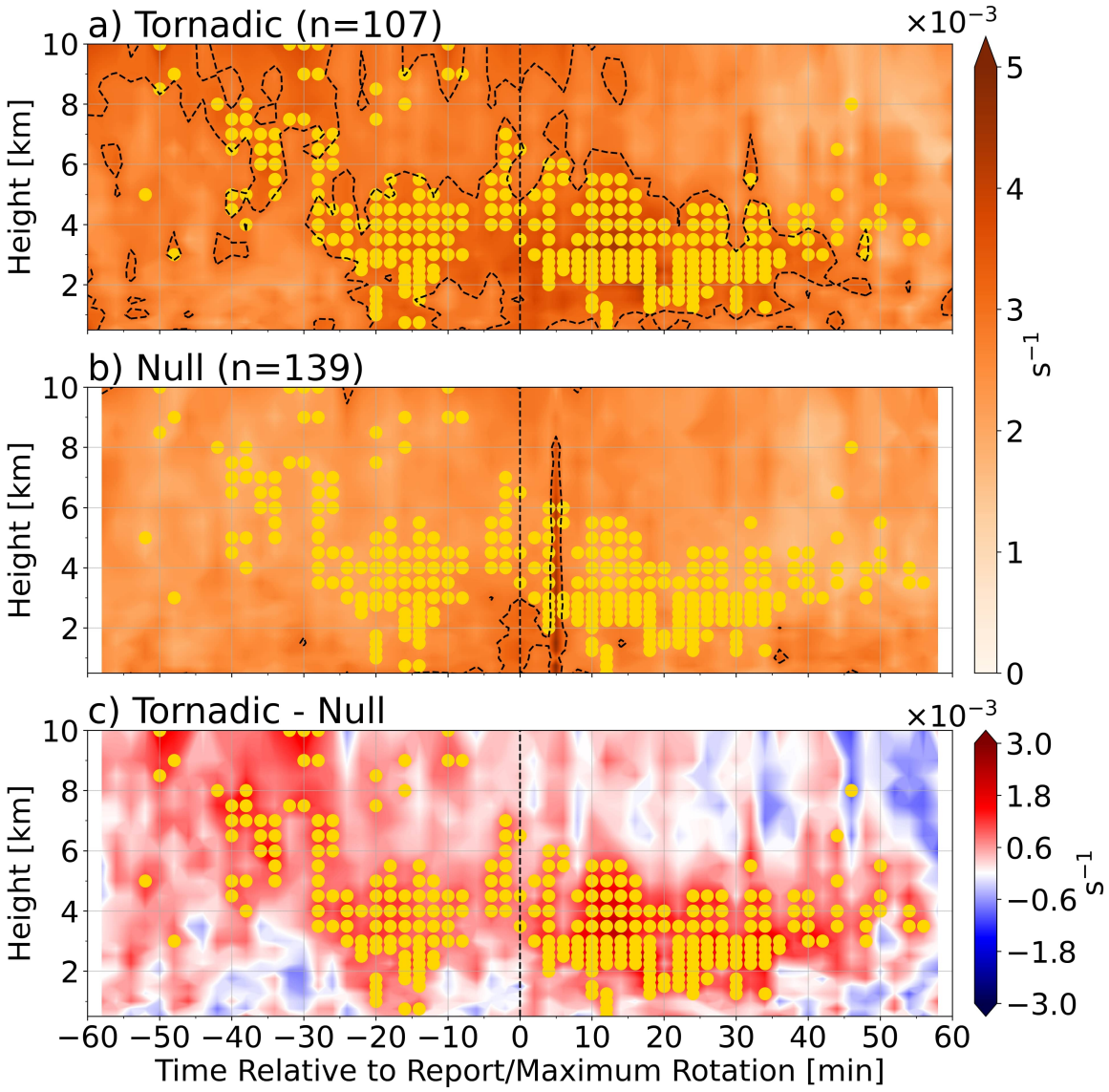

Figure A.15: Similar to Figure A.9, except showing the median DivShear maxima within the boxed region surrounding the location of all (a) tornadic and (b) null mesovortices retained in the dataset. Values are contoured at 0.003 s^{-1} (dashed black).

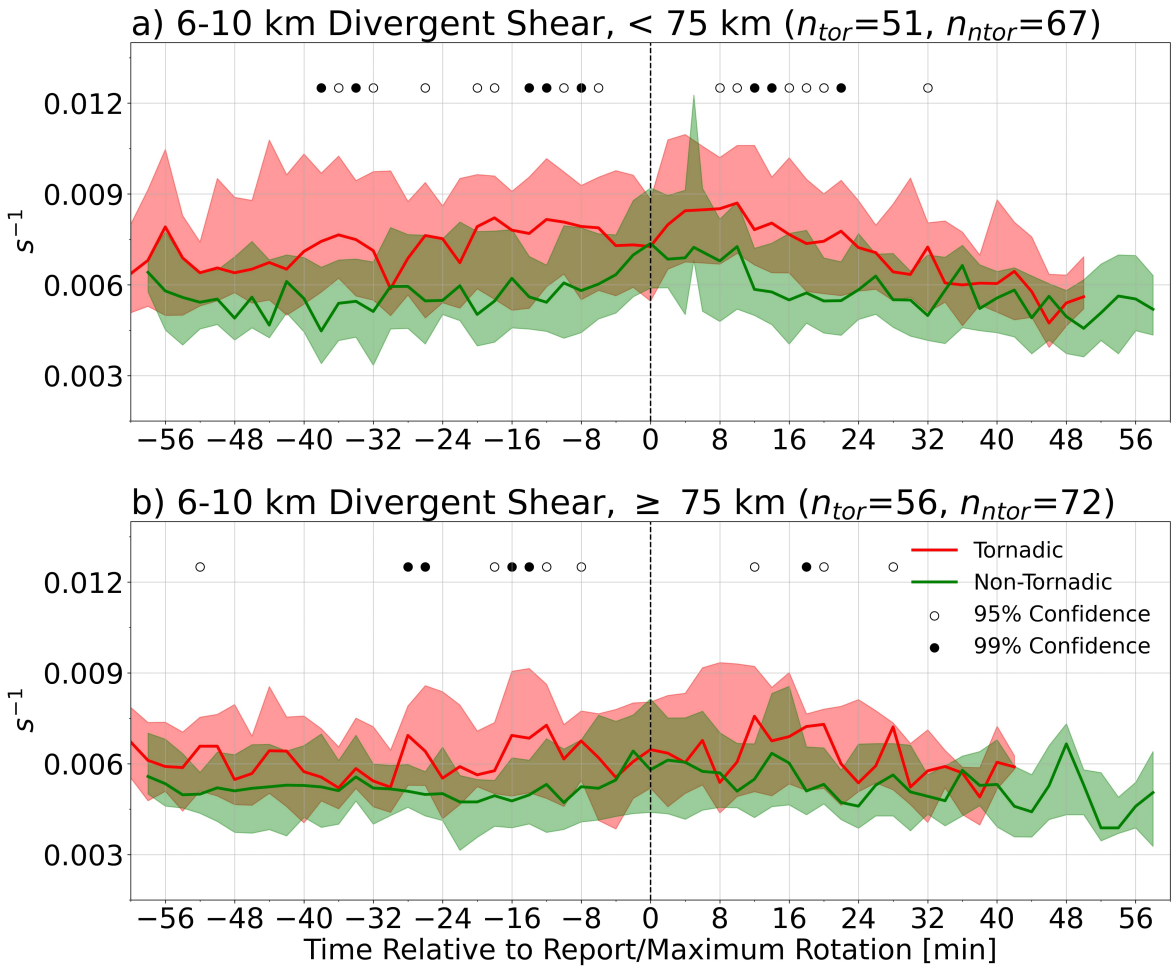

Figure A.16: Similar to Figure A.14, except showing the 6–10 km AGL layer-maximum DivShear.

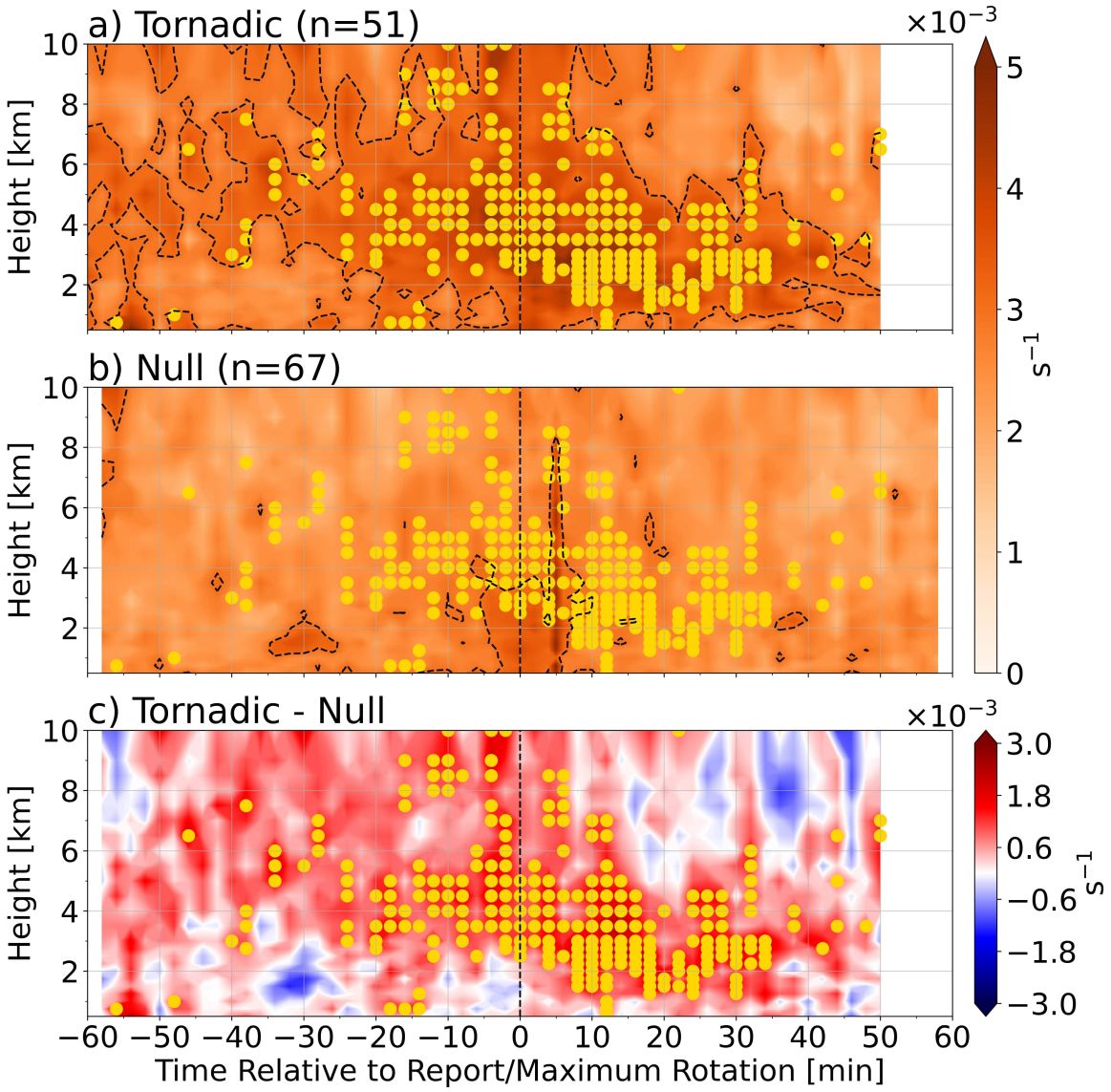

Figure A.17: Similar to Figure A.15, except showing the median DivShear maximum for close-proximity (a) tornadic and (b) null mesovortices.

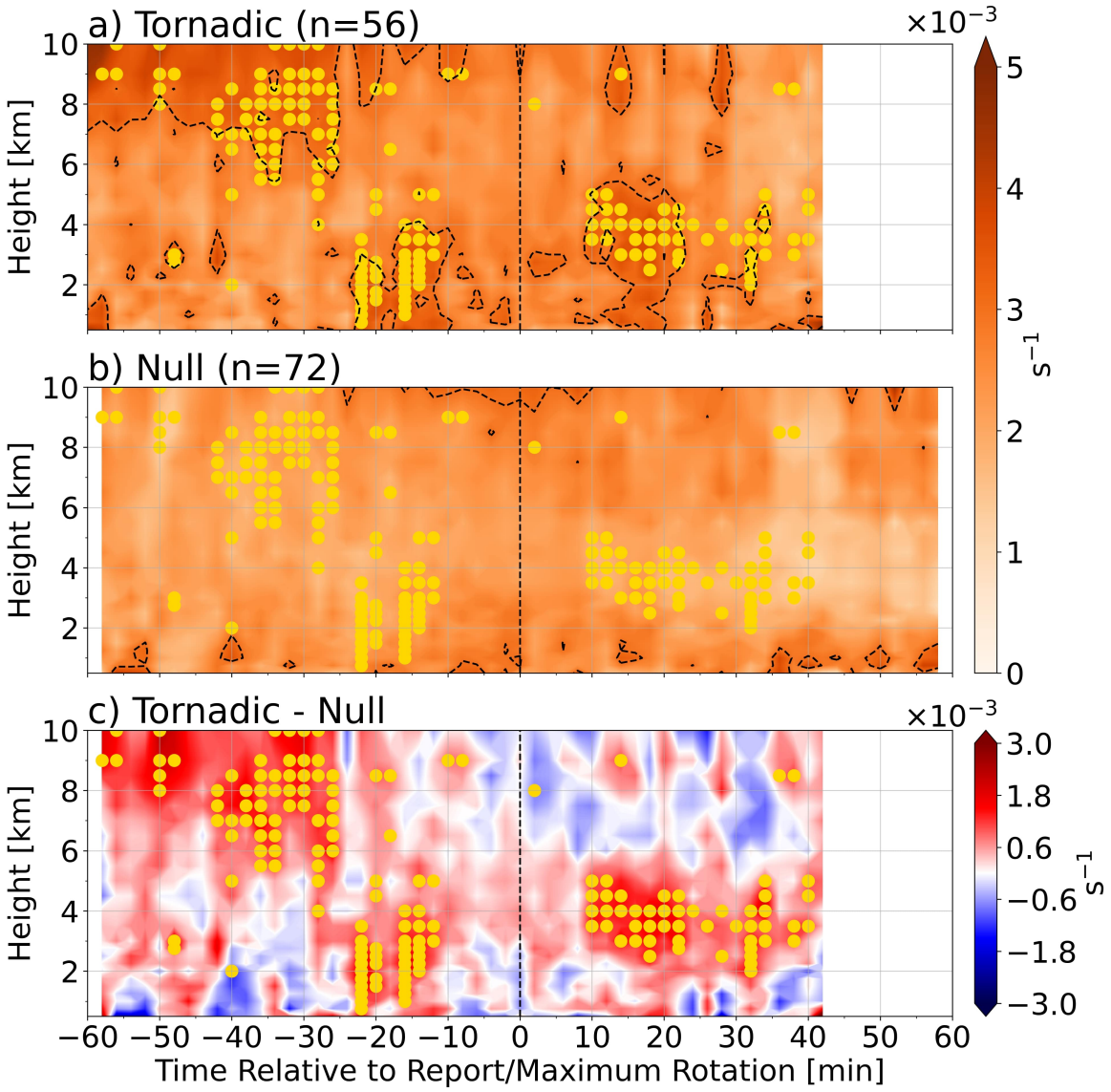

Figure A.18: Similar to Figure A.15, except showing the median DivShear maximum for far-proximity (a) tornadic and (b) null mesovortices.

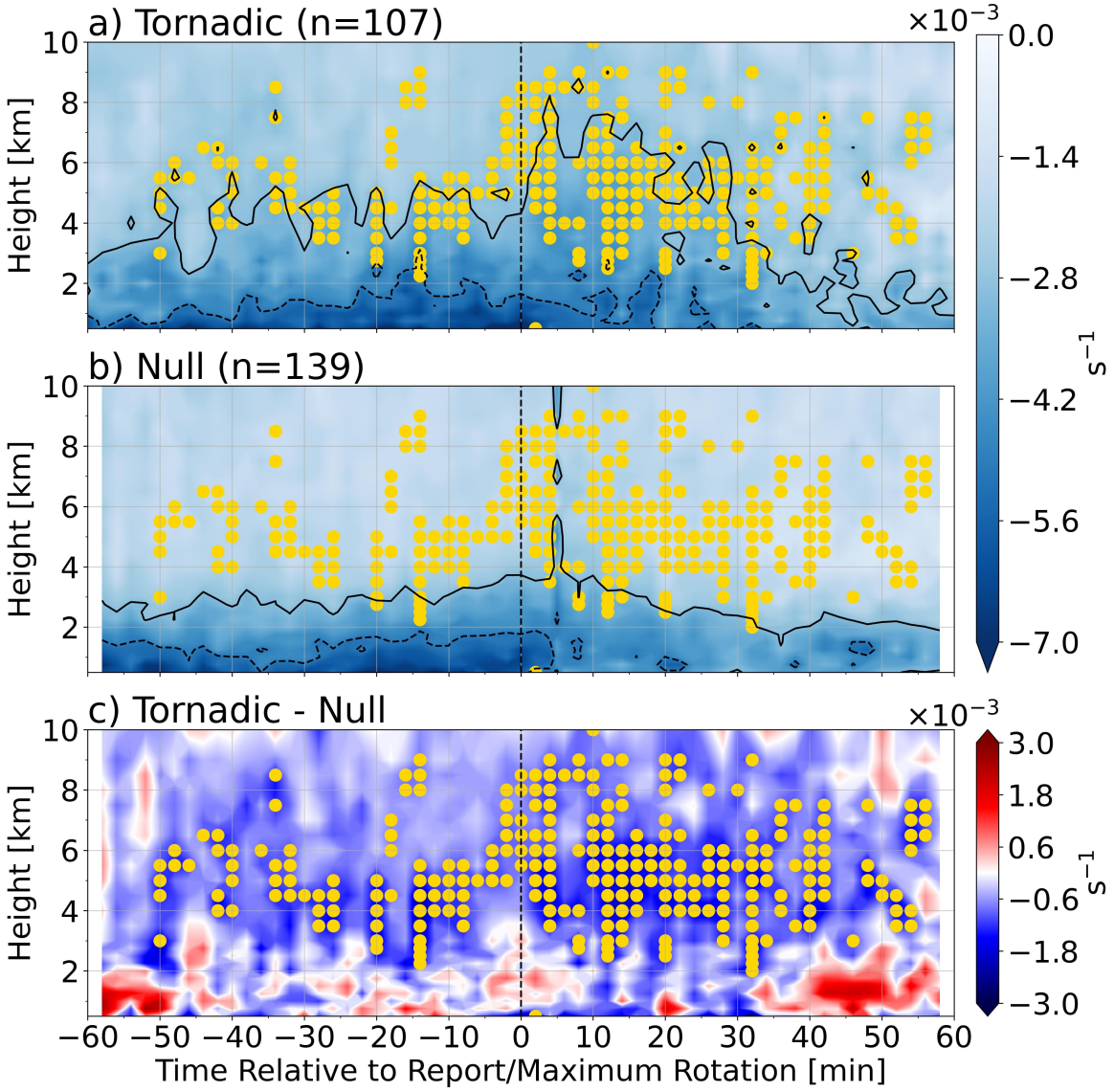

Figure A.19: Similar to Figure A.9, except showing DivShear minimum illustrating the maximum convergence in the boxed region surrounding all (a) tornadic and (b) null mesovortices retained in the dataset. Values are contoured at -0.005 s^{-1} (dashed black) and -0.003 s^{-1} (solid black).

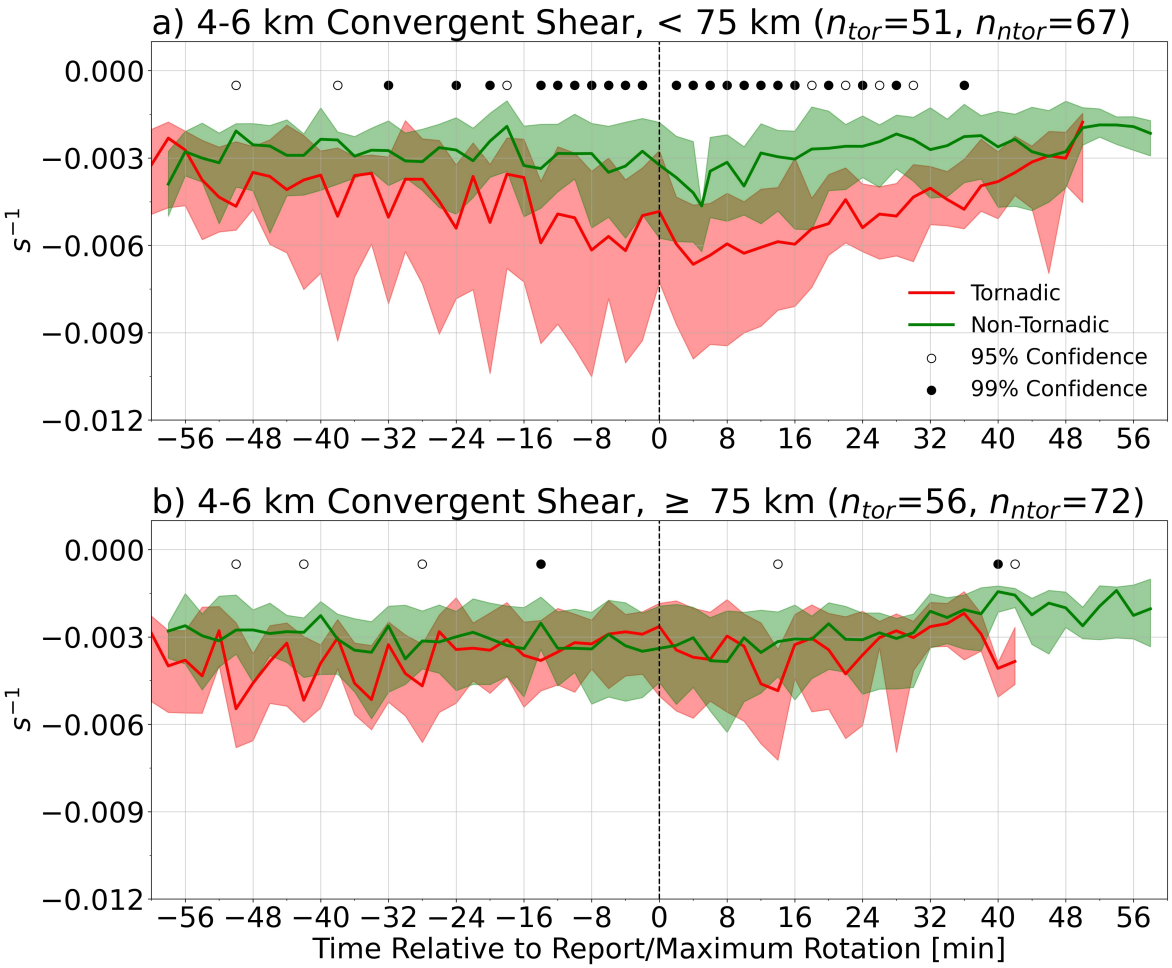

Figure A.20: Similar to Figure A.13, except the 4–6km AGL layer-minimum DivShear, illustrating maximum convergence.

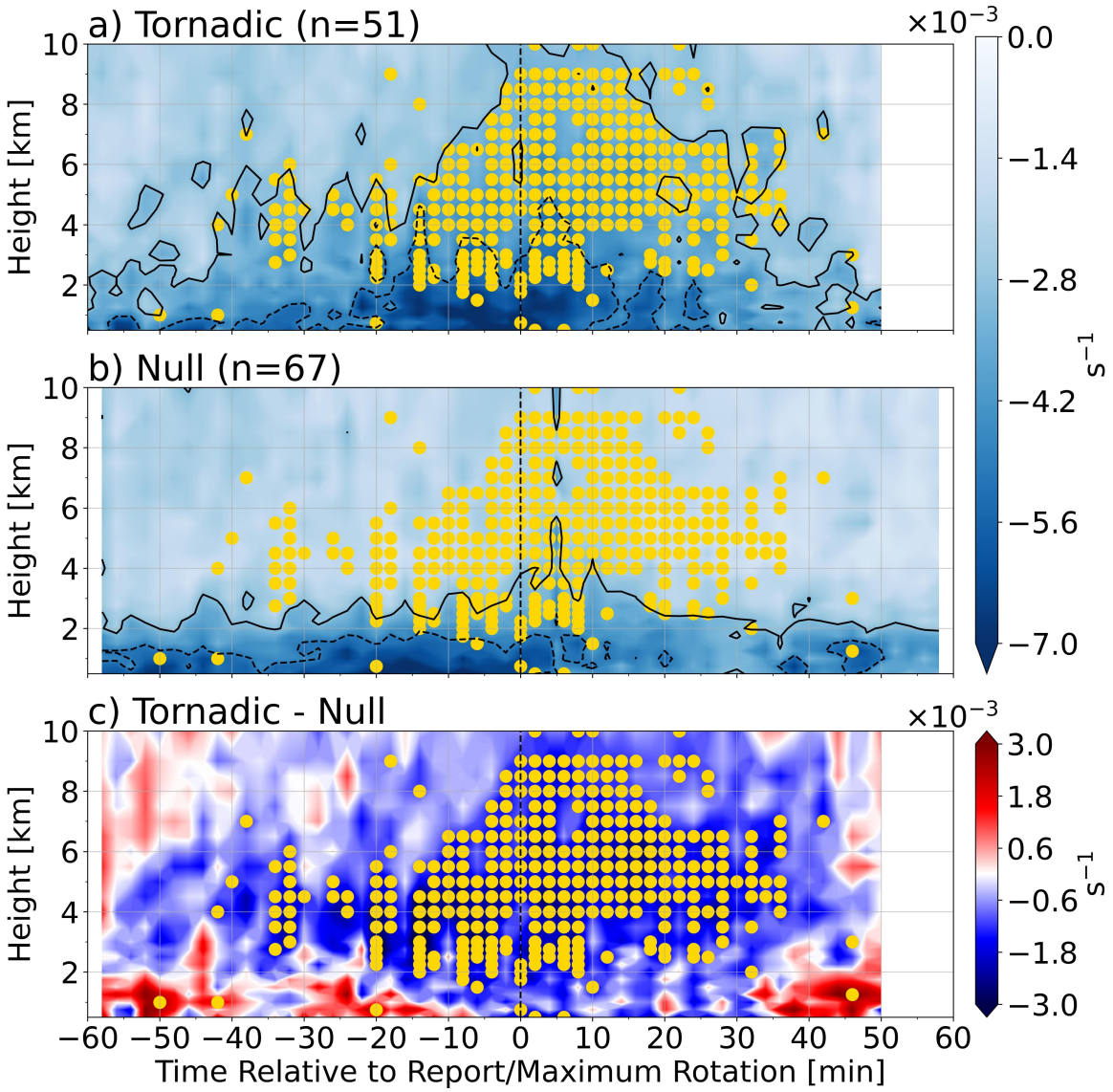

Figure A.21: Similar to Figure A.19, except showing DivShear minimum for close-proximity (a) tornadic and (b) null mesovortices with (c) the difference between the tornadic and null median.

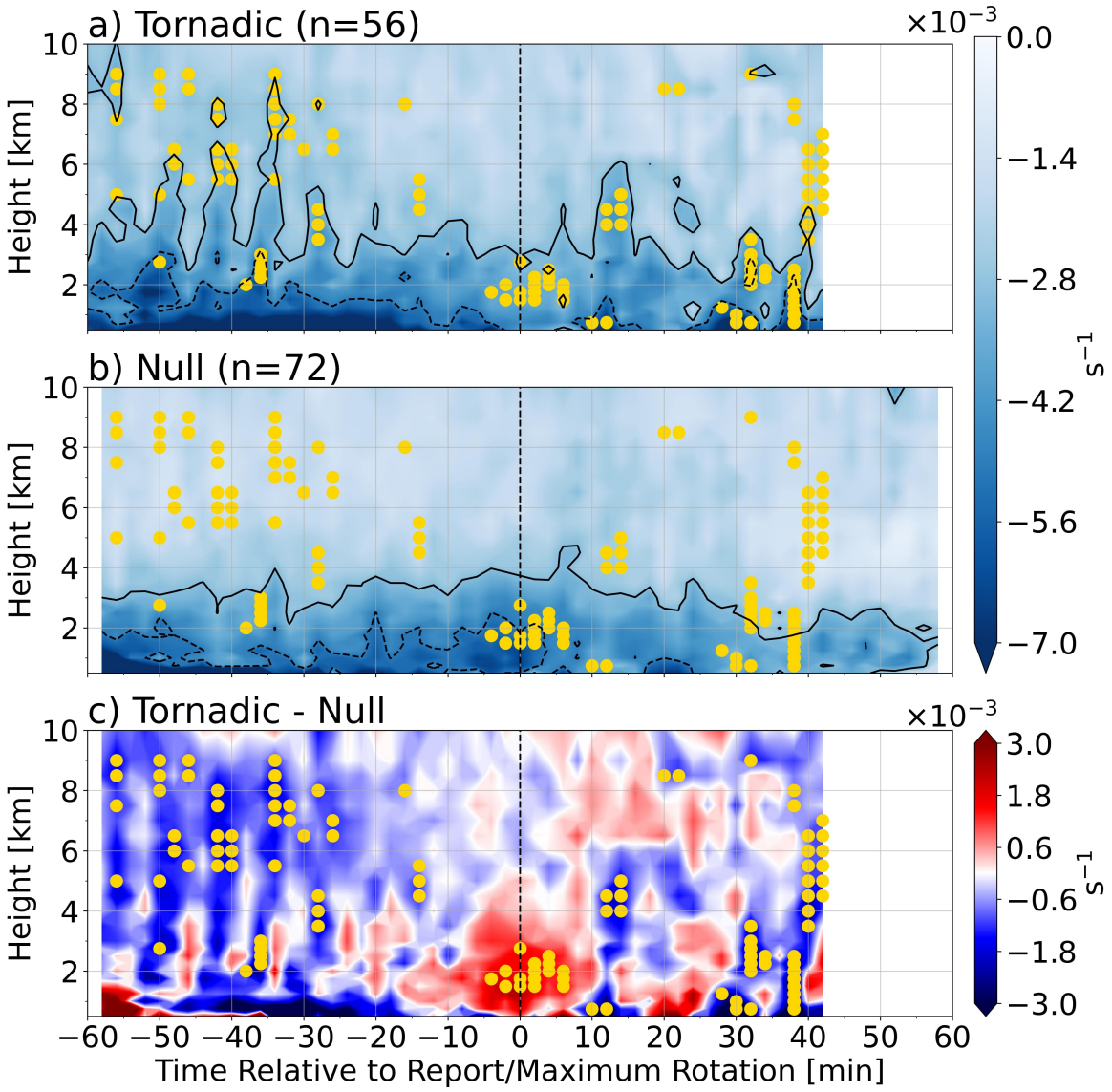

Figure A.22: Similar to Figure A.19, except showing DivShear minima for far-proximity (a) tornadic and (b) null mesovortices with (c) the difference between the tornadic and null median.

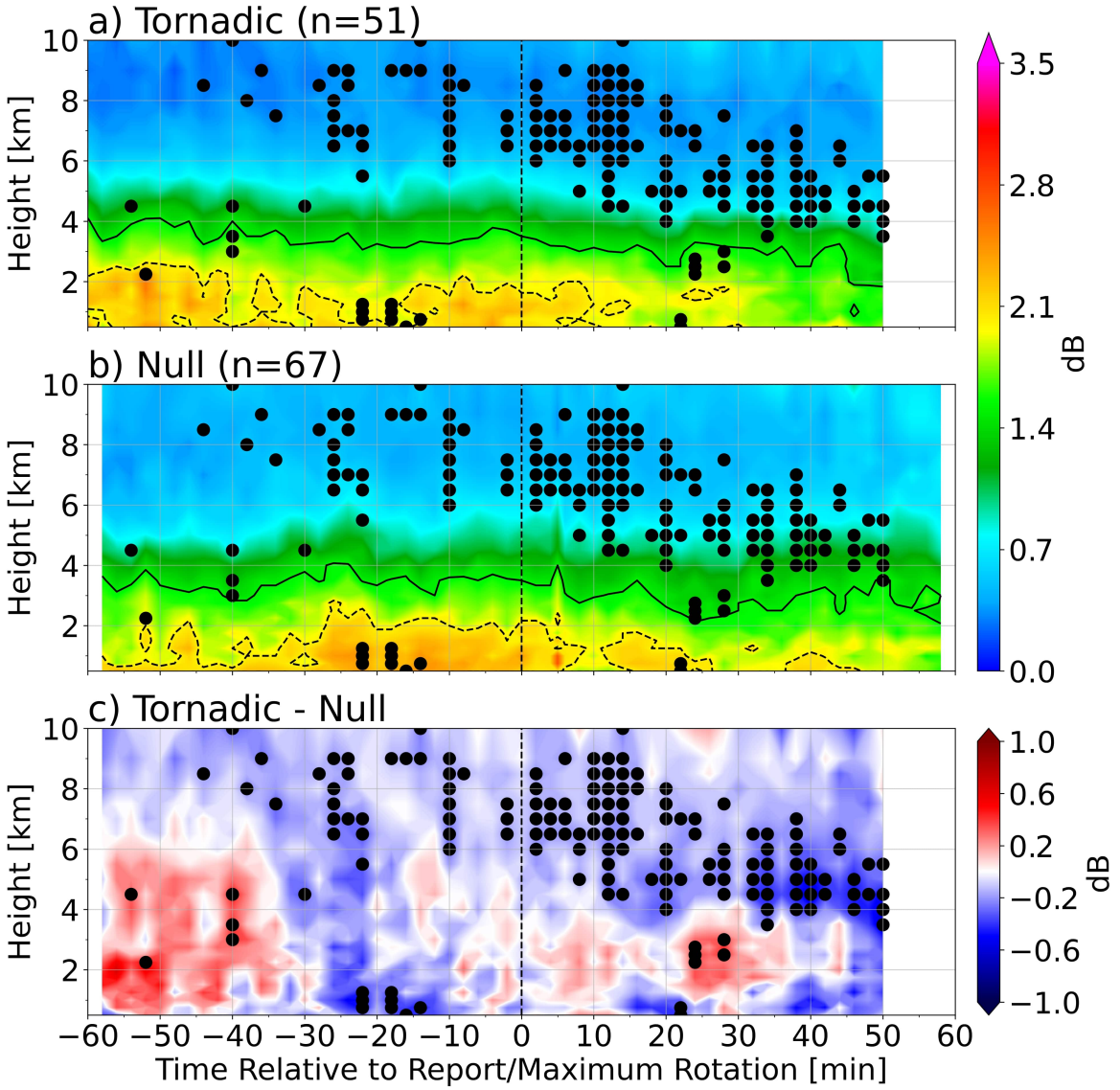

Figure A.23: Similar to Figure A.9, except showing differential reflectivity (Z_{DR}) maximum for close-proximity (a) tornadic and (b) null mesovortices. Significantly different grid points at 95% (α=0.05) confidence are annotated as black circles. Values are contoured at 2 dB (dashed black) and 1.5 dB (solid black).

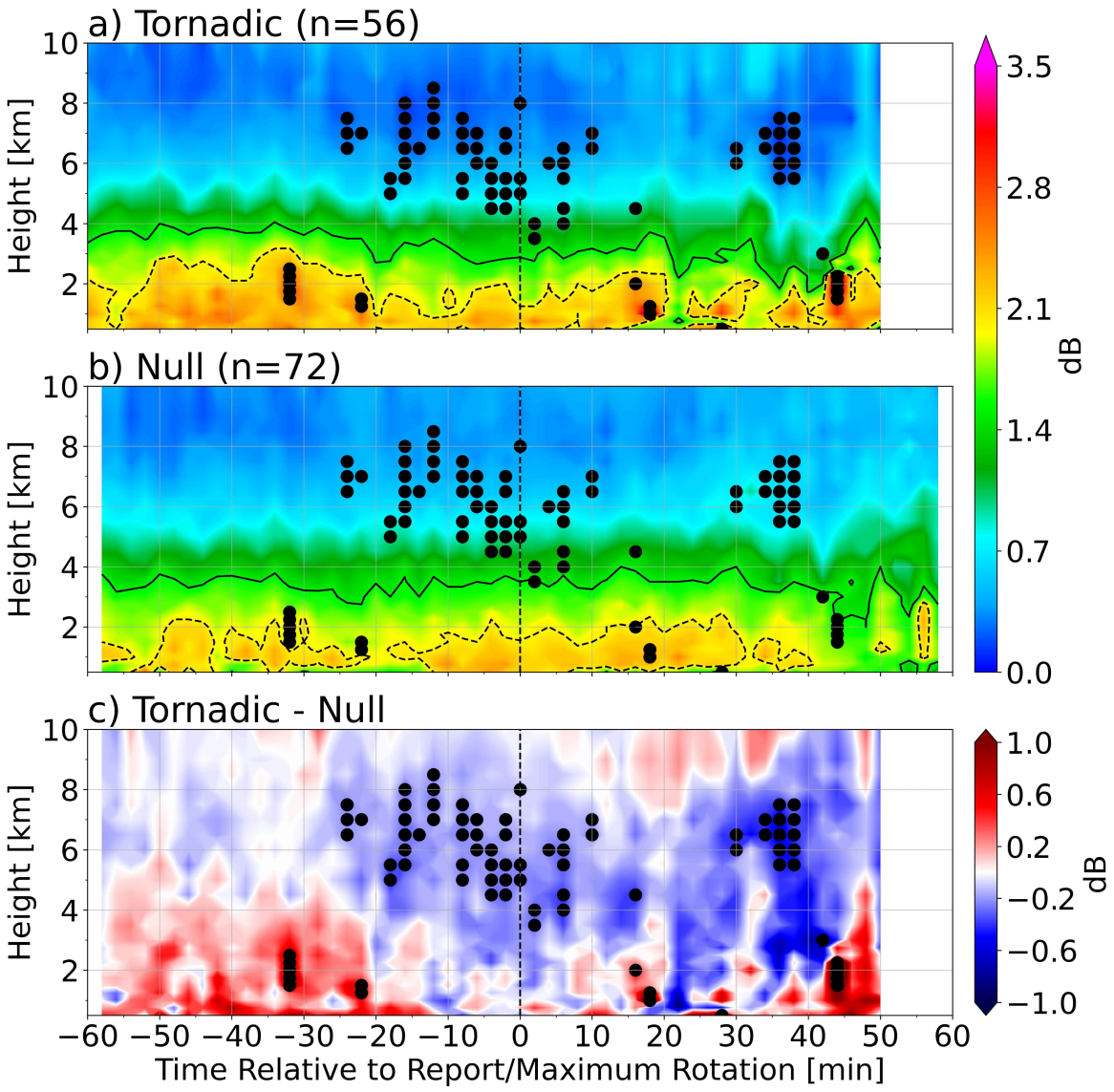

Figure A.24: Similar to Figure A.23, except showing differential reflectivity (Z_{DR}) maximum for far-proximity mesovortices.

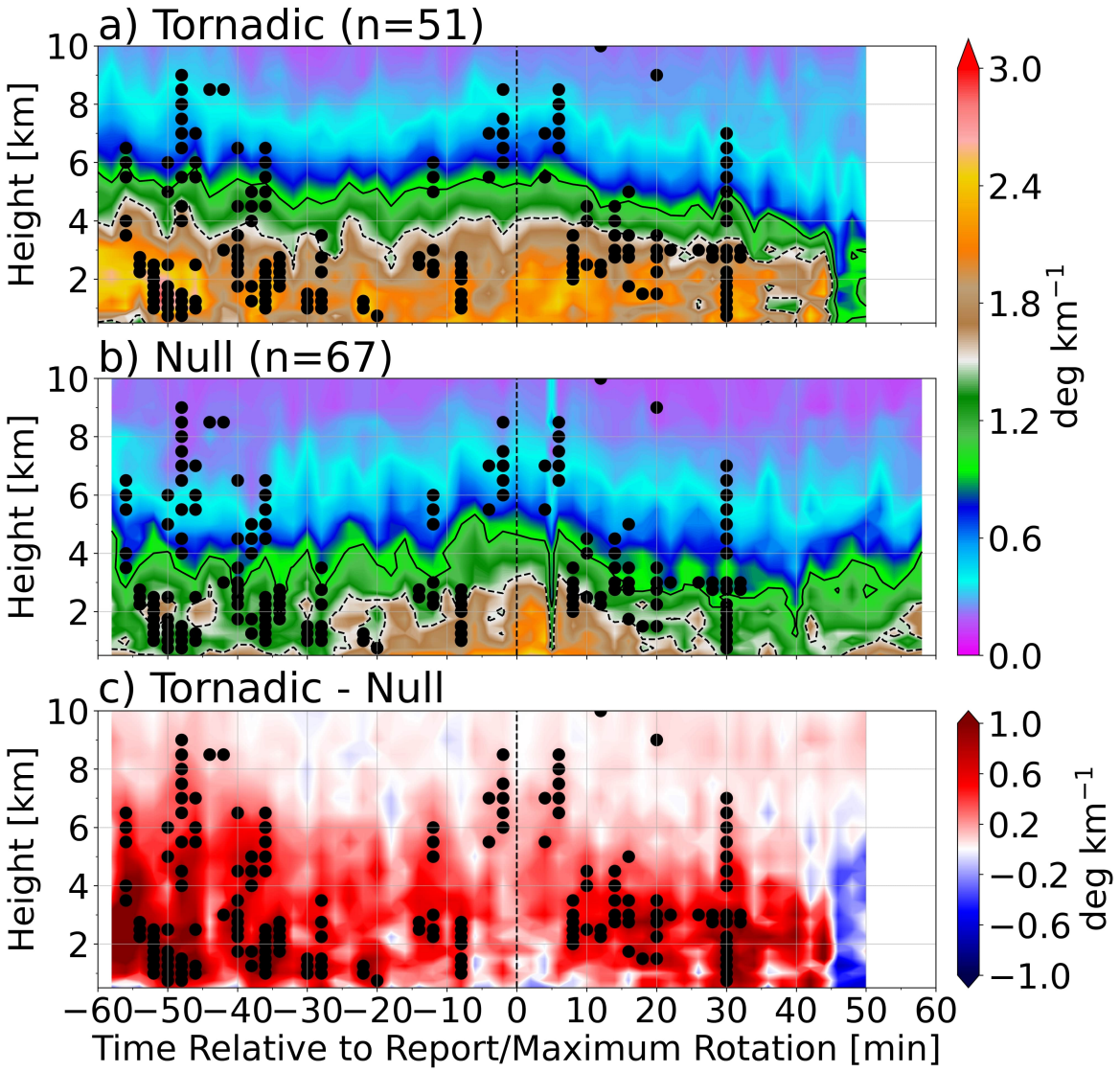

Figure A.25: Similar to Figure A.9, except showing the specific differential phase (KDP) maximum for close-proximity (a) tornadic and (b) null mesovortices. Significant grid points at 95% are shown as black circles. Values are contoured at 1.5 deg km^{-1} (dashed black) and 1 deg km^{-1} (solid black).

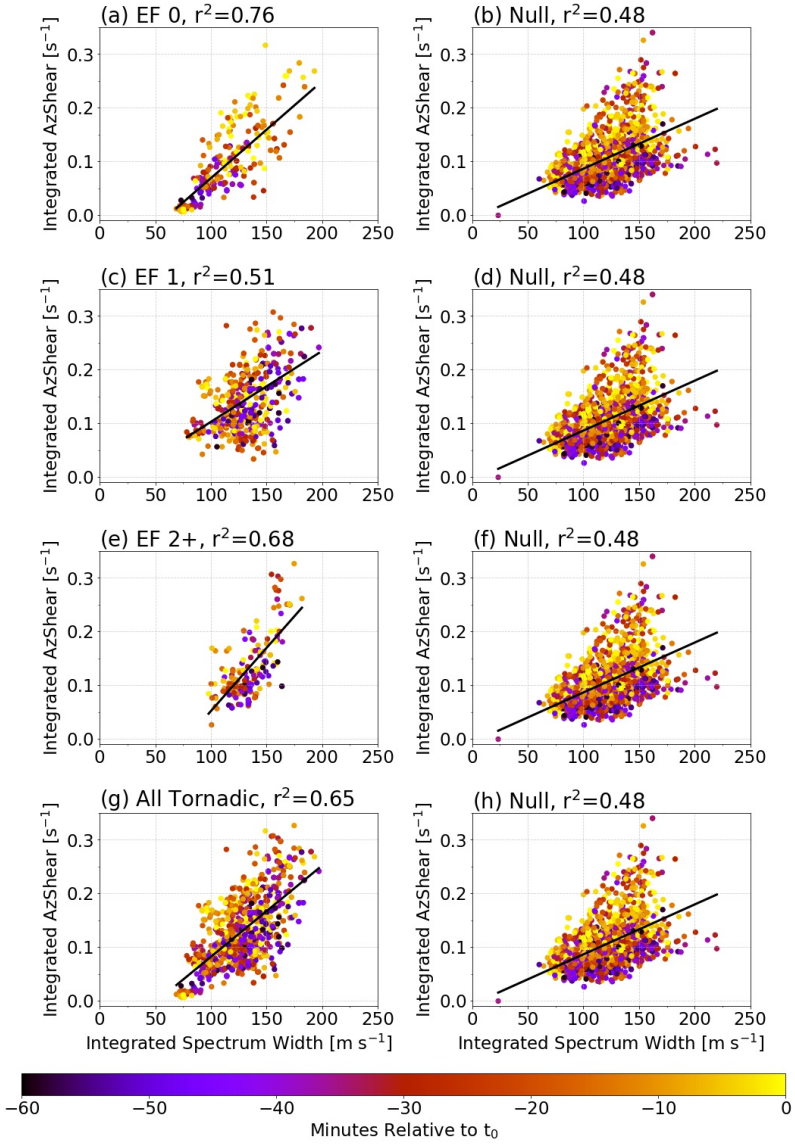

Figure A.26: The correlation between column-integrated azimuthal shear maximum and column-integrated spectrum width maximum following each QLCS vortex in time prior to t_0 (shaded). Each product is integrated from 0.25–10 km AGL beginning 60 minutes prior to t_0 and ending at t_0 (shaded). Each panel on the left-most column represents all tornadic mesovortices that spawned (a) EF 0, (c), EF 1, (e) EF 2+ tornadoes. (g) All tornadic mesovortices regardless of spawned tornado strength on the EF scale. The panels on the right most column represent all null mesovortices for comparison.

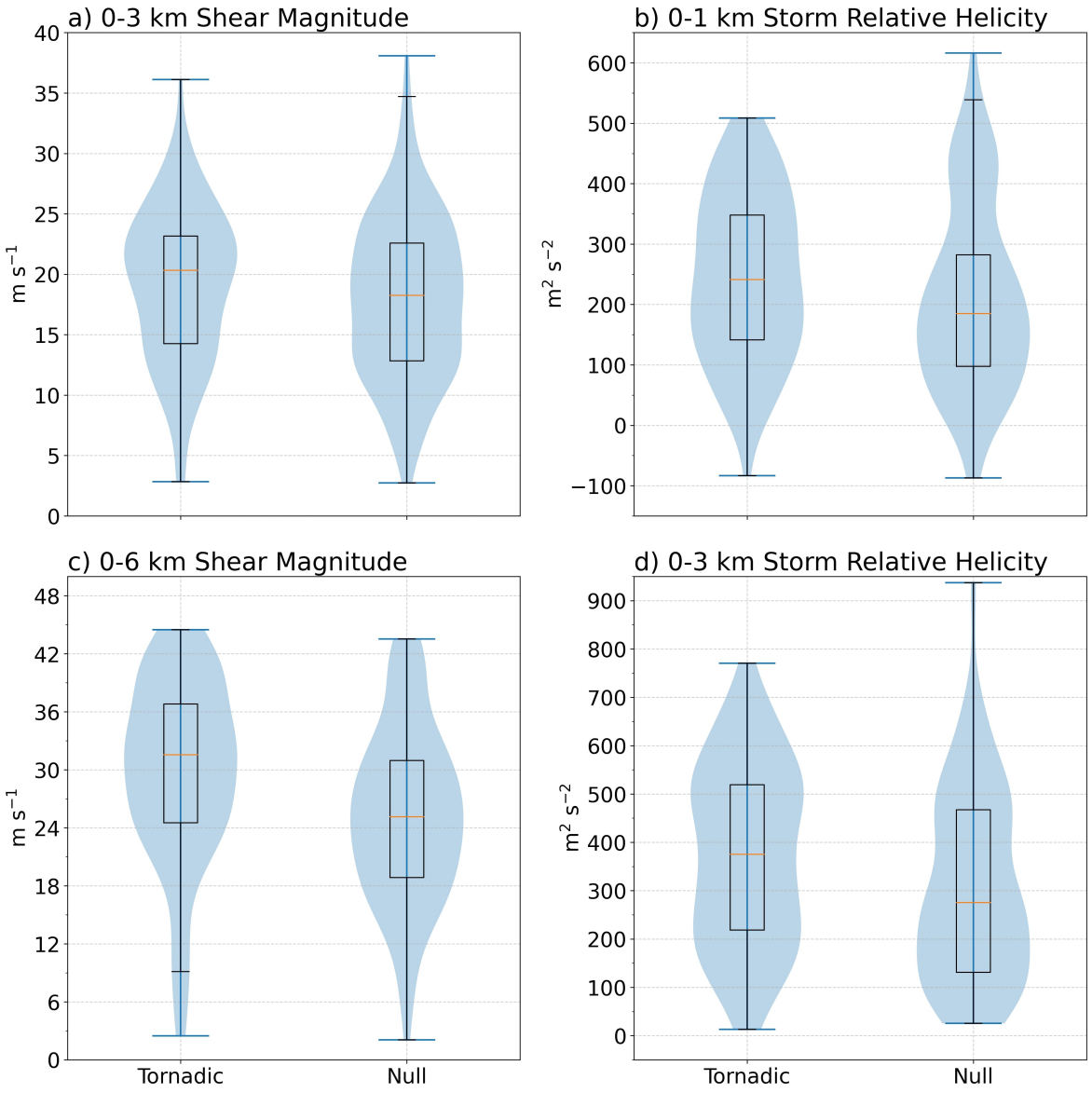

Figure A.27: The distribution of kinematic environmental parameters derived from the RAP reanalysis showing (a) the 0–3 km vertical wind shear magnitude, (b) the 0–1 km storm relative helicity, (c) the 0–6 km bulk wind shear magnitude, and (d) the 0–3 km storm relative helicity. The distribution of tornadic (left) and null (right) mesovortices are shown on each panel captured one hour prior to t_0.

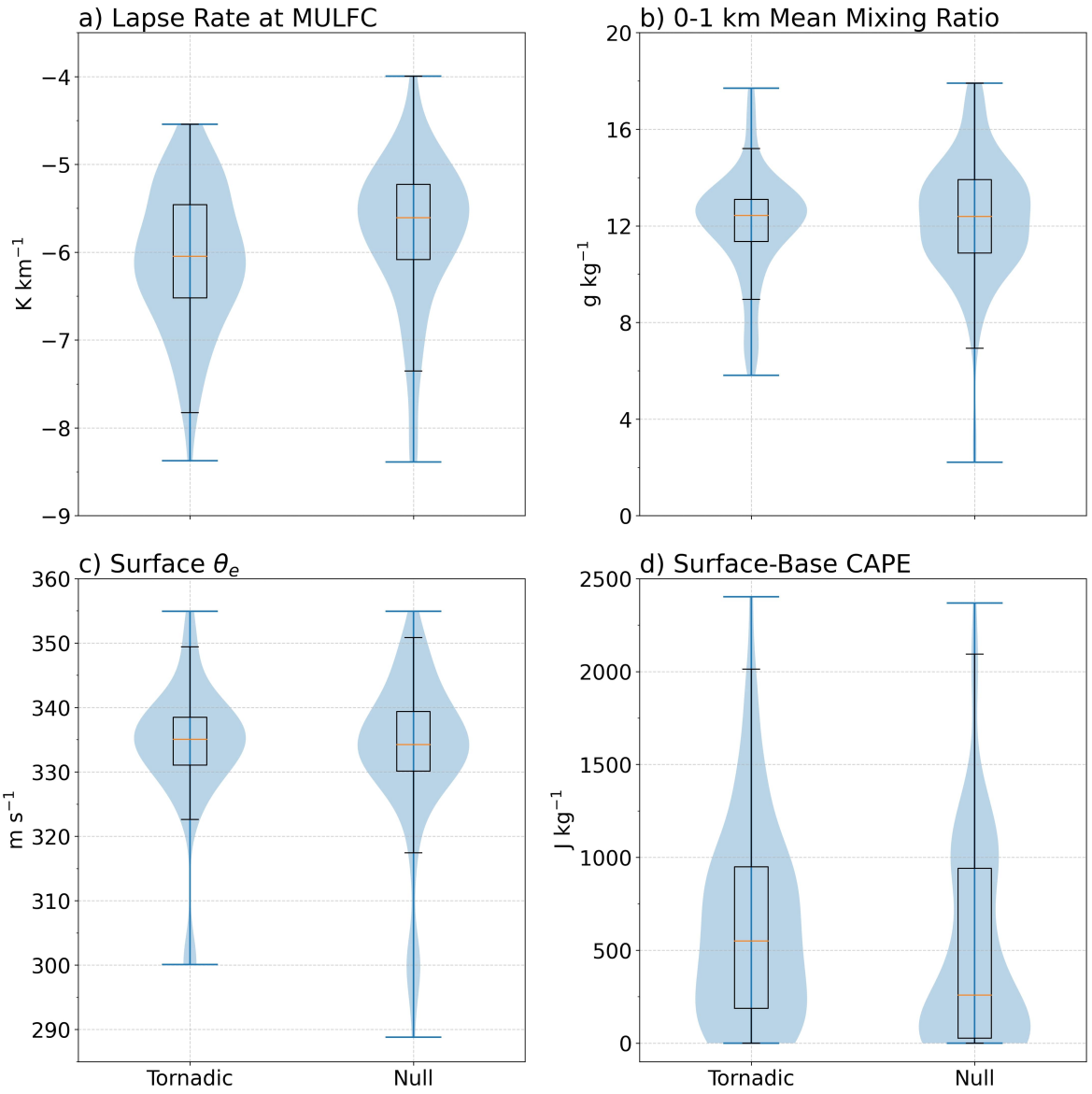

Figure A.28: Similar to Fig. A.27, except showing (a) the lapse rate at the most unstable lifted condensation level (MULFC), (b) the 0–1 km layer mean mixing ratio, (c) the surface equivalent potential temperature (θ_e), and (d) the surface-based CAPE.

2 Tables

Table A.1: The full dataset containing 13 total QLCS storms including the start date of observation, their region of occurrence, the total number of WSR-88Ds used in blending, the number of tornadic mesovortices sampled (T_{vort}), the total number of non-tornadic QLCS mesovortices sampled (N_{vort}), the start time of observation, and the end time of observation in UTC. The total number of tornadic and non-tornadic mesovortices is shown at the bottom of the table in bold. Regions are organized by North Central Plains (NCP), Central Plains (CP), South Central Plains (SCP), Southeast (SE), Tennessee Valley (TV), and Midwest (MW).

Date	Region	Radars Used	T_{vort}	N_{vort}	Start Time	End Time
26 May 2019	SCP	5	7	8	02:00	07:00
9 April 2020	MW	5	11	8	23:00	05:00
24 April 2021	SE	4	5	7	10:00	15:00
21 June 2021	MW	6	2	11	02:00	07:00
13 October 2021	CP	7	10	23	00:00	11:00
27 October 2021	SE	6	4	14	16:00	00:00
30 March 2022	TV	9	23	7	18:00	06:00
5 April 2022	SE	14	19	10	13:00	00:00
13 April 2022	SE	5	7	8	19:00	03:00
30 May 2022	NCP	6	13	8	18:00	02:00
12 October 2022	TV	6	0	10	19:00	01:00
24 October 2022	SCP	6	1	14	09:00	17:00
5 November 2022	SE	12	5	11	00:00	12:00
Totals			**107**	**139**		

Table A.2: The full dataset organized by region of the CONUS including the average lifetime of tornadic mesovortices ($T_{Lifetime}$) and non-tornadic mesovortices ($N_{Lifetime}$) in minutes and average path length for tornadic (T_{path}) and non-tornadic (N_{path}) mesovortices in kilometers.

Region	QLCSs	$T_{Lifetime}$ [min]	$N_{Lifetime}$ [min]	T_{path} [km]	N_{path} [km]
NCP	1	56.15	57.75	65.17	56.48
CP	1	71.13	53.25	96.22	66.08
SCP	3	48.1	71.48	40	56.98
SE	4	68.22	58.80	78.72	62.29
TV	2	64.87	54.94	68.09	54.13
MW	2	44.92	59.98	45.43	59.92